Department of Precision and Microsystems Engineering

Automated reset controller design with a novel structure for improved performance of an industrial motion stage

Yixuan Liu

Report no : 2023.069
Coach : ir. L.F. van Eijk, ir. X. Zhang, dr. ir. D. Kostić
Professor : dr. ir. S.H. HosseinNia
Specialisation : Mechatronic System Design
Type of report : Master Thesis
Date : 30/08/2023

AUTOMATED RESET CONTROLLER DESIGN WITH A NOVEL STRUCTURE FOR IMPROVED PERFORMANCE OF AN INDUSTRIAL MOTION STAGE

by

Yixuan LIU

Master Thesis

in partial fulfillment of the requirements for the degree of

Master of Science

in Mechanical Engineering

at the Delft University of Technology,

to be defended publicly on 30/08/2023

Supervisors:	dr. ir. S.H. HosseinNia	(TU Delft)
	ir. X. Zhang	(TU Delft)
	ir. L.F. van Eijk	(TU Delft)
	dr. ir. D. Kostić	(ASMPT)
Thesis committee:	dr. ir. S.H. HosseinNia	(TU Delft)
	dr. ir. M.A.S. Kolarijani	(TU Delft)
	dr. ir. M. Guo	(TU Delft)
	ir. X. Zhang	(TU Delft)
	ir. L.F. van Eijk	(TU Delft)

TU Delft Delft University of Technology

ASMPT enabling the digital world

Abstract

In the realm of precision motion control, Linear Time-Invariant (LTI) controllers, such as PID controllers, have gained widespread adoption. The popularity of linear controllers stems from their simplicity in design through loop-shaping methods, which establish a connection between open-loop and closed-loop performance. However, the traditional LTI control encounters challenges in meeting evolving demands for high accuracy, including exceptional tracking and disturbance suppression capabilities, while maintaining high speed. These challenges arise due to the inherent limitations of LTI controllers, such as the waterbed effect and Bode's gain-phase relationship. Promising findings in recent literature suggest that reset control, a nonlinear control technique, is possible to overcome these limitations. Furthermore, reset control could also potentially allow the use of straightforward design techniques, thus making it suitable for industrial applications. In this study, we explore the application of the Proportional Clegg Integrator (PCI), a reset element, to replace the Proportional Integrator (PI) within the PID framework for a wire bonder, aiming to break LTI limitations and therefore improve the system's performance. However, due to the reset action of the PCI, it cannot provide a constant buffer force as the PI does to compensate for the machine's nonlinearity and external disturbances. This lack of compensation can lead to undesired limit-cycling behavior, preventing the system from achieving zero steady-state error. To address this issue, a PI is added after the PCI to form a PCI-PID framework for completely eliminating the limit cycles. To optimize the performance of the PCI within the PCI-PID framework, a tuning algorithm is proposed, leveraging the machine's frequency response function (FRF) data. Frequency-domain analytical tools, including open-loop Higher-Order Sinusoidal Input Describing Functions (HOSIDFs) and the pseudo-sensitivity function from approximate closed-loop HOSIDFs, are applied during the optimization process. However, the introduction of the PI for the PCI leads to a trade-off, causing a reduction in phase margin or a decrease in the nonlinear benefits gained from the PCI. To overcome this limitation, a novel integrator called the Generalized First Order Reset Element-based Integrator (GFbI) is introduced. The GFbI, as a single integrator, has the ability to internally incorporate a PI within its structure, allowing it to achieve the desired zero steady-state error without externally introducing an additional linear integrator. This unique characteristic allows the GFbI to attain zero steady-state error, without being confined by the limitations associated with introducing an additional PI. Furthermore, the automated tuning method is proposed for GFbI, also permitting the use of machines' FRF data. Notably, with the novel GFbI structure and its tuning algorithm, the experimental data obtained from a wire bonder demonstrates a decrease (30.8%) in the root-mean-square of the settling error. Nevertheless, limitations in the reset control still exist and further work is required in order to achieve the full potential that this technique has to offer, and some recommendations on further work are given in the conclusion.

Preface

This research and its success would not have been possible without the support, encouragement, and guidance of numerous individuals whom I wish to acknowledge with profound gratitude. First and foremost, I extend my heartfelt appreciation to my daily advisor from company ASMPT, Luke van Eijk, whose expertise, absolute attention to details, insightful feedback, and especially patient guidance have been invaluable to this research journey and been the shaping force behind my career. Equally, I am also deeply thankful to my daily advisor from TU Delft, Xinxin Zhang. Her exceptional mathematical skills in control help me solid the control theory and build my deep ambition in mathematically analyzing the performance and exploring the essence of the system. Through the guidance of Xinxin and Luke, I have built a solid foundation in analysis as a structural and critical way. Furthermore, I am deeply graceful to my mentor from ASMPT, Dragan Kostić. His rich industrial experience and extensive knowledge have been invaluable sources of insight. He leveraged me several practical wisdom that assists me fill some gap between theory and practical performance prediction of reset control system. Dragan's consistent support and mentorship have been vital in ensuring the smooth progress of this research. Additionally, I want to express my sincere gratitude to my mentor from TU Delft, Hassan Hossenia. He possesses deep expertise in this research about reset control and has offered invaluable feedback on my work. His guidance in presenting practical results in an academic manner has not only ensured the scientific rigor of this work but has also strengthened my grasp of control theory and improved my critical and comprehensive thinking abilities. The commitment demonstrated by these four supervisors towards my academic development has made an enduring impact on both this thesis and my journey in the field of control.

Furthermore, I would like to express my gratitude to all the employees of ASMPT's mechatronic system group. Our discussions during company walks and lunch breaks have been invaluable for exploring control-related topics. Additionally, I've gained insights into cutting-edge control techniques through biweekly meetings with fellow control students. These interactions have significantly expanded my perspective. I also want to extend my heartfelt appreciation to my classmate, Xi Chen, who is studying electrical engineering at TU Delft. Throughout this year, we have often studied together, and Xi's encouragement and kind assistance have helped me navigate challenging moments. A special acknowledgment goes to my parents and family. Their selfless and constant support have instilled confidence in me.

Lastly, I sincerely thank each committee member for their time devoted to this thesis defense.

Yixuan Liu

15/08/2023

Contents

Contents **iv**

1 INTRODUCTION **1**
1.1 Background . . . 1
1.1.1 The AB383 wire bonder and its Simscape model . . . 1
1.1.2 Wire bonding process . . . 2
1.2 Problem Definition . . . 3
1.2.1 Basics of LTI control . . . 3
1.2.2 Traditional Limitations of LTI Feedback Control . . . 5

2 LITERATURE REVIEW **7**
2.1 Potential Nonlinear Control Techniques for Breaking Linear Limitations . . . 7
2.1.1 Split-path nonlinear filters . . . 7
2.1.2 Reset control . . . 8
2.1.3 Hybrid integrator-gain system . . . 8
2.2 Definition of Reset Control . . . 9
2.3 Performance Prediction . . . 11
2.3.1 Open-loop performance prediction of reset control . . . 11
2.3.2 Closed-loop performance prediction of reset control . . . 12
2.4 Stability and Convergence . . . 18
2.5 Reset Control Elements . . . 18
2.6 Past Implementations of Reset Controllers on AB383 Wire Bonder . . . 23

3 PCI-PID AND PGFbI **27**

4 CONCLUSIONS AND FUTURE WORK RECOMMENDATIONS **48**
4.1 Conclusions . . . 48
4.2 Future work recommendations . . . 49

Bibliography **52**

Chapter 1

INTRODUCTION

The work in this thesis is the result of a collaboration between the Technology University of Delft and the company ASMPT. ASMPT is a leading global supplier of hardware and software solutions for the manufacture of semiconductors and electronics [1]. The Center of Competency of ASMPT in Beuningen, the Netherlands, is responsible for exploring new high-tech innovation opportunities for the full global ASMPT product. This chapter commences by exploring ASMPT's wire bonders and their tracking problems, establishing the contextual background for this thesis. Notably, these wire bonders currently rely on Linear Time-Invariant (LTI) controllers, which inherently inherit the constraints associated with LTI control. Consequently, the chapter proceeds to investigate these conventional LTI limitations, which constitute the core problem addressed within this thesis.

1.1 Background

The wire bonder produced by ASMPT is served for the back-end of semiconductor manufacturing industry, utilized for electrically connecting the microchips and other integrated circuits with the terminals of a chip package or other substrates [2]. This section focuses on one of the typical wire bonders used in this work, namely the AB383 wire bonder.

1.1.1 The AB383 wire bonder and its Simscape model

ASMPT's AB383 wire bonder and its isolated motion stage are depicted in Figure 1.1. The motion stage facilitates motion along the X-, Y-, and Z-axes, offering 3 Degrees of Freedom (DoF). To model the dynamics of the motion stage, a Simscape model is developed by ASMPT including a base frame, and individual X, Y and Z stages, as shown in Figure 1.2. The base frame with the huge mass is to provide the support and vibration isolation from the external world. X, Y and Z stages are responsible for modelling the motion along their respective axes. Since each DoF of the motion stages is controlled by a separate actuator, the dynamics along the X-, Y- and Z-axis could be approximately treated as independent Single-Input Single-Output (SISO) systems. In this work, the dynamics of the motion along X-axis is focused. In this context, the input represents the applied force on the X stage, while the output corresponds to the displacement of the X stage. Moreover, it is notable that the Simscape model is based on the linearization of the nonlinear dynamics equation at different positions, therefore the nonlinearity of the practical machine cannot be fully captured.

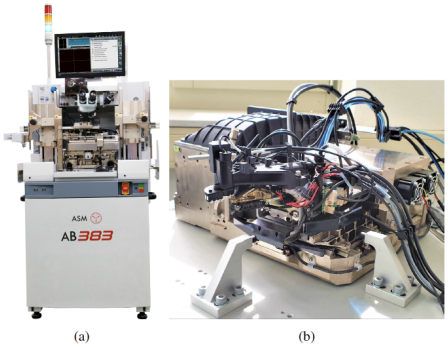

Figure 1.1: Reference signal for one movement of end-effector.

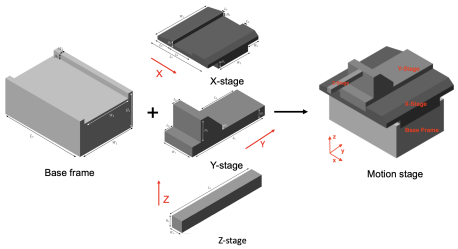

Figure 1.2: Reference signal for one movement of end-effector.

1.1.2 Wire bonding process

To further understand the working principle of a wire bonder, the wire bonding process is introduced. A complete wire bonding cycle is achieved based on the cooperation of three components, which are end-effector, support platform, and wires as shown in Figure 1.3. The wire bonding process is illustrated in Figure 1.4. In Figure 1.4-1, the end-effector is originally connected with the bonded wire. Subsequently, in Figure 1.4-2, the end-effector attaches the desired bonded region to create the first electronic bond by heat (thermo-compression) or ultrasound energy [2]. From Figure 1.4-2 to Figure 1.4-3 and to Figure 1.4-4, the end-effector travels to the second interested region to generate another bond for fixing the wire. Ultimately, one complete bonded process is finished in Figure 1.4-5, and restored to Figure 1.4-1 for the next bonding cycle.

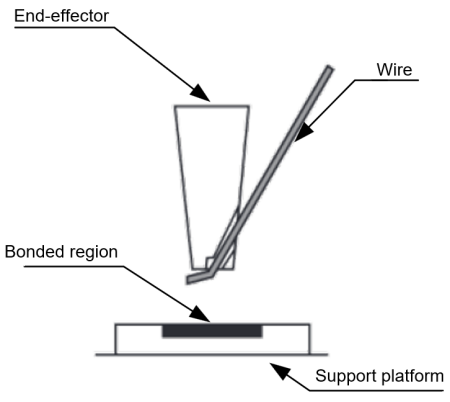

Figure 1.3: Components for wire bonding process [2].

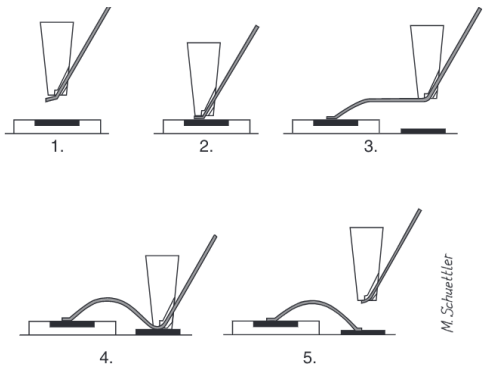

Figure 1.4: Illustration of wire bonding process [2].

The process depicted from Figure 1.4-2 to Figure 1.4-3 is a central focus of this work, and this phase could be affiliated with the problem of motion control and tracking a desired trajectory. In terms of the reference trajectory provided by ASMPT in Figure 1.5, it includes the tracking section(1), settling section(2), and steady-state section(3). The tracking section corresponds to Figure 1.4 from 2 to 3, during which the end-effector follows a designed trajectory. However, after the tracking section is completed and the end-effector reaches a specific position, oscillations are still exhibited, which is referred to as the settling section. Lastly, in the steady-state section, the end-effector remains stable without oscillations, holding a fixed position. Typically, the end-effector should pass through the steady-state section where the error is reduced to zero. However, traversing the entire steady-state section might introduce unnecessary delays. To address this, ASMPT defines a permissible error bounds, as illustrated in Figure 1.5. As long as the error signal remains within this bound, the system proceeds to the second bonding stage.

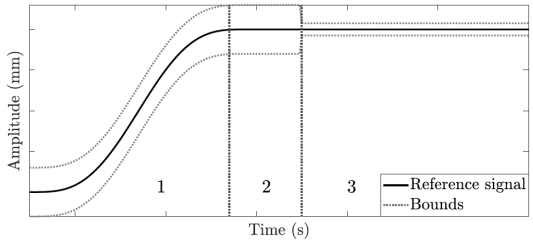

Figure 1.5: Reference signal for one movement of end-effector [3].

1.2 Problem Definition

1.2.1 Basics of LTI control

A typical and general control system is depicted in Figure. 1.6, in which C_{ff} is the feedforward controller, C_{fb} is the feedback controller and P is the plant. In addition, $r \in \mathbb{R}$ is the reference signal, $d \in \mathbb{R}$ is the disturbance signal, $n \in \mathbb{R}$ is the noise signal, $y \in \mathbb{R}$ is the true output signal, $y^* = y + n$ is the measured output, and $e = r - y^*$ is the error signal. Assuming no feedforward controller in the system and assuming C_{fb} and P are Linear-Time-Invariant (LTI) SISO systems, the open-loop transfer function is expressed as $L(s) = C_{fb}(s)P(s)$, with $s \in \mathbb{C}$ being the Laplace variable. In terms of the closed-loop analysis of the system, the sensitivity function $S(s)$ and complementary sensitivity function $T(s)$ are defined as

$$S(s) = \frac{\mathscr{L}(e)}{\mathscr{L}(r)} = \frac{\mathscr{L}(y)}{\mathscr{L}(d)} \frac{1}{P(s)} = \frac{1}{1 + L(s)}, \tag{1.1}$$

$$T(s) = \frac{\mathscr{L}(y)}{\mathscr{L}(r)} = -\frac{\mathscr{L}(y)}{\mathscr{L}(n)} = \frac{L(s)}{1 + L(s)}, \tag{1.2}$$

where $\mathscr{L}(x)$ represents the Laplace transform of $x \in \mathbb{R}$.

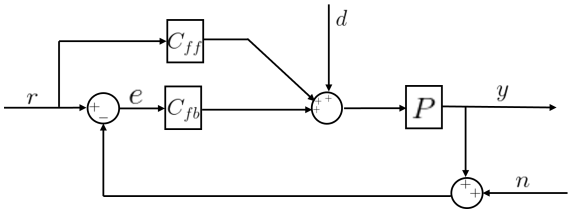

Figure 1.6: General control system architecture.

In terms of the reference tracking problem, the goal of the control system is to track a desired reference signal while attenuating undesired disturbance and sensor's noise. In other terms, the ideal control system will result in $y = r$. Attenuating disturbances requires $|\frac{\mathscr{L}(y)}{\mathscr{L}(d)}| \approx 0$. Based on (1.1), this requirement could be achieved only when $|L(j\omega)| \gg 1$, with $j = \sqrt{-1}$ and $\omega \in \mathbb{R}_{>0}$ being the frequency, since P cannot be altered. Decent tracking performance requires $|\frac{\mathscr{L}(y)}{\mathscr{L}(r)}| \approx 1$, also leading to $|L(j\omega)| \gg 1$ according to (1.2). On the other hand, noise suppression necessitates $|\frac{\mathscr{L}(y)}{\mathscr{L}(n)}| \approx 0$, thus constraining $|L(j\omega)| \ll 1$ based on (1.2). It is evident that the requirements for $|L(j\omega)|$ cannot be satisfied simultaneously for all ω. However, for mechanical systems, the noise usually acts at high frequencies, while disturbances usually act at lower frequencies [4]. Therefore, $|L(s)| \gg 1$ is usually required at low frequency range, and $|L(s)| \ll 1$ is required at high frequency range. Based on the above reasoning and requirements, loop-shaping technique is proposed for controller design in which the desired closed loop performance is achieved by shaping the open and closed loop transfer functions in the frequency domain [4]. Based on the loop-shaping technique, the open-loop transfer function should be shaped with the following characteristics as:

- exhibiting high magnitude at low frequencies for decent tracking and disturbance rejection
- having sufficient phase margin to ensure stability and robustness
- presenting low magnitude at high frequency for noise rejection

One of the widely used LTI feedback controllers in industry is PID controller. The PID controller could be typically represented by:

$$C_{PID} = \underbrace{k_P}_{\text{P}} \underbrace{\left(1 + \frac{\omega_{i-\text{PI}}}{s}\right)}_{\text{I (PI filter)}} \underbrace{\left(\frac{\frac{s}{\omega_d} + 1}{\frac{s}{\omega_t} + 1}\right)}_{\text{D (lead filter)}}, \tag{1.3}$$

where $k_P \in \mathbb{R}$ is the proportional gain, $\omega_{i-\text{PI}} \in \mathbb{R}_{>0}$ is the corner-frequency of Proportional Integrator (PI), and $\omega_d, \omega_t \in \mathbb{R}_{>0}$. Regarding discussing the function of PID in the frequency domain, k_P guarantee the sufficient bandwidth of the system, and the PI ensures the high open-loop magnitude at the low frequency range, thereby suppressing low-frequency disturbances. Moreover, in terms of the time-domain performance, the incorporation of the PI enables a system that initially cannot achieve zero steady-state error to attain such error-free performance. In addition, the lead filter is employed to provide the phase lead majorly within the frequency range $[\omega_d, \omega_t]$, thereby ensuring the sufficient phase margin and robustness of the system. The phase provided by the PID controller in (1.3) at the open-loop cross-over frequency is discussed in [5] as

$$\phi = \tan^{-1}\frac{\omega_{bw}}{\omega_d} - \tan^{-1}\frac{\omega_{bw}}{\omega_t} - \tan^{-1}\frac{\omega_{i-\text{PI}}}{\omega_{bw}} \tag{1.4}$$

Based on loop-shaping methods, the rules of thumb [5] [6] are proposed for tuning a PID controller in (1.3), which are

$$k_P \approx \frac{1}{3|P(\omega_{bw})|},\ \omega_{i-\text{PI}} = \frac{1}{10}\omega_{bw},\ \omega_d = \frac{1}{3}\omega_{bw},\ \omega_t = 3\omega_{bw}, \tag{1.5}$$

with $\omega_{bw} \in \mathbb{R}_{>0}$ being the bandwidth defined as the open-loop cross-over frequency of the control system. Tuning of PID controller could be simplified by the rule of thumb in (1.5), via relating multiple parameters of a PID controllers to one parameter ω_{bw}. Moreover, the factor 3 in k_P, ω_d and ω_t is chosen to provide about 53° phase at the frequency ω_{bw} and, if a higher phase margin is required, this factor can be increased.

1.2.2 Traditional Limitations of LTI Feedback Control

The fundamental limitations for a LTI system represents that there is always a trade-off between the improvement of reference tracking, and deterioration in noise amplification and robustness. This trade-off will be explained by Bode's gain-phase relationship from open-loop perspective and water-bed effect from closed-loop perspective.

Bode's gain-phase relationship

Bode's gain-phase relationship describes the LTI controllers' limitation from the open-loop perspective. Based on the loop-shaping technique, the magnitude of $L(s)$ is supposed to be possibly large at the low frequency, while $|L(s)|$ should be relatively low at the high frequency range. Therefore, the slope around bandwidth in magnitude plot should be as small as possible. Nevertheless, Bode's gain-phase relationship demonstrates that a $-20n$ dB/decade ($n \in \mathbb{R}$) slope in magnitude plot results in the phase lag of $n90°$ [7] [8], indicating that the increase of $|L(s)|$ at low frequency range or its attenuation at high frequency range for the fixed bandwidth could result in undesired increase of phase lag, which negatively effects the system's robustness (phase margin) and could potentially lead the system to be unstable. Vice versa as depicted in Figure 1.7, when the plant controlled by a LTI controller, the phase margin is increased, but the tracking and noise rejection ability are both decreased. In short, Bode's gain-phase relationship describes that it is impossible to improve the disturbance rejection and the noise rejection, and the system robustness simultaneously.

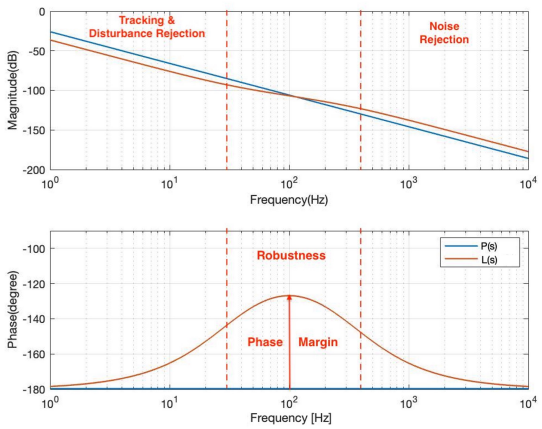

Figure 1.7: Bode plot of a mass plant ($P(s)$), and its $L(s)$ with a PID controller.

Water-bed effect

Based on Section 1.2.1, $|S(j\omega)|$ should be smaller than 0 dB at the low frequency range to ensure decent tracking ability, while $|S(j\omega)| \approx 0$dB for decent noise rejection ability. However, water-bed effect explains that it is theoretically impossible for $|S(j\omega)| \leq 0$dB at all frequencies. This effect could be mathematically explained by Bode's sensitivity integral [7], which is

$$\int_0^\infty \ln(S(j\omega))\ \mathrm{d}\omega = 0, \tag{1.6}$$

Figure 1.8 graphically illustrates the water-bed effect, and S_1 is defined as the area between the sensitivity curve below 0dB and horizontal axis. S_1 is regarded as the desired ares as it represents the suppression of low-frequent disturbances and the commendable tracking abilitiy. However, S_2 is considered as the area between the curve above 0db and horizontal axis, representing the undesired amplification of noise at high frequency. According to (1.6), $S_1 = S_2$, indicating that the improvement of tracking abilities and disturbance suppression have to cause the reduction of noise

rejection ability. In addition, resulted by the improvement in tracking, the increase in S_2 could also bring out the reduction of robustness, related to the modulus margin defined as the maximum value of the sensitivity function. Last but not least, the water-bed effect could be applied for the most of motion control systems, whose the degree of denominator for $L(s)$ is relatively at least 2 higher than its numerator. To sum up, water-bed effect describes the trade-off of LTI controllers between tracking ($|S(jw)| < 1$), noise rejection ($|S(jw)| > 1$) and robustness (modulus margin).

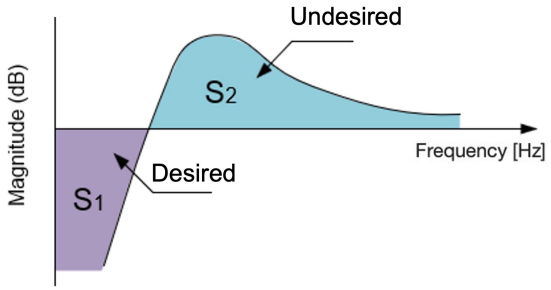

Figure 1.8: Sensitivity function.

Chapter 2

LITERATURE REVIEW

2.1 Potential Nonlinear Control Techniques for Breaking Linear Limitations

In order to break inherent limitations of LTI control, several state-of-art nonlinear techniques were proposed, such as Split-Path Nonlinear (SPAN) filters [9], Hybrid Integrator-Gain Systems (HIGS) [10], and reset control [11], etc. This chapter will delve into the fundamental principles, disadvantages, and advantages underlying these three nonlinear control techniques.

2.1.1 Split-path nonlinear filters

In contrast to the associated magnitude and phase properties of LTI controllers, the principal design philosophy of a SPAN filter is to split the magnitude and phase properties of a filter to achieve separate design and provide more design flexibilities. One of the main applications of SPAN filters is to design a nonlinear integrator, which is called SPAN integrators (SPANI) [12]. Regarding its advantage, SPANI could perform zero phase lag between the input and the first-order harmonic of its output [13], in comparison to the 90 degrees phase lag of linear integrators. As an extension of SPANI, Filtered Split-Path Nonlinear Integrator (F-SPANI) could be designed to achieve phase lead between the input and the first-order harmonic of its output [14]. However, subject to a single harmonic input, the output signal of F-SPAN integrator exhibits the properties of discontinuity and non-smoothness, as depicted in Figure 2.1. Besides, the further application of SPAN filter technique and its extensions in industry necessities analytical frequency-domain performance prediction methods to facilitate loop-shaping.

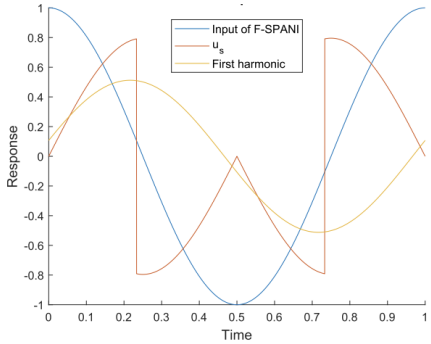

Figure 2.1: Output of a F-SPANI subject to a 1Hz harmonic input with amplitude 1 [13].

2.1.2 Reset control

The concept of reset control is to reset the states of a linear element to a certain value when its input satisfies a certain condition [11]. The first reset element Clegg Integrator (CI) is innovated to reset the state of a linear integrator to zero when its input signal hits zero [11]. CI could reach a lower phase lag of 38 degrees between the input and the first-order harmonic of output signal, compared to the traditional linear integrator with 90 degrees phase lag. Regarding the comparison of the output signals between SPANI and CI through Figure 2.1 and Figure 2.2, it is worth noting that although they both have two jumps in one period, the output of CI is smooth between two jumps while the output signal of SPANI is not. In addition, state-of-art researches focusing on stability criteria allowing the utilization of the machine's frequency response function (FRF) [15] [16], as well as the development of accurate closed-loop performance prediction methods [17] [18] [19] and reset structures [20] [21], have made reset control more comprehensive and feasible for industrial implementation. A comprehensive discussion of reset control will be presented in the upcoming sections.

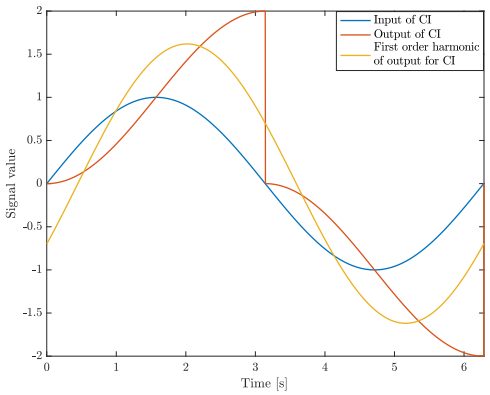

Figure 2.2: Output of CI and its first-order harmonic, with being subject to a sinusoidal input with the frequency 1rad/s and amplitude 1.

2.1.3 Hybrid integrator-gain system

HIGS is developed based on the reset control [22]. The main difference from reset control is that HIGS enforces the sign of an integrator output as to be consistent with its input sign. Similar to reset control, HIGS reaches a lower phase lag of 38 degrees between the input and the first-order harmonic of output signal, compared to the traditional linear integrator. Similar to SPANI and CI, HIGS nonlinearizes a linear integrator and offers improvement on it. In comparison to the output of SPANI in Figure 2.1, CI in Figure 2.2 and HIGS in Figure 2.3, HIGS is the only element among the three that lends a continuous output, although it is still non-smooth. Nonetheless, in contrast to reset control, the closed-loop performance of HIGS currently can only be predicted by a less accurate method called describing function (DF), and more accurate prediction method Higher-Order Sinusoidal Input Describing function (HOSIDF) is not supported for HIGS. Therefore, in terms of closed-loop performance analysis, the accuracy of HIGS is relatively lower compared to the reset control.

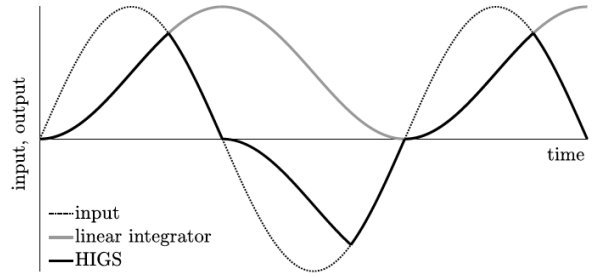

Figure 2.3: Comparison of HIGS and linear integrator [22].

After discussing the SPAN filter, reset control and HIGS, it is pertinent to conduct a comparative analysis between these three solutions to break traditional LTI limitations. While these three nonlinear control techniques share a common approach as reducing the phase lag of linear integrators, they possess distinct characteristics respectively. Although SPAN filters could provide improved integrator behavior with zero phase lag based on DF analysis, their lack of frequency-domain performance prediction hinders the utilization of simple loop-shaping tuning method, obstructing the application of SPAN in industry. Besides, the discontinuity and non-smoothness of SPANI output could pose challenges in ensuring stability. Consequently, additional research is necessary for its industry-wide implementation. In terms of the comparison between HIGS and reset control, although reset control exhibits discontinuity in the output signal, it could be remedied by continuous reset (CR) element [20]. The problem of non-zero steady-state error for reset control could be eliminated by adding an extra linear integrator and PI+CI structure (Proportional Integrator + Clegg Integrator) [23] . In addition, state-of-art researches [19] [18] in reset control provide accurate closed-loop prediction methods in frequency domain. Therefore, in spite of some drawbacks, due to the availability of stability guarantee in frequency domain, accurate closed-loop performance prediction and various reset structures, reset control is a preferred technique for industries to break traditional limitations of LTI control and improve machines' performance. Therefore, this thesis work will apply the reset control technique to ASMPT's wire bonder for improving the performance of the machine.

2.2 Definition of Reset Control

The definition of SISO reset controllers is portrayed in the following equation [24]

$$\mathscr{R} = \begin{cases} \dot{x_r}(t) = A_r x_r(t) + B_r e_r(t), & if(x_r(t), e_r(t) \notin \mathscr{M} \\ x_r(t^+) = A_\rho x_r(t), & if(x_r(t), e_r(t) \in \mathscr{M} \\ u_r(t) = C_r x_r(t) + D_r e_r(t), \end{cases} \tag{2.1}$$

where $e_r(t) \in \mathbb{R}$ is the input of the reset controller, $x_r(t) \in \mathbb{R}^{n_r \times 1}$ is the state of the reset controller $\mathscr{R}$, and $u_r(t) \in \mathbb{R}$ is the output of the reset controller, with n_r representing the number of states of $\mathscr{R}$. $A_r \in \mathbb{R}^{n_r \times n_r}$, $B_r \in \mathbb{R}^{n_r \times 1}$, $C_r \in \mathbb{R}^{1 \times n_r}$ and $D_r \in \mathbb{R}$ stand for the state-space matrices representing the base linear system (BLS) of $\mathscr{R}$. The transfer function of BLS denoted as $\mathscr{R}_{BLS}$ could be derived as

$$\mathscr{R}_{BLS} = C_r(sI - A_r)^{-1}B_r + D_r. \tag{2.2}$$

In addition, $A_\rho \in \mathbb{R}^{n_r \times n_r}$ is the reset matrix whose elements on diagonal determine the state values after being reset. The matrix A_ρ is usually a diagonal matrix, expressed as

$$A_\rho = \begin{bmatrix} \gamma & \\ & I_{n_R} \end{bmatrix}, \tag{2.3}$$

where $\gamma = \text{diag}(\gamma_1, \gamma_2, \gamma_3, ..., \gamma_r)$, $\gamma_i \in [-1, 1]$, and $\gamma_i = 1$ results in a corresponding linear controller. From the matrix expression, γ defines the state values after reset action, while I_{n_R} is corresponding to non-reset states, and n_R represents the number of non-reset states. Therefore, based on the definition of (2.1), it is supposed to be perceived that the first equation explains the base-linear dynamics. The second equation denotes the reset action characterized by jump dynamics, while the third equation symbolizes the output of the reset controller.

In terms of the trigger of reset action, the reset condition related to the reset surface $\mathscr{M}$ in (2.1) would be discussed further. There are several different reset conditions, and some recently emerged conditions depend on reset time intervals and fixed reset time instants [25] [26]. However, this thesis work would apply the traditional reset condition as zero-crossing law, since this condition allows the frequency-domain performance prediction in both open- and closed-loop. Zero-crossing law defines the occurrence of reset when the input of the reset controller $e_r(t)$ hits zero. Mathematically, the reset surface $\mathscr{M}$, which defines the reset condition is formulated as the following for the traditional zero-crossing law [24]:

$$\mathscr{M} := \{e_r(t) = 0\} \cap \{I - A_\rho x_r(t) \neq 0\}, \tag{2.4}$$

where the condition $I - A_\rho x_R(t) \neq 0$ ensures the prevention of the unnecessary redundant resets when the state of the element is already zero.

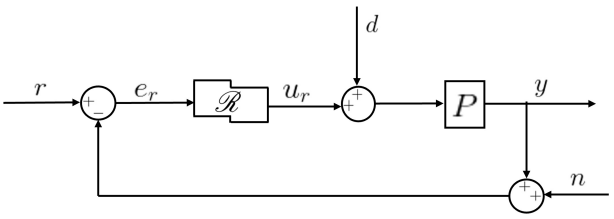

Figure 2.4: General reset control system.

After discussing the definition of a reset controller, the description of a whole Reset Control System (RCS) as depicted in Figure 2.4 is subsequently introduced. Firstly, the state-space expression of plant P is defined as

$$P = \begin{cases} \dot{x_p}(t) = A_p x_p(t) + B_p u(t), \\ y_p(t) = C_p x_p(t), \end{cases} \tag{2.5}$$

where $A_p \in \mathbb{R}^{n_p \times n_p}$, $B_p \in \mathbb{R}^{n_p \times 1}$, $C_p \in \mathbb{R}^{1 \times n_p}$ are the state-space matrices of the plant, with n_p being the number of plant states. After neglecting external input signals $r_{(t)}$, $d_{(t)}$ and $n_{(t)}$, the state-space equation of the RCS by combining (2.1) and (2.5) is provided as [27]

$$\bar{\mathscr{R}} = \begin{cases} \dot{x}(t) = A_{cl} x(t), & x \notin \bar{\mathscr{M}} \\ x(t^+) = A_{\rho cl} x(t), & x \in \bar{\mathscr{M}} \\ y(t) = C_{cl} x(t), \end{cases} \tag{2.6}$$

where $x^T = [x_r^T,\ x_p^T] \in R^{n_s}$, and $n_s = n_r + n_p$ is the number of states of $\bar{\mathscr{R}}$. $\bar{\mathscr{M}} := \{x \in \mathbb{R}^{n_s} | C_{cl} x = 0\}$ is the set of reset instants satisfying zero crossing law, where reset instants are defined as the

time when the input of reset controller hits zero. At the end, the state-space matrices for $\bar{\mathscr{R}}$ is derived as [27]

$$A_{cl} = \begin{bmatrix} A_r & -B_r C_p \\ B_p C_r & A_p \end{bmatrix}, A_{\rho cl} = \begin{bmatrix} A_\rho & \\ & I \end{bmatrix}, C_{cl} = \begin{bmatrix} 0 & C_p \end{bmatrix}, \tag{2.7}$$

2.3 Performance Prediction

Performance prediction of reset controllers is one of the noteworthy sections, as it plays a pivotal role in tuning controller parameters during the design process. In order to allow the simple loop-shaping technique be applicable for reset controller design, several performance prediction methods of RCS are develop in frequency-domain for both open- and closed-loop scenarios. This chapter will discuss the performance prediction methods in frequency domain for the reset controllers utilizing the traditional zero-crossing law.

2.3.1 Open-loop performance prediction of reset control

In reference to a reset controller defined in (2.1) subjected to a sinusoidal input $e_r(t) = A_0 \sin(\omega t)$ with $A_0 \in \mathbb{R}_{>0}$ and $\omega \in \mathbb{R}_{>0}$, the nonlinearity of the RCS results in the output of the reset controller being periodic, but not a single harmonic. By applying Fourier series analysis, the output of $\mathscr{R}$ can be decomposed into the first-order harmonic with the same frequency as the input and higher-order harmonics with frequencies as multiples of the input harmonic. The DF $H_1(\omega)$ of a reset controller is employed to predict its performance. It resembles the Bode plot of an LTI system, and is defined as the ratio between the Fourier transform of the first harmonic of u_r and the Fourier transform of the input, where the input is a sinusoidal of a certain frequency [28]. However, the predicted accuracy of DF is limited due to the neglection of higher-order harmonics of u_r. Therefore, a more precise prediction method HOSIDF $H_n(\omega)$ is proposed for reset controller in [17] to improve the prediction accuracy. $H_n(\omega)$ could be analytically calculated by [17] [29]

$$H_n(\omega) = \begin{cases} C_r(j\omega I - A_r)^{-1}(I + j\Theta_D(\omega))B_r + D_r, & for\ n = 1 \\ C_r(jn\omega I - A_r)^{-1}(j\Theta_D(\omega))B_r, & for\ odd\ n > 1 \\ 0, & for\ even\ n > 1 \end{cases} \tag{2.8}$$

with

$$\begin{aligned} &\Lambda(\omega) = \omega^2 I + A_R^2, \\ &\Delta(\omega) = I + e^{(\frac{\pi}{\omega} A_R)}, \\ &\Delta_r(\omega) = I + A_\rho e^{(\frac{\pi}{\omega} A_R)}, \\ &\Gamma_r(\omega) = \Delta_r^{-1}(\omega) A_\rho \Delta(\omega) \Lambda^{-1}(\omega), \\ &\Theta_D(\omega) = \tfrac{-2\omega^2}{\pi} \Delta(\omega)[\Gamma_r(\omega) - \Lambda^{-1}(\omega)]. \end{aligned}$$

To visually comprehend the distinction in prediction between DF and HOSIDF, a comparative analysis is conducted for open-loop performance prediction. In Figure 2.5, it is evident that the prediction generated by the HOSIDF approach closely matches the actual output of the reset controller $\mathscr{R}$, surpassing the prediction derived from the DF method.

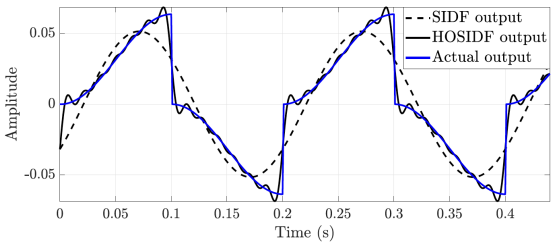

Figure 2.5: Output of CI subject to a 5 Hz sinusoidal input with amplitude 1, its redicted output based on DF (SIDF) and HOSIDFs [3].

2.3.2 Closed-loop performance prediction of reset control

Loop-shaping technique for reset control not only requires the accurate prediction of open-loop performance, but also necessitates the connection between open-loop and closed-loop to have a relatively accurate prediction of closed-loop performance. Although DF approach could be applied to perform closed-loop performance prediction, this method does not consider higher-order harmonics within the RCS, resulting in less accurate prediction in frequency domain. Therefore, three closed-loop models (closed-loop model A, B and C) based on HOSIDF with increased prediction accuracy will be introduced in this section to promote the industrial application of reset control. Besides, the pseudo-sensitivity is defined for reset control.

Closed-loop model A

The first closed-loop performance prediction method of RCS by applying HOSIDF method was introduced in [17], and the model of RCS based on this method is shown in Figure 2.6. Closed-loop A achieves the higher prediction accuracy compared to DF approach by introducing the virtual harmonic generator to consider higher-order harmonics at the output of $\mathscr{R}$. Besides, there are also two additional elements in this closed-loop model, which are virtual harmonic separator and R_{bl}. Due to the model assumes that only the first-order harmonic at the input of $\mathscr{R}$ could pass through $\mathscr{R}$ [17], virtual harmonic separator is applied for separating the first-order harmonic with other higher-order harmonics. R_{bl} represents the BLS of the reset controller $\mathscr{R}$. In relation to the first-order harmonic at the input of $\mathscr{R}$, e_1 constantly passes through H_1 and P in Figure 2.6. As for n-th higher-order harmonic at the input of $\mathscr{R}$, at first, they are generated by e_1 passing through H_n and P in Figure 2.6. After this, e_n constantly passes through R_{bl} and P, and does not pass H_n any more since higher-order harmonics are not assumed to be reset in this model. Based on the above explanation of closed-loop A, the closed-loop sensitivity function provided in [17] could be analytically calculated as

$$S_n(\omega) = \begin{cases} \frac{E_1(\omega)}{R(\omega)} = \frac{1}{1+H_1(\omega)P(n\omega)}, & for\ n = 1 \\ \frac{E_n(\omega)}{R(\omega)} = \frac{-P(n\omega)H_n(\omega)}{1+R_{bl}(n\omega)P(n\omega)}, & for\ odd\ n > 1 \\ 0, & for\ even\ n > 1 \end{cases} \tag{2.9}$$

where $E_1(\omega), E_n(\omega) \in \mathbb{C}$ are the Fourier transform of the first order harmonic and n-th higher-order harmonic of error signal, and $R(\omega) \in \mathbb{C}$ is the Fourier transform of reference r, as depicted in Figure 2.6.

Although closed-loop model A provides performance prediction for RCS, the accuracy of this model is limited by its assumption that only the first order harmonic of the reset input results in reset, and higher-order harmonics of e are hence not considered to pass through $\mathscr{R}$. Besides,

another assumption, that RCS only resets two times per period, limits the applicability and generality of this model. In terms of counting reset times of a RCS, it is supposed to count the zero-crossing times per period at the input of $\mathscr{R}$, when the RCS reaches its steady state and zero-crossing law is used.

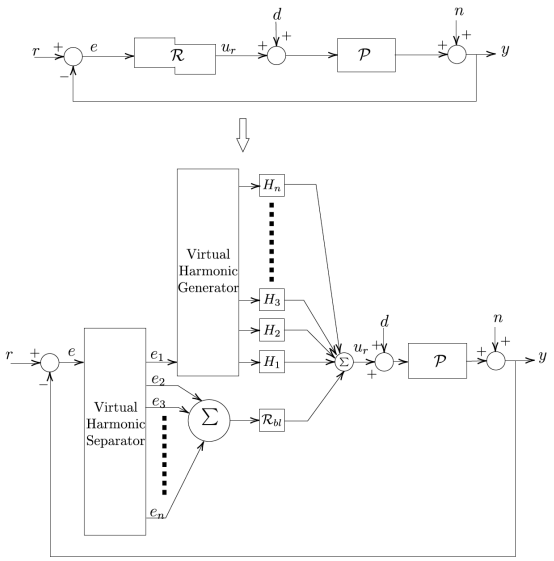

Figure 2.6: Closed-loop model A [17].

In short, closed-loop model A based on HOSIDF method and virtual harmonic separator provides the relatively accurate closed-loop prediction in the frequency domain. However, due to its assumptions, this model has limited accuracy and generality, and the following state-of-art models (closed-loop model B and C) are introduced for improving the closed-loop prediction accuracy of RCS.

Closed-loop model B (pulse-based model)

Pulse-based model was introduced in [19] to consider reset actions resulted by higher order harmonics at the input of $\mathscr{R}$. This model is based on the reclassification of the output of $\mathscr{R}$. For a reset controller defined in (2.1) subject to a sinusoidal input $e_r(t) = A_0\sin(\omega t)$, the steady-state output of the reset controller could be divided into linear and nonlinear parts, expressed as:

$$u_r(t) = u_{bl}(t) + q(t), \tag{2.10}$$

where $u_{bl}, q \in \mathbb{R}$ are the linear and nonlinear parts of u_r. The linear part of u_r is the output of the BLS of $\mathscr{R}$. As an example of CI, the nonlinear part of its output is a square wave as shown in Figure 2.7. Based on this new classification method, two transfer functions $R_L(\omega)$ and $R_{NL}(\omega)$ are proposed in [19] for predicting the performance of the reset controller in open-loop, in which $R_L(\omega)$ is the Fourier transform of $\frac{u_{bl}(t)}{e(t)}$, and $R_{NL}(\omega)$ is the Fourier transform of $\frac{q(t)}{e(t)}$ (assuming $e_r(t) = e(t)$). By applying these two transfer functions, a novel open-loop model of reset controller is built as illustrated in Figure 2.8. Because the fundamental frequency of $q(t)$ is still equal to the input frequency or the frequency of $u_{bl}(t)$, it is notable that the first-order harmonic of $u_r(t)$ is combined by both the linear output $u_{bl}(t)$ and the first-order harmonic of $q(t)$. However, higher-order harmonics of $u_r(t)$ are only related to nonlinear output $q(t)$.

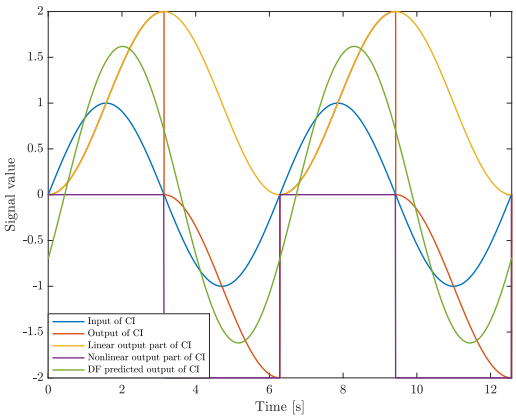

Figure 2.7: Linear and nonlinear parts of CI output, being subjective to a sinusoidal input with the frequency 1rad/s and amplitude 1.

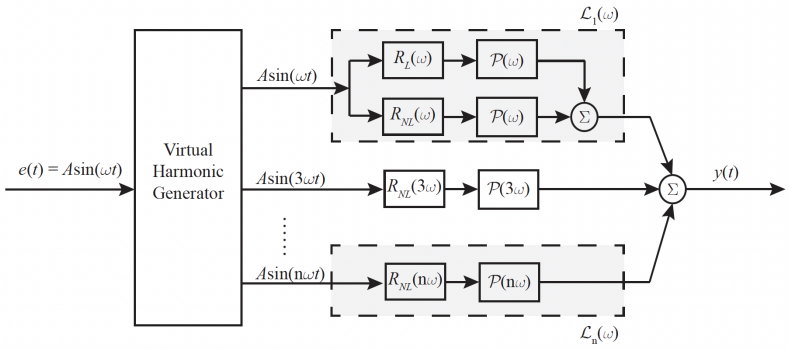

Figure 2.8: Open-loop HOSIDF model based on closed-loop model B [19].

Closed-loop model B provides a different perspective to model the open-loop performance of a RCS, and the open-loop performance prediction by closed-loop model B in Figure 2.8 is as accurate as the prediction by the open-loop model part (from $e(t)$ to $y(t)$) in Figure 2.6. In addition, in terms of the relationship between the two open-loop models in Figure 2.6 and Figure 2.8, the $H_1(\omega)$ in Figure 2.6 is equal to the superposition of $R_L(\omega)$ and $R_{NL}(\omega)$ in Figure 2.8. The $H_n(\omega)$ in Figure 2.6 is equivalent to $R_{NL}(n\omega)$ in Figure 2.8. After discussing the new classification method in open-loop, closed-loop model A could be reviewed to discuss the actual neglected output parts by model A. Not every parts of the higher-order harmonics of $u_r(t)$ are neglected in closed-loop model A, and in fact, only the nonlinear output parts corresponding to higher-order harmonics of $e(t)$ are neglected. The $u_{bl}(t)$ resulted by the higher-order harmonics of $e(t)$ are considered by R_{bl} of closed-loop model A as depicted in Figure 2.6.

After discussing the pulse-based model of RCS in open-loop, the closed-loop model B could be introduced to compensate the neglection of reset actions resulted from higher-order harmonics of $e(t)$, for achieving an improved prediction accuracy. In closed-loop model B, the parameter Γ is proposed in [19] to achieve such compensation, which is defined as

$$\Gamma = \frac{\sum_{n=1}^{\infty} q_n(t)}{q_1(t)} \quad [19], \tag{2.11}$$

where $q_1(t), q_n(t) \in \mathbb{R}$ are the nonlinear output part resulted by the first-order and n-th order

harmonic of $e(t)$. To be understandable, Γ is the nonlinear output part corresponding to the $e(t)$ divided by the nonlinear output part corresponding to the first-order harmonic of $e(t)$ (i.e. $e_1(t)$). The closed-loop model B of RCS defined in (2.6) is shown in Figure 2.9. The virtual harmonic separator could be continuously used in this model to simplify the calculation. Based on closed-loop model B, the nonlinear output parts resulted by higher-order harmonics of $e(t)$ could finally be considered by the multiplication of Γ with the nonlinear output part corresponding to the first-order harmonic of $e(t)$. Last but not least, Γ could be mathematically calculated by

$$\Gamma = 1/(1 - \frac{\sum_{n=3}^{\infty} \zeta(n\omega)\eta(n\omega)}{\eta(\omega)}) \quad [19], \tag{2.12}$$

with

$$\begin{aligned}
&\zeta(n\omega) = \tfrac{-|L_{NL}(n\omega)|}{1+|L(n\omega)|}, \\
&\eta(n\omega) = (A_\rho - I)\,|R_L(n\omega)|\,sin(l\pi + \angle(R_L(n\omega))), \\
&L(n\omega) = R_L(n\omega)P(n\omega), \\
&L_{NL}(n\omega) = R_{NL}(n\omega)P(n\omega).
\end{aligned}$$

In order to better understand the difference and the improvement of closed-loop model B compared to the closed-loop model A, the block diagram for closed-loop model B is recreated based on the closed-loop model A, as depicted in Figure 2.10. By comparing Figure 2.6 and Figure 2.10, it is straight to comprehend that closed-loop model B divides the output of the reset controller into nonlinear and linear parts, and adds Γ after the nonlinear output part resulted by $e_1(t)$. By considering the reset actions caused by the higher-order harmonics of $e(t)$ based on Γ, closed-loop model B could achieve the improved accuracy for predicting the closed-loop performance of $\bar{\mathscr{R}}$, compared to the closed-loop model A.

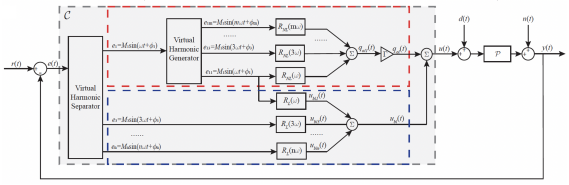

Figure 2.9: Closed-loop model B [19].

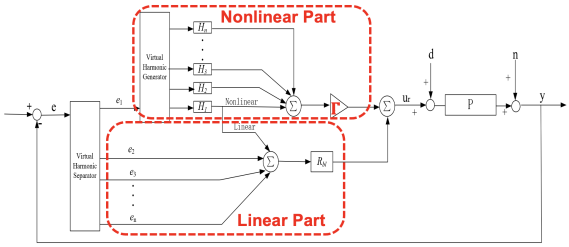

Figure 2.10: Closed-loop model B based on closed-loop model A.

Based on the closed-loop B illustrated in Figure 2.9, more accurate analytical method to calculate sensitivity function of RCS defined in (2.6) could be derived as

$$S_n(\omega) = \begin{cases} \frac{1}{1+L_O(\omega)P(n\omega)}, & for\ n = 1 \\ \frac{\Gamma L_{NL}(n\omega)}{1+L_O(n\omega)} \cdot \frac{1}{1+L(n\omega)}, & for\ odd\ n > 1 \\ 0, & for\ even\ n > 1 \end{cases} \tag{2.13}$$

where $L_O(n\omega) = L(n\omega) + \Gamma L_{NL}(n\omega)$. In addition, similar to closed-loop model A, closed-model B is also constrained by the assumption that there are only two reset instants per period when RCS reaches the steady-state. Therefore, when the system is subject to multiple resets, closed-loop model B provides limited prediction accuracy.

Closed-loop model C

Closed-loop model C proposed in [18] is based on the time-domain to analytically predict the closed-loop performance of RCSs. This model does not separately analyze the input and output of individual elements, such as $\mathscr{R}$ and plant, but basically concentrates on regarding every elements as a whole system, and performs time-domain study regarding the input $r(t)$ and output $y(t)$ relationship of this whole system. Fourier transform is applied for $r(t)$ and $y(t)$ to study the frequency-domain performance and derive the closed-loop transfer function at the end. By studying $r(t)$ and $y(t)$, the corresponding complementary sensitivity function $T_n(j\omega)$ could be derived firstly. Subsequently, by applying the relationship between complementary function $T_n(j\omega)$ and sensitivity function $S_n(j\omega)$ of RCS in (2.14), $S_n(j\omega)$ could be finally derived. In addition, there is a toolbox to implement the theory of closed-loop model C for predicting the RCS performance in frequency-domain.

$$T_n(j\omega) + S_n(j\omega) = \begin{cases} 1, & for\ n = 1 \\ 0, & for\ n > 1 \end{cases} \tag{2.14}$$

Regarding the advantages of closed-loop model C, similar to closed-loop model B, closed-loop model C also takes into account the reset actions resulting from the higher-order harmonics of the error signal $e(t)$. Moreover, this approach doesn't necessitate the assumption of two resets per period, which makes it more generalizable compared to closed-loop model B. However, closed-loop model C also comes with certain limitations. Firstly, it is constrained by the need for a parametric plant model and the requirement for approximations of plant parameters. This is because the analytical equations of closed-loop model C demand the state-space matrices of the plant model, making a parametric plant model essential. As for the second drawback, the calculation process is complex and time-consuming due to the fact that closed-loop model C is developed based on time-domain simulations. In addition, since closed-loop C is based on the time-domain simulation, which is computationally inefficient. Furthermore, due to the requirement for the state-space matrices of the plant, incorporating an accurate time delay as $e^{-t_d s}$ becomes challenging, where $t_d \in \mathbb{R}_{>0}$ represents the time delay of the system. Despite the limitation imposed by the state-space matrices of the plant, this theory is formulated and derived based on a continuous plant model. In Figure 2.11, a comparison is presented between the continuous plant without delay and a discrete plant with a delay using the AB383 Simscape model. It is evident that the two plant models exhibit noticeable differences in the phase plot. This discrepancy between the continuous and discrete plant models needs to be addressed. Consequently, interms of practical application, another issue lie in bridging the gap between a discrete plant model and a continuous plant model. An additional consideration is that, unlike closed-loop models A and B, closed-loop model C lacks a direct association with open-loop and closed-loop configurations. As a result, the loop-shaping technique cannot be directly applied through this model for reset control. In summary, despite the advantages of closed-loop model C, including high prediction accuracy and a well-developed toolbox, several challenges still persist. These challenges encompass accurately approximating the

impact of time delay and plant discretization, effectively implementing the loop-shaping technique, and ensuring computational efficiency.

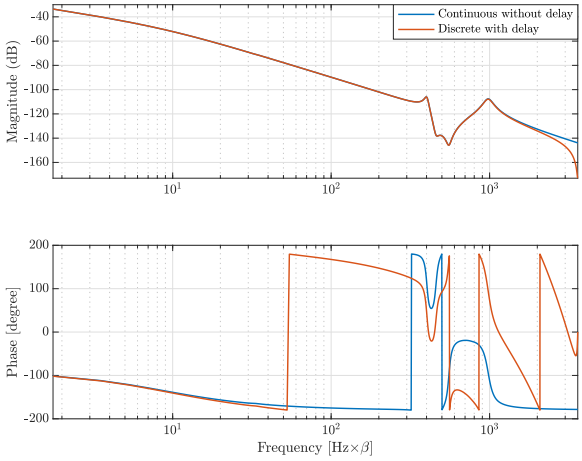

Figure 2.11: Comparison of the Ab383 wire bonder's Simscape model being continuous with delay and discrete with delay (due to the confidentiality, the frequency axis is scaled by a random constant β).

Comparison of three closed-loop models and pseudo-sensitivity

After discussing closed-loop models A, B, and C, a comprehensive comparison is presented in Table 2.1 to provide a deeper understanding of their characteristics. Both closed-loop models B and C exhibit enhanced accuracy compared to the closed-loop model A due to their consideration of reset actions resulted by the higher-order harmonics at the input of $\mathscr{R}$. When contrasting closed-loop models B and C, it becomes evident that closed-loop model B holds an advantage in terms of implementation simplicity and the feasibility of applying the loop-shaping technique. However, its accuracy is limited by the assumption of two reset times per period. On the contrary, closed-loop model C enjoys broader generalization but is accompanied by increased computational complexity and the necessity of a parametric plant model. Acquiring an accurate parametric model can be challenging for industrial machines. Furthermore, the complete theory underpinning closed-loop model B is not available within the scope of this thesis. Hence, taking into account the factors of utilizing the accurate machine's FRF and the feasibility of employing loop-shaping techniques, the choice was made to utilize closed-loop model A for performance prediction throughout this thesis.

Table 2.1: Comparison of closed-loop model A, B and C.

	Closed-loop model A (already implemented)	Closed-loop model B (To be implemented)	Closed-loop model C (To be implemented)
Reset times per period	Two reset times	Two reset times	Multiple reset times
Consider higher-order harmonics of reset input	No	Yes	Yes
Applicability of loop-shaping	Yes	Yes	No
Applied plant model	Machine spectrum(FRF) (accurate)	Machine spectrum(FRF) (accurate)	Parametric model (less accurate)

2.4 Stability and Convergence

After investigating the performance prediction of RCS, the stability of RCS should be concentrated. The H_β-condition in [24] [30] provides sufficient conditions for bounded input bounded state stability for the closed-loop RCS. H_β-condition states that the RCS defined in (2.6) is quadratically stable if and only if $\beta \in \mathbb{R}^{n_r}$ and a positive definite matrix $P_r \in \mathbb{R}^{n_r \times n_r}$ exist, such that the transfer function

$$H_\beta(s) := \begin{bmatrix} Pr & 0_{n_r \times n_{nr}} & \beta C_p \end{bmatrix} (sI - A_{cl})^{-1} \begin{bmatrix} I_{n_r} \\ 0 \end{bmatrix}, \tag{2.15}$$

is strictly positive real and subsequently a non-zero reset matrix A_{ρ_r} fulfills the condition

$$A_{\rho_r}^T P_r A_{\rho_r} \; - \; Pr \leq 0 \tag{2.16}$$

However, the H_β-condition necessitates the solving of complex linear matrix inequality (LMI), which necessitates a parametric plant model in state-space form rather than the highly accurate machine's FRF. Hence, H_β-condition is reformulated based on Nyquist stability vector (NSV) proposed in [15] in order to hinder solving LMI and directly apply the FRF data of plant. The details of the stability guarantee of RCS through NSV method are shown in the following.

Firstly, $O(j\omega)$ and $C_R(j\omega)$ are respectively defined as the FRF of the open-loop BLS and the reset element. Subsequently, the vector $\vec{\mathscr{N}}(\omega)$ is denoted as $\vec{\mathscr{N}}(\omega) = [\mathscr{N}_X, \mathscr{N}_Y]^T$, where

$$\mathscr{N}_X = \Re(O(j\omega)\kappa(j\omega)), \mathscr{N}_Y = \Re(\kappa(j\omega)C_R(j\omega)), \tag{2.17}$$

in which $\kappa(j\omega) = 1 + O^{'}(j\omega)$, and $O^{'}(j\omega)$ is defined as the conjugate of the complex $O(j\omega)$, and $\Re(.)$ represents the real part of a complex number. Then the RCS is uniformly bounded-input and bounded-output (UBIBS) stable if

$$(-\frac{\pi}{2} < \theta_1 < \pi) \wedge (-\frac{\pi}{2} < \theta_2 < \pi) \wedge (\theta_2 - \theta_1 < \pi) \text{ [15]}, \tag{2.18}$$

where $\theta_1 = min\angle\vec{\mathscr{N}}(\omega)$, and $\theta_2 = max\angle\vec{\mathscr{N}}(\omega))$.

2.5 Reset Control Elements

With accurate performance prediction methods, reset controllers could be properly designed to improve the system performance. During this chapter, several reset structures are introduced for designing a RCS to improve the performance of wire bonders. In addition, the reset elements discussed in this section are all based on the reset condition law as the "zero-crossing" law.

Clegg Integrator (CI) and Proportional Clegg Integrator (PCI)

As an origin of other reset elements, CI could be implemented by resetting a linear integrator, and other reset element could be achieved by combinations of CI and other linear elements. The BLS of CI is $A_r = 0$, $B_r = 1$, $C_r = 1$, $D_r = 0$, and the reset matrix of CI is $A_\rho = \gamma$. Based on the DF analysis, the advantage of CI lies in its less phase lag about 38 degrees compared to 90 degrees phase lag of linear integrators.

Similar to the transition from a linear integrator to CI, PCI with the corner frequency $\omega_{i-\text{PCI}} \in \mathbb{R}_{>0}$ is derived when a PI is reset. The BLS and reset matrix of the PCI are derived as $A_r = 0, B_r = \omega_{i-\text{PCI}}, C_r = 1, D_r = 1, A_\rho = \gamma$. It is concluded that there are two tuning parameters of a PCI,

which are $\omega_{i-\mathrm{PCI}}$ and γ. In relation to the comparison between PCI and PI, when ensuring the same $\omega_{i-\mathrm{PCI}}$ and $\omega_{i-\mathrm{PI}}$, the PCI has the advantage of less phase lag and higher open-loop gain as shown in Fig. 2.12, indicating a larger phase margin and more suppression of low-frequency disturbances in control systems. Among different PCI elements with the same $\omega_{i-\mathrm{PCI}}$, those with lower γ value exhibits more reset action and nonlinearity, resulting in greater reduction of phase lag and increase of open-loop gain, as depicted in Fig. 2.12. But as a part of the nonlinearity of PCI, undesired higher-order harmonics also increase as γ decreases, as illustrated by the 3rd HOSIDF in Fig. 2.12.

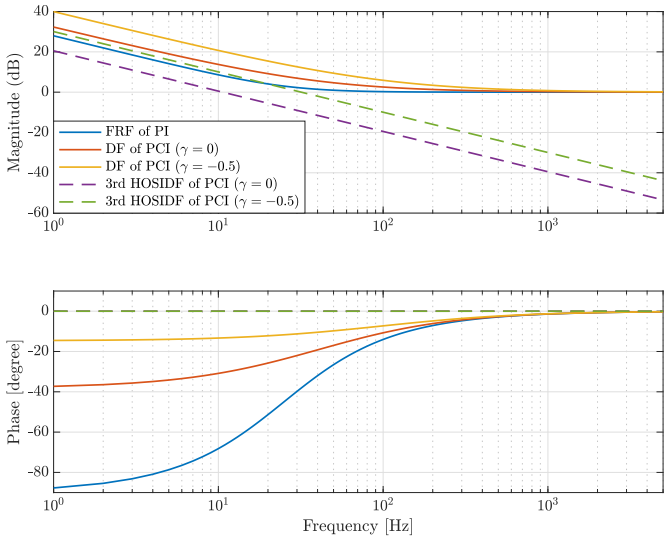

Figure 2.12: FRF of PI, DF and 3rd HOSIDF of PCI (with $\gamma = 0$ and $\gamma = -0.5$), and all PI and PCI filters are with the same corner-frequency as 25Hz.

PI+CI

Due to the drawback about the non-zero state error of a single PCI, PI+CI structure firstly introduced in [23], was proposed to solve such issue by adding an extra linear integrator. The PI+CI structure is presented in Figure 2.13, in which $k_p \in \mathbb{R}$ is the proportional gain, $\tau_i \in \mathbb{R}$ is the integral time constant, and $p_{reset} \in [0, 1]$ is the reset ratio. By means of the parallel connection between PI and CI, PI+CI structure could achieve the partial reset of a PI, which occupies the transfer function $k_p(1 + \frac{1}{\tau_i s})$. To be specific, when the reset ratio p_{reset} is 0, the structure is a PI controller without reset, and when p_{reset} is 1, the structure is a CI. Therefore, when $p_{reset} \in (0, 1)$, the structure could be interpreted as an integrator with the partial reset. There are two states of PI+CI, which are corresponding to the linear integrator and CI term [23]. Therefore the state-space matrices of PI+CI are

$$A_r = \begin{bmatrix} 0 & 0 \\ 0 & 0 \end{bmatrix}, B_r = \begin{bmatrix} 1 \\ 1 \end{bmatrix}, A_\rho = \begin{bmatrix} 1 & 0 \\ 0 & 0 \end{bmatrix}, C_r = \frac{k_p}{\tau_i}[1 - p_r \; p_r], \; D_r = kp \; [23]. \tag{2.19}$$

The advantage of PI+CI structure could be concluded from Figure 2.14. Compared to a linear integrator (p_{reset} is 0), partial reset integrator achieved by PI+CI structure could provide less phase lag and larger gain at low frequency, while zero-state error is also achieved simultaneously.

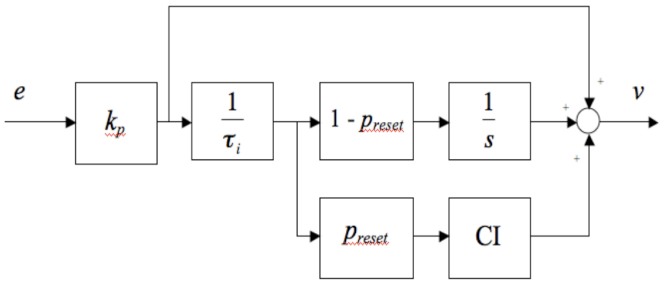

Figure 2.13: PI+CI structure [23].

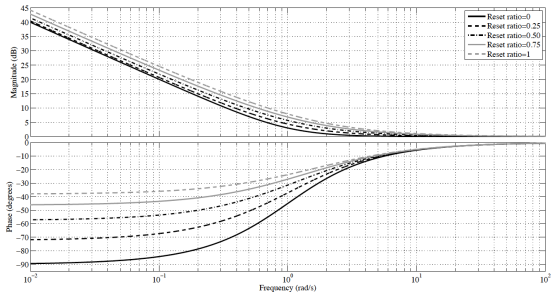

Figure 2.14: DF of PI+CI structure with different p_{reset} ($k_p = \tau_i = 1$) [23].

First Order Reset Element (FORE)

FORE was initially introduced in [8] by resetting the first-order low-pass filter. The BLS and reset matrix of FORE are followed by $A_r = -\omega_r$, $B_r = \omega_r$, $C_r = 1$, $D_r = 0$, and $A_\rho = \gamma$. The frequency behavior of FORE is present in Figure 2.15. In contrast to the linear low pass filter, FORE could achieve about 52 degree less phase lag at the high frequency range. In addition, a second-order low pass filter could either be reset to generate a second order reset element (SORE) [31]. However, SORE has two reset states, indicating more complex in tuning compared to FORE.

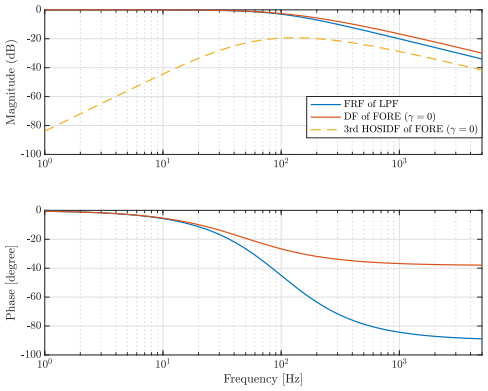

Figure 2.15: HOSIDF of FORE with corner frequency at 100Hz.

Constant in Gain Lead in Phase (CgLp)

CgLp is a state-of-art reset structure recently developed in [21]. CgLp could achieve the function about providing the phase lead to the system without increasing the magnitude (without loss of

noise rejection at high frequency). However, the traditional linear differentiator has to result in the reduction of noise rejection ability while involving phase lead, and therefore CgLp could be a potential replacement of linear differentiator for improving system performance. This extraordinary benefit of CgLp is achieved by series connection with a reset lag filter $\mathscr{R}(s)$ (FORE or SORE) and a linear lead filter $L(s)$ (the first-order linear lead filter F_l or the second order skewed notch filter F_{sn}), with the illustrated block in Figure 2.16. F_l and F_{sn} are expressed as,

$$F_l = \frac{\frac{s}{\omega_r}+1}{\frac{s}{\omega_f}+1}, \quad F_{sn} = \frac{\frac{s}{\omega_r}^2 + \frac{2s\beta_r}{\omega_r}+1}{\frac{s}{\omega_f}^2 + \frac{2s}{\omega_f}+1} \quad [21], \tag{2.20}$$

where the denominator parts are for proper transfer function, and therefore $\omega_f >> \omega_r$. Besides, due to the complexity of SORE, the series combination of FORE and the first-order lead filter are mainly focused to form a CgLp element. In addition, regarding the design of the CgLp, the parameter α is supposed to be appropriately selected, defined as the ratio between ω_r and the corner frequency of reset lag element. The DF of CgLp is shown in Figure 2.17. It could be known that FORE could compensate the increase in gain of a linear lead filter from ω_r to ω_f. On the other hand, due to the FORE's special property of less phase lag, the phase lead of the lead filter can not be fully eliminated, and therefore phase lead is still present. Moreover, compared to a linear lead filter, one additional advantage of CgLp is to achieve the reduced gain at high frequency (after ω_f in Figure 2.17) to ensure the suppression of noise signals.

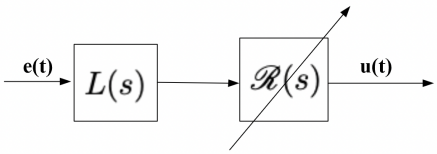

Figure 2.16: Block illustration of CgLp structure.

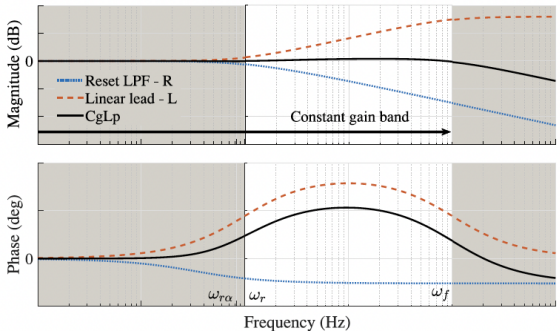

Figure 2.17: DF of CgLp achieved by FORE with the first-order linear lead filter [21].

Continuous Reset (CR) Element and Parallel CR

CR was firstly introduced as the series connection of elements in [20], including a reset element inserted between a linear lead filter $L(s)$ and lag filter $D(s)$ as shown in Figure 2.18, and $L(s)$ and $D(s)$ are expressed in [20] as

$$L(s) = \frac{\frac{s}{\omega_l}+1}{\frac{s}{\omega_h}+1}, \; D(s) = \frac{1}{\frac{s}{\omega_l}+1}. \tag{2.21}$$

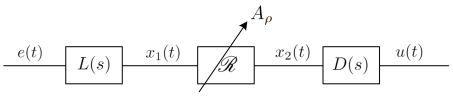

Figure 2.18: Block diagram of series CR structure.

As a lag filter, $D(s)$ is for lowering the HOSIDFs of the reset controller. $L(s)$ is to mainly cancel the influence of $D(s)$ on the base linear system. Consequently, added lead and lag elements nearly have no effect on the whole system SIDF, but only the HOSIDFs are affected [3]. The denominator of $L(s)$ is to realize a proper transfer function, and therefore in essence the equation $L(s) = D(s)^{-1}$ is supposed to be held by achieving $\omega_h >> \omega_l$. There are two main advantages of series CR. Firstly, CR structure could smooth the output of the reset controller, and change the less continuous system output to be instead continuous as shown in Figure 2.19. Concluded from Figure 2.20, another advantage is that CR provides a significant reduction in higher-order harmonics and therefore DF predicted result could be more accurate.

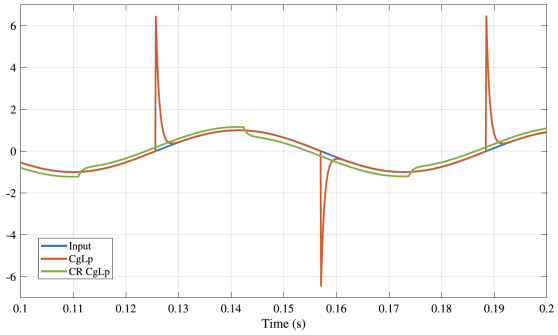

Figure 2.19: Comparison of the RCS output with and without series CR structure [20].

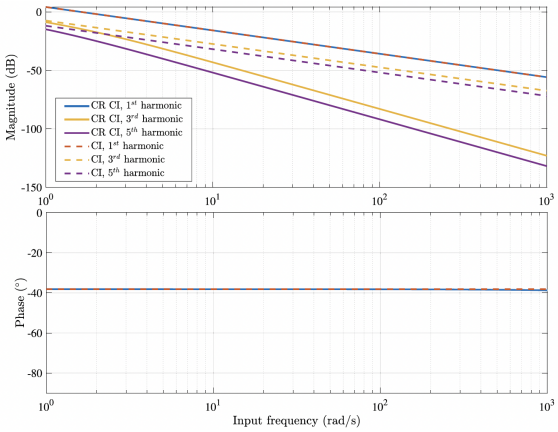

Figure 2.20: HOSIDFs of RCS with and without CR structure [20].

Although the advantages of CR are promising, during the practical implementation in discrete-domain, aliasing could amplify the error [3]. Additionally, the lead filter before the reset element could lead to the amplification of noise signal. Hence, a state-of-art structure called parallel CR was introduced in [3]. Parallel CR continues to use $D(s)$ after the reset element to reduce HOSIDFs as shown in Figure 2.21. Instead, the lead element is parallel installed to reset element $\mathscr{R}$ for avoiding the amplification of error by series connection of lead element. Illustrated by Figure

2.21, C_{par} is expressed as $\mathscr{R}(L-1)$, and C_2 is $D(s)$ as defined in CR structure. However, due to the limitation that current performance prediction method could only support one reset element in the whole RCS, the parallel CR with two reset elements C_{par} and $\mathscr{R}$ could be difficult to predict its frequency behavior. But an approximation of C_{par} as a linear controller could be made for a certain situation when $\mathscr{R}$ is PCI. Regarding this specific situation, C_{par} could be approximated as $PI_{par}(L-1)$, and PI_{par} is the BLS of the corresponding PCI.

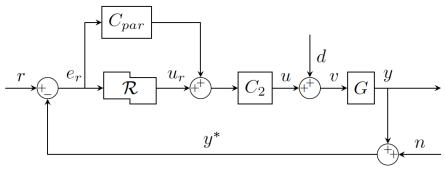

Figure 2.21: Block diagram of the RCS with parallel CR structure [3].

To sum up for the CR part, the basic principle of both CR and parallel CR is to apply a low pass filter (lag element $D(s)$) after the reset element to reduce undesired HOSIDFs. The difference between CR and parallel CR is the methods to eliminate the effect of adding a lag element. CR applies $L(s)$ as $D(s)^{-1}$ to cancel $D(s)$. Parallel CR adopts $C_{par}(s)$ as the $\mathscr{R}(L(s)-1)$ to eliminate the effect of $D(s)$, with the advantage of the less amplification of HOSIDFs at the input of the reset controller and less amplification of the undesired noise signal.

2.6 Past Implementations of Reset Controllers on AB383 Wire Bonder

The master thesis work in [3] applied a HOSIDF performance prediction model (closed-loop model A) for designing reset controllers. Sevel reset structures including CgLp, and PCI-PID with series and parallel CR were implemented. In terms of the CgLp structure, FORE was applied to construct the CgLp. Two CgLp elements ($CgLp_{10}$ and $CgLp_{15}$) were designed to form the CgLp-PID controller structure for AB383 wire bonder. The predicted frequency behavior is shown in Figure 2.22 based on a plant G_a occupying similar properties to the AB383 wire bonder. It is notable that CgLp introduces phase leads of 10 and 15 while exerting minimal impact on the gain of DF. From the perspective of closed-loop performance, CgLp was effective in reducing the magnitude of pseudo-sensitivity due to the introduction of phase lead, as clearly depicted in Figure 2.23.

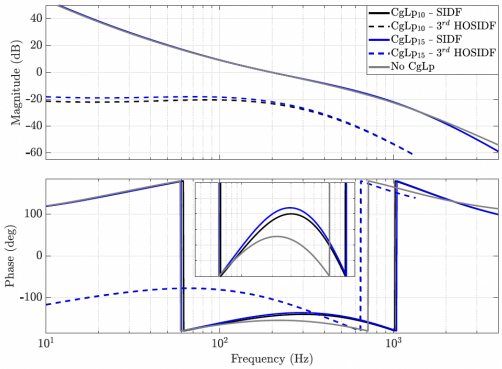

Figure 2.22: FRF of the DF and 3rd HOSIDF of the system with CgLp-PID controller, and FRF of the LTI controller without CgLp (all with the plant similar to AB383 wire bonder) [3].

Despite the evident robustness improvements concerning phase margin and modulus margin, the practical application of CgLp in industrial setups presents challenges, primarily due to the tendency of industrial stages to possess lower damping characteristics [3]. This scenario deviates from the experimental setups with highly damped resonance peaks often found in literature. Thus, it becomes imperative to thoroughly investigate the potential impact of high-frequency resonances on stability, especially when applied to industrial platforms such as the AB383 wire bonder. As elucidated by the stability study conducted in [3], less damped resonances at higher frequencies can be triggered by the HOSIDF generated by the nonlinear reset element CgLp. Consequently, to ensure system stability, the incorporation of a notch filter becomes necessary. This notch filter serves to attenuate the resonance peaks at high frequencies, and therein lies a challenge. The addition of the notch filter might result in a reduction of the phase margin greater than the phase lead provided by CgLp. In essence, the introduction of the required notch filter can counteract the overarching goal of expanding the phase margin, rendering CgLp less effective in its application to the AB383 wire bonder. In summary, the application of CgLp in the context of the AB383 wire bonder is complicated by the need for a notch filter to mitigate high-frequency resonance issues, which can undermine the intended enhancement of the phase margin.

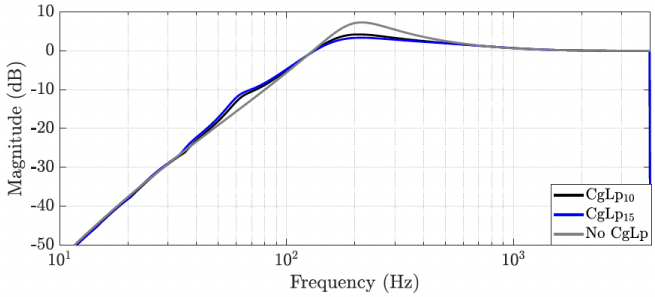

Figure 2.23: Pseudo-sensitivities computed through the approximate method of the closed-loop model for system with $CgLp_{10} - PID$, $CgLp_{15} - PID$, PID controller structure, with the plant similar to AB383 wire bonder [3].

The PCI reset element was also implemented into AB383 wire bonder to form the system with the PCI-PID controller. However, the trade-off discussed in Section 2.5, which involves balancing the trade-off between high DF magnitude with high HOSIDFs gain and a reduced phase margin, posed a challenge during the tuning of PCI [3]. To address this issue and reduce the magnitude of HOSIDFs while having a minimal impact on the gain of DF, a series CR element was applied into the PCI-PID control structure for AB383 wire bonder. This configuration, known as the CR-PCI-PID structure, was designed to diminish the HOSIDFs magnitude within the system governed by a PCI-PID controller. The open-loop system representation of the series CR-PCI-PID structure is illustrated in Figure 2.24. Under the condition of no noise, the CR-PCI-PID structure demonstrated improved system performance, as evidenced by the lower cumulative power spectral density (CPSD) of the error signal, as shown in Figure 2.26. However, in real-world scenarios where noise is present, the impact of noise cannot be ignored. In such cases, the presence of the part $L(s)$ of the CR element could amplify the undesired noise signal, leading to suboptimal steady-state performance, as depicted in Figure 2.27. Notably, the CPSD of the error signal in the system with the CR element was found to be higher than that without it.

Furthermore, the implementation of CR elements faces challenges beyond noise, including aliasing effects. In discrete implementations, to avoid aliasing, the power at frequencies above the Nyquist frequency should be minimal or nonexistent. This requirement is relatively satisfied by the PCI-PID control structure, where HOSIDFs exhibit lower magnitudes, as shown in Figure 2.12. However, in the CR-PCI-PID structure, the amplification of HOSIDFs at frequencies above ω_l in the $L(s)$ component from the CR element could lead to significant amplification of higher-

order HOSIDFs in the frequency range beyond the Nyquist frequency. The pseudo-sensitivity comparison shown in Figure 2.25 highlights the presence of multiple undesired peaks at higher frequency ranges in the system with the series CR element. These outcomes suggest that when considering practical aspects as discretization, aliasing and noise signals, the CR element could prove less effective in the context of the AB383 wire bonder.

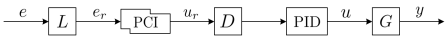

Figure 2.24: CR-PCI-PID structure (adjusted from [3]).

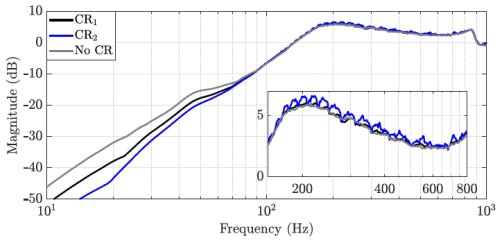

Figure 2.25: Pesudo-sensitivities of the system with and without series CR [3].

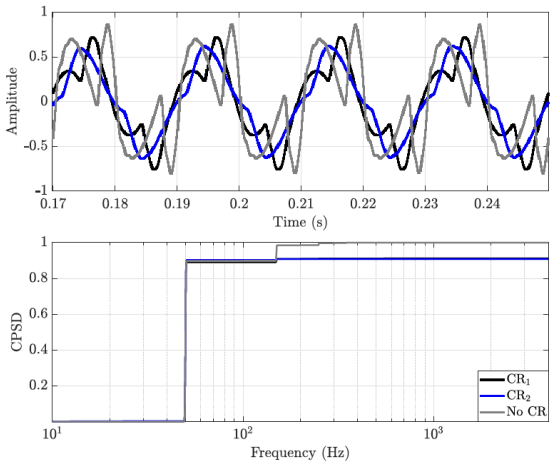

Figure 2.26: Normalized error signal of the closed-loop system without input noise resulting from the simulation and the CPSD of the error signal [3].

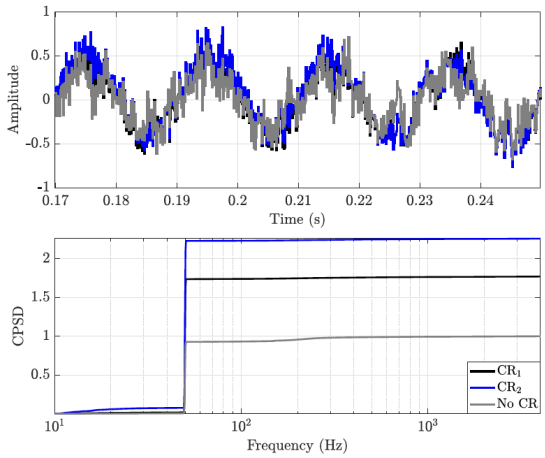

Figure 2.27: Normalized error signal of the closed-loop system with input noise resulting from the simulation and the CPSD of the error signal [3].

In order to effectively lower the magnitude of HOSIDFs when considering practical involving discrete systems with noise, the parallel CR was developed in [3] and implemented into AB383 wire bonder. Different from the CR element, the parallel CR does not amplify HOSIDFs and undesired noise signal at the input of the PCI, while also achieving the advantage of decreasing the magnitude of HOSIDFs within the RCS. In the parallel CR element, when $\mathscr{R}$ is PCI, $C_{par}(s)$ could be approximated as $PI_{par}(s)(D(s)-1)$, in which $PI_{par}(s) = 1 + \frac{w_{ipar}}{s}$ [3]. With the approximated $C_{par}(s)$, the parallel CR-PCI-PID is formed to control the wire bonder. An analysis of the error signal using experimental data, as illustrated in Figure 2.28, underscores the efficacy of the parallel CR structure. Notably, the CPSD originating from the system equipped with the parallel CR element demonstrates the lowest value, indicating a substantial reduction in error. This outcome signifies a significant improvement in the performance of the system.

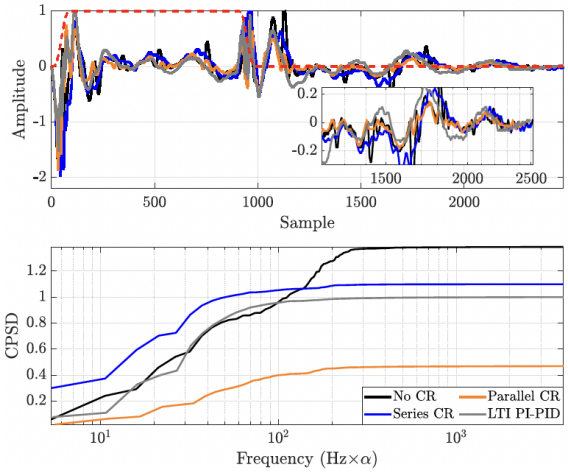

Figure 2.28: Normalized error signals and its CPSDs from experiments for a typical reference trajectory (the reference is scaled) [3].

Chapter 3

PCI-PID AND PGFbI

To ensure conciseness, this chapter presents the findings and contributions of this work in an individual paper format. The INTRODUCTION and PRELIMINARIES sections within this paper format encompass the necessary background and theories already discussed in Section 1.1, Section 1.2, Section 2.1, Section 2.2, and Section 2.3 of this report. Moreover, the automation tuning algorithms developed for the PCI-PID and PGFbI structures are made available on the official Matlab website, accessible through the reference [32].

Automated Reset Controller Design with a Novel Structure for Improved Performance of an Industrial Motion Stage

Abstract— **Linear time-invariant (LTI) controllers suffer from inherent limitations as the waterbed effect and Bode's gain-phase relationship. Reset control, a nonlinear strategy involving the reset of linear controllers, offers a potential solution to overcome these traditional LTI limitations. Based on the describing function analysis, the reset controller provides the advantage of less phase lag compared to its linear counterpart. In this study, we explore the application of the Proportional Clegg Integrator (PCI), a reset element, to replace the Proportional Integrator (PI) within the PID framework for a wire bonder, aiming to break LTI limitations and therefore improve the system's performance. However, due to the reset action of the PCI, it cannot provide a constant buffer force as the PI does to compensate for the machine's nonlinearity and external disturbances. This lack of compensation can lead to undesired limit-cycling behavior, preventing the system from achieving zero steady-state error. To address this issue, a PI is added after the PCI to form a PCI-PID framework for completely eliminating the limit cycles. To optimize the performance of the PCI within the PCI-PID framework, a tuning algorithm is proposed, leveraging the machine's frequency response function (FRF) data. Frequency-domain analytical tools, including open-loop Higher-Order Sinusoidal Input Describing Functions (HOSIDFs) and the pseudo-sensitivity function from approximate closed-loop HOSIDFs, are applied during the optimization process. However, the introduction of the PI for the PCI leads to a trade-off, causing a reduction in phase margin or a decrease in the nonlinear benefits gained from the PCI. To overcome this limitation, a novel integrator called the Generalized First Order Reset Element-based Integrator (GFbI) is introduced. The GFbI, as a single integrator, has the ability to internally incorporate a PI within its structure, allowing it to achieve the desired zero steady-state error without externally introducing an additional linear integrator. This unique characteristic allows the GFbI to attain zero steady-state error, without being confined by the limitations associated with introducing an additional PI. Furthermore, the GFbI can be automatically tuned based on a proposed constraint regarding the number of reset instants, permitting the use of machines' FRF data. Finally, with the novel GFbI structure and its tuning algorithm, the experimental data obtained from an industrial motion platform demonstrates a decrease (30.8%) in the root-mean-square of the settling error.**

I. Introduction

In the realm of precision motion control, linear time-invariant (LTI) controllers, such as Proportional-Integral-Derivative (PID) controllers, have gained widespread adoption and constitute over 90% of the controllers used in industry [1]. The popularity of linear controllers stems from their simplicity in design through loop-shaping methods, which establish a connection between open-loop and closed-loop performance. However, the traditional LTI control encounters challenges in meeting evolving demands for high accuracy, including exceptional tracking and disturbance suppression capabilities, while maintaining high speed. These challenges arise due to the inherent limitations of LTI controllers, such as the waterbed effect [2] and Bode's gain-phase relationship [3]. In essence, implementing an LTI controller necessitates a trade-off between bandwidth, robustness, and precision in terms of tracking and noise suppression abilities. Improving one aspect requires the compromise or degradation of at least one other performance criteria. This trade-off poses a limitation in achieving desired precision levels while maintaining other desirable characteristics.

To break the LTI limitations, nonlinear control strategies have been garnered great consideration in the literature, such as Split-Path Nonlinear (SPAN) filter [4], Hybrid Integrator-Gain System (HIGS) [5], and reset control [6]. The integrators of these nonlinear techniques, as analyzed by the Describing Function (DF), exhibit less phase lag compared to the traditional linear Proportional Integrator (PI). SPAN Integrator (SPANI) can achieve zero phase lag [7] [8], while its extension as Filtered Split-Path Nonlinear Integrator (F-SPANI) could achieve phase lead [8]. However, the further application of SPAN filter technique and its extensions in industry requires analytical frequency-domain performance prediction methods to facilitate loop-shaping. In contrast, HIGS and reset control could provide the accurate open-loop performance predictions in the frequency domain, based on Higher-Order Sinusoidal Input Describing Functions (HOSIDFs) [9] [10] [11] [12]. Among these two, reset control analytically offers closed-loop HOSIDFs [11] [13], enabling loop-shaping based design, which is non-existent for HIGS-based systems.

Reset control, as one of the nonlinear control strategies, was originally proposed by Clegg [6], and has shown the potential in overcoming LTI limitations. Based on the DF, the phase lag of a reset integrator called Clegg integrator (CI) can be reduced to 38° compared to the PI with 90° phase lag. Besides, recent studies have demonstrated the existence of frequency domain predictive performance [11] [13] and stability analysis methods for specific reset control structures [14] [15]. These methods offer an approach to design and analyze reset controllers with a similar means to that used for linear controllers, thus breaking the inherent LTI limitations while preserving the simplicity during the design of LTI systems. As for the reset control elements, the 'Constant in gain-Lead in phase' [16] is drawing some research attention, due to its ability to provide the phase lead advantage without necessitating an increase in the gain characteristic, as compared to a linear lead filter. Nevertheless, it should be noted that the design of the CgLp element comes with complexity in tuning, while simplicity is highly valued in practical industrial applications.

The Proportional Clegg Integrator (PCI), is another reset

structure, which will be focused in this work due to its relatively less tuning parameters compared to other reset elements. Additionally, PCI is mainly activated within the low-frequency range. Given that the present performance prediction methods for reset controllers are developed in continuous-time domain [11] [13], this characteristic aligns well with existing prediction methodologies, as at low frequencies, the Frequency Response Function (FRF) of a discrete system, representative of the real behavior of a practical system, closely aligns with its continuous counterpart. Through DF analysis, the PCI exhibits a higher open-loop gain at low frequencies compared to its linear counterpart, the PI, while maintaining the same phase lag around the bandwidth frequency. Consequently, replacing the PI with PCI in the PID structure improves low-frequency disturbance suppression and bandwidth without compromising phase margin. Previous literature has explored the utilization of PCI for this purpose [17]. In [17], the PCI is utilized to form a PI-PCID system, but the results show that the PI-PCID system did not outperform its linear counterparts, due to undesired higher-order harmonics introduced by the PCI. However, a recent research proposes a structure called Continuous Reset element, which effectively reduces the undesired HOSIDFs without altering the desired DF [15].

The goal of this paper is to firstly study the sequence of PCI-PID structure considering the practical effect of noise, and develop tuning algorithms for the PCI-PID. Based on the analysis of experimental results, PCI-PID systems are constrained by a trade-off between an increase in the nonlinear benefits gained from the PCI and an escalation of undesired limit-cycling behavior, which seriously limits the system's settling time. This trade-off is essentially attributed to that the PCI necessities an extra integrator PI to achieve zero steady-state error. To address this issue, we propose a novel nonlinear integrator, the Generalized First Order Reset Element-based Integrator (GFbI). The GFbI, a single integrator, internally incorporates a PI after the reset element, allowing it to achieve the desired zero steady-state error without externally introducing an additional linear integrator. We also develop an automated tuning algorithm for GFbI, aiming to maximize the open-loop bandwidth, while considering closed-loop performance related to the pseudo-sensitivity and the number of reset instants per period. The findings are finally validated through experiments, utilizing the industrial motion stage.

The next section (Section II) introduces the necessary background theory regarding reset control. In the subsequent section (Section III) the PCI-PID controller is investigated including its practically optimal sequence, and its tuning algorithm. Then, the effective aspects and drawbacks of optimized PCI-PID systems are discussed based on simulation and experimental results. Section IV presents the definition of the novel GFbI, along with its tuning guidelines based on a constraint regarding the number of reset instants. The experimental analysis is further performed to validate the feasibility and effectiveness of GFbI. Finally, conclusions and suggestions for future work are presented in Section V.

II. PRELIMINARIES

A. Motion control and its common LTI controllers

In order to control the motion of positioning systems, the control structure depicted in Fig. 1 is commonly utilized for industrial applications, in which P is assumed to be the LTI Single-Input Single-Output (SISO) plant, $r \in \mathbb{R}$ is the reference, $d \in \mathbb{R}$ is the disturbance, $n \in \mathbb{R}$ is the noise, and $y \in \mathbb{R}$ is the true output of the control system. The feedforward controller, denoted as C_{ff}, is responsible for accurately tracking a predefined reference trajectory. By employing an advanced feedforward controller approximately represented as P^{-1}, most of the plant dynamics represented by P can be taken into account. However, it is important to note that certain aspects of the plant dynamics, such as nonlinearities and high-frequency modes, may not be adequately modeled. These unmodeled plant dynamics can potentially result in undesired low-frequent base frame vibrations, which will be a significant focus of this paper. The feedback controller C_{fb} is therefore implemented to suppress base frame vibrations and attenuate the effects of disturbances.

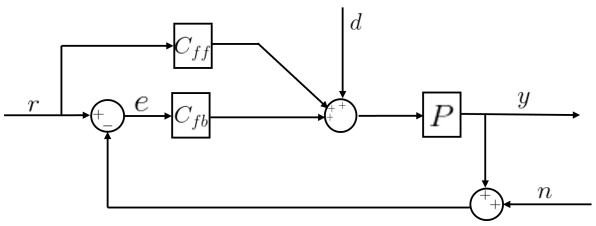

Fig. 1. Motion control system structure with LTI controllers.

One of the widely used feedback controllers in the industry is the LTI PID controller. The PID controller is typically represented by the following expression:

$$C_{PID} = \underbrace{k_P}_{\text{P}} \underbrace{\left(1 + \frac{\omega_{i-\text{PI}}}{s}\right)}_{\text{I (PI filter)}} \underbrace{\left(\frac{\frac{s}{\omega_d} + 1}{\frac{s}{\omega_t} + 1}\right)}_{\text{D (lead filter)}}, \tag{1}$$

where $s \in \mathbb{C}$ being the Laplace variable, $k_P \in \mathbb{R}$ being the proportional gain, $\omega_{i-\text{PI}} \in \mathbb{R}_{>0}$ being the corner-frequency of PI, and $\omega_d, \omega_t \in \mathbb{R}_{>0}$. Regarding discussing the function of PID in the frequency domain, the PI enhances the open-loop magnitude at the low frequencies, thereby suppressing low-frequency disturbances. Moreover, in terms of the time-domain performance, the incorporation of the PI enables a system that initially cannot achieve zero steady-state error to attain such error-free performance. On the other hand, the lead filter is employed to provide the phase lead majorly within the frequency range $[\omega_d, \omega_t]$, thereby ensuring the sufficient phase margin and robustness of the system. In terms of tuning a PID controller based on loop-shaping methods, the rules of thumb discussed in [18] [19] are commonly applied. Based on the practical experience with the wire bonder used during this work, the rules of thumb utilized in this work for PID tuning are provided as:

$$\omega_{i-\text{PI}} = \frac{1}{5}\omega_{bw},\ \omega_d = \frac{1}{3}\omega_{bw},\ \omega_t = 3\omega_{bw}, \tag{2}$$

with $\omega_{bw} \in \mathbb{R}_{>0}$ being the bandwidth defined as the open-loop cross-over frequency of the control system.

B. Definition of reset controllers

A SISO reset controller is defined in [11] as

$$R = \begin{cases} \dot{x}_r(t) = A_r x_r(t) + B_r e_r(t), & \text{if } e_r(t) \neq 0 \\ x_r(t^+) = A_\rho x_r(t), & \text{if } e_r(t) = 0 \\ u_r(t) = C_r x_r(t) + D_r e_r(t), \end{cases} \tag{3}$$

where $x_r(t) \in \mathbb{R}^{n_r \times 1}$ is the state vector of R, $e_r(t) \in \mathbb{R}$ is the input of R, and $u_r(t) \in \mathbb{R}$ is its output, with $t \in \mathbb{R}_{\geq 0}$ representing the time. $A_r \in \mathbb{R}^{n_r \times n_r}$, $B_r \in \mathbb{R}^{n_r \times 1}$, $C_r \in \mathbb{R}^{1 \times n_r}$ and $D_r \in \mathbb{R}$ with $n_r \in \mathbb{N}$ representing the number of states, stand for the linear state-space matrices which are named as the Base Linear System (BLS). The BLS of R is denoted as R_{BLS}, and its transfer function is obtained as

$$R_{BLS} = C_r(sI - A_r)^{-1}B_r + D_r. \tag{4}$$

In addition, the "zero-crossing" law $e_r(t) = 0$, as the traditional reset condition [20] defines the trigger of reset action. This particular law is employed in this work due to its feasibility of performance prediction in the frequency domain, rendering it the preferred approach. $A_\rho \in \mathbb{R}^{n_r \times n_r}$ is the reset matrix whose elements on diagonal determine the state values after being reset. A_ρ is usually a diagonal matrix, expressed as

$$A_\rho = \begin{bmatrix} \gamma & \\ & I_{n_R} \end{bmatrix}, \tag{5}$$

where γ = diag(γ_1, γ_2, γ_3,..., γ_r), $\gamma_i \in [-1, 1]$, and $\gamma_i = 1$ results in a corresponding linear controller [15]. Besides, the reset with $\gamma_i = 0$ is also called the traditional reset [13]. γ corresponds to reset states, while I_{n_R} is related to non-reset states with $n_R \in \mathbb{N}$ indicating the number of non-reset states. In summary, in (3), the first equation denotes the base-linear dynamics. The second equation demonstrates the reset action characterized by jump dynamics, which reveals the nonlinearity of the reset control [11]. The third equation symbolizes the output of the reset controller.

C. Reset control system architecture

The reset control system (RCS) architecture applied in this work is depicted in Fig. 2, in which C_1 and C_2 are the LTI SISO controllers, and $u \in \mathbb{R}$ is defined as the controller output.

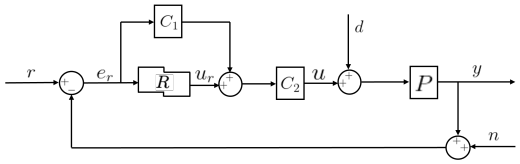

Fig. 2. General closed-loop reset control system.

D. Performance prediction and reset instants of RCS

In frequency domain analysis of LTI systems, the steady-state input-output relationship provides crucial information and serves as the foundation for computing FRFs. These FRFs play a fundamental role in employing loop shaping techniques for controller design. However, when dealing with a RCS subjected to a single harmonic input, the nonlinearity of the RCS results in the output of the reset controller being periodic, but not a single harmonic. By applying Fourier series analysis, the output of the RCS can be decomposed into the first-order harmonic with the same frequency as the input and higher-order harmonics with frequencies as multiples of the input harmonic.

The DF of a reset controller [21] is employed to predict its performance. It resembles the Bode plot of an LTI system, and is defined as the ratio between the Fourier transform of the first harmonic of u_r and the Fourier transform of the input of the reset controller, where the input is a sinusoidal of a certain frequency [22]. However, the DF method does not consider the higher-order harmonics of u_r, limiting its prediction accuracy. To achieve more accurate predictions, researchers have introduced the concept of HOSIDFs [9], which provide valuable information about the higher-order harmonic components present in the system's output. An analytical method, capable of predicting the open-loop HOSIDFs of the reset controller, was established in [11] and is given in Theorem 2.1.

Theorem 2.1: [10, Theorem 3.1] [12] Given $e_r(t)$ of a reset controller as a sinusoidal signal $e_r(t) = A_0\sin(\omega t)$ with $A_0 \in \mathbb{R}_{>0}$ and $\omega \in \mathbb{R}_{>0}$, two essential functions, which are the DF denoted as H_1, and n-th HOSIDF represented as H_n ($n \in \mathbb{N}$, and $n > 1$), are determined by

$$H_n(j\omega) = \begin{cases} C_r(j\omega I - A_r)^{-1}(I + j\Theta_D(w))B_r + D_r \\ \quad for\ n = 1 \\ C_r(jn\omega I - A_r)^{-1}(j\Theta_D(w))B_r \\ \quad for\ odd\ n > 1 \\ 0 \quad for\ even\ n > 1 \end{cases} \tag{6}$$

with $j = \sqrt{-1}$, and

$$\begin{aligned} &\Lambda(\omega) = \omega^2 I + A_r^2, \\ &\Delta(\omega) = I + e^{(\frac{\pi}{\omega}A_r)}, \\ &\Delta_r(\omega) = I + A_\rho e^{(\frac{\pi}{\omega}A_r)}, \\ &\Gamma_r(\omega) = \Delta_r^{-1}(\omega)A_\rho\Delta(\omega)\Lambda^{-1}(\omega), \\ &\Theta_D(\omega) = \tfrac{-2\omega^2}{\pi}\Delta(\omega)[\Gamma_r(\omega) - \Lambda^{-1}(\omega)]. \end{aligned}$$

It is noteworthy that the analysis of the 3rd HOSIDF in reset elements can provide a profound understanding of the behavior of all HOSIDFs [11]. This is because the magnitude of HOSIDFs ($n > 3$) often follow similar patterns and shapes as the 3rd HOSIDF. Focusing on the 3rd HOSIDF simplifies the analysis while still capturing the essential characteristics

of the nonlinearity properties of a reset element. Therefore, the visualization of HOSIDFs in this work will solely focus on the 3rd HOSIDF.

The HOSIDFs of a reset controller can be extended to the open-loop HOSIDFs of a RCS with LTI systems. In terms of the open-loop RCS depicted in Fig. 2, given the input as $e_r(t) = A_0\sin(\omega t)$, the resulting steady-state controller output can be calculated as an infinite sum of harmonics

$$\begin{aligned} u =& A_0|C_1(j\omega)||C_2(j\omega)|\sin(\omega t + \angle C_1(j\omega)) + \angle C_2(j\omega)) \\ & \sum_{n=1}^{\infty} A_0|H_n(j\omega)||C_2(jn\omega)|\sin(n\omega t + \\ & \angle H_n(j\omega) + \angle C_2(jn\omega)). \end{aligned} \tag{7}$$

Theorem 2.1 could accurately predict the open-loop performance of a reset controller. On the other hand, another method, allowing to utilize machines' FRF data, enables the implementation of loop-shaping methods for RCS by analytically relating the open- and closed-loop HOSIDFs. This method was established in [11] and is presented as Theorem 2.2.

Theorem 2.2: [10, Theorem 4.1]

$$S_n(\omega) = \begin{cases} S_1(j\omega), & for\ n = 1 \\ \frac{-L_n(j\omega)}{1+L_{BLS}(jn\omega)}(|S_1(j\omega)|e^{jn\angle S_1(j\omega)}), & for\ odd\ n > 1 \\ 0, & for\ even\ n > 1 \end{cases} \tag{8}$$

and

$$\begin{aligned} & S_1(j\omega) = \tfrac{1}{1+L_1(j\omega)}, \\ & L_n(j\omega) = (C_1(j\omega) + H_n(j\omega))C_2(jn\omega)P(jn\omega), \\ & L_{BLS}(j\omega) = (C_1(j\omega) + R_{BLS}(j\omega))C_2(j\omega)P(j\omega), \end{aligned}$$

when the following assumptions are satisfied:
1) The system is input-to-state convergent
2) Reset action occurs π/ω apart and there are two resets times per time period
3) Only the first harmonic of e_r results in reset actions.

The first assumption, regarding the input-to-state convergence, could be fulfilled for a RCS by satisfying H_β-condition [14] [23]. In terms of the second assumption, it has already been proven in [12, Corollary 1] that the reset action occurs with a period of π/ω. Furthermore, the validity of two resets per period can be assessed by calculating $e_r(t)$ based on the Theorem 2.2 and examining the number of zero crossings per period in $e_r(t)$, by taking into account a sufficient number of HOSIDFs. However, the third assumption does not always hold. It specifies that only the first harmonic of e_r results in resets, but the higher-order harmonics of $e_r(t)$ could also potentially influence reset actions and possibly cause multiple resets [11]. Besides, the third assumption only considers the high-order harmonics created by the first-order harmonic of e_r, while the higher-order harmonics generated by higher-order harmonics are not taken into account. However, it is worth noting that the first-order harmonic of $e_r(t)$ has larger magnitude compared to higher-order harmonics, and the reset element PCI studied in this work is only activated at the low-frequency range. Therefore despite the omissions in the third assumption leading to inaccuracies in predictions, Theorem 2.2 could still provide reasonably decent prediction accuracy, and shows much better accuracy than the DF-based sensitivity [11].

In order to provide a simple and comprehensive analysis of the closed-loop performance of RCS, multiple S_n derived from Theorem 2.2 are consolidated into a unified frequency function called the pseudo-sensitivity function. Given a RCS with the reference signal $r(t) = A_1 sin(\omega t)$ with $A_1 \in \mathbb{R}_{>0}$, the magnitude of pseudo-sensitivity of RCS is defined in [13]

$$|S_\infty(\omega)| = |\frac{\max(e_{ss}(\omega, t))}{A_1}|, \tag{9}$$

where

$$e_{ss}(t) = \sum_{n=1}^{\infty} A_1|S_n(j\omega)|\sin(n\omega t + \angle(S_n(j\omega))). \tag{10}$$

Additionally, to better describe the time-domain behavior of a RCS, the concept of reset instant was introduced in [13]. For a RCS with a single harmonic input at frequency ω, the reset instant is defined as the time when the steady-state error hits zero.

E. Reset elements

Two relevant reset elements are presented here, which are the Proportional Clegg Integrator (PCI) and the Generalized First Order Reset Element (GFORE).

1) PCI: As the first proposed reset element in [6] , CI could be implemented by resetting a linear integrator. The BLS and reset matrix of the CI are $A_r = 0$, $B_r = 1$, $C_r = 1$, $D_r = 0$ and $A_\rho = \gamma$. The advantage of CI is that its DF offers a lower phase lag of 38°, compared to the 90° phase lag of a linear PI. Similar to CI, PCI with the corner frequency $\omega_{i-\text{PCI}} \in \mathbb{R}_{>0}$ is derived when a PI is reset. The BLS and reset matrix of the PCI are derived as

$$A_r = 0, B_r = \omega_{i-\text{PCI}}, C_r = 1, D_r = 1, A_\rho = \gamma. \tag{11}$$

It is concluded that there are two tuning parameters of a PCI, which are $\omega_{i-\text{PCI}}$ and γ. In relation to the comparison between PCI and PI, when ensuring the same $\omega_{i-\text{PCI}}$ and $\omega_{i-\text{PI}}$, the PCI has the advantage of less phase lag and higher open-loop gain as shown in Fig. 3, indicating a larger phase margin and more suppression of low-frequency disturbances in control systems. Among different PCI elements with the same $\omega_{i-\text{PCI}}$, those with lower γ value exhibits more reset action and nonlinearity, resulting in greater reduction of phase lag and increase of open-loop gain, as depicted in Fig. 3. But as a part of the nonlinearity of PCI, undesired higher-order harmonics also increase as γ decreases, as illustrated by the 3rd HOSIDF in Fig. 3.

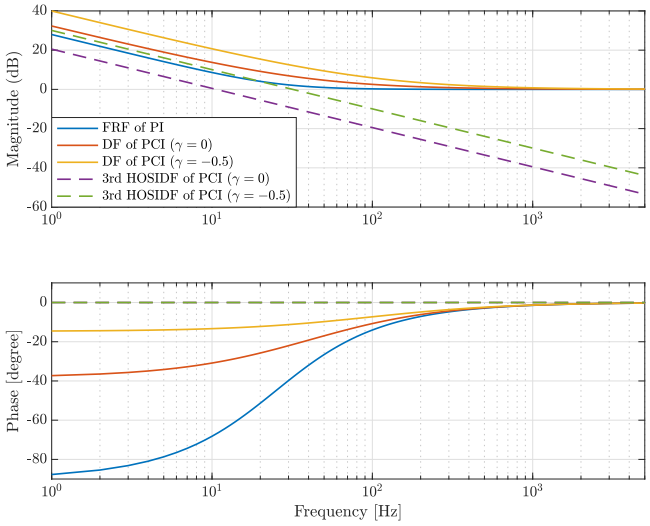

Fig. 3. FRF of PI, DF and 3rd HOSIDF of PCI (with $\gamma = 0$ and $\gamma = -0.5$), and all PI and PCI filters are with the same corner-frequency as 25Hz.

2) GFORE: First Order Reset Element (FORE) was firstly proposed in [24], and was extended as the Generalized FORE (GFORE) in [25]. GFORE is a resetting first-order low-pass filter with the corner-frequency ω_r. The BLS and reset matrix of GFORE are

$$A_r = -\omega_r, B_r = \omega_r, C_r = 1, D_r = 0, A_\rho = \gamma. \quad (12)$$

III. PCI-PID

Disturbance vibrations at the low frequency range, such as floor vibration and base frame vibration, is a noteworthy issue in the motion control field [17]. One particular example is the base frame vibration issue encountered in wire bonders manufactured by company ASMPT.

In order to suppress the base frame vibration mentioned in Section II-A and other low-frequent disturbances, the PI is commonly used, due to its large magnitude before the cut-off frequency in open-loop. In addition, when the PI design follows the rule of thumb in (2), it provides the added benefit of increased bandwidth due to the slight gain boost around the bandwidth frequency. However, despite the benefit of disturbance suppression and extended bandwidth, the 90° phase lag of PI can result in reduced robustness quantified by the decreased phase margin and modulus margin, as the traditional LTI limitations. In order to overcome this LTI limitation, the PI element of the PID controller expressed in (1) is replaced by the nonlinear reset element PCI to form the PCID feedback control structure. Nevertheless, resulted from the lack of a linear integrator in the PCID structure, zero steady-state error cannot be reached in the closed-loop system, leading to limit-cycling behavior [26]. Therefore, to address this issue, an extra linear integrator PI, is added to the PCID, forming the PCI-PID structure to eliminate the non-zero steady-state error. In the following parts, we will discuss the optimal sequence of the PCI-PID controller considering a practical perspective as noise, propose the tuning algorithm for the PCI-PID structure, and analyze the simulation and experimental validation results of optimized PCI-PID systems.

A. Sequence of the PCI-PID structure

It has been known that different sequences of linear controllers do not affect the performance of the system since they result in the same FRF. However, in the case of the RCS, the nonlinearity introduces variability in the PCI-PID system's performance when changing the relative position between the PCI and the LTI elements of the PID controller. In this part, the sequence of the PCI-PID structure to the performance of RCS, will be discussed when taking into account the practical effects.

1) Sequence between a PCI and a proportional controller: Based on the effect of the proportional controller, it is responsible for amplifying or attenuating the signals within the control loop. When it is placed before the PCI, it amplifies the input signals, and each harmonic of $e_r(t)$ are equally scaled due to the linearity of the BLS of R. Similarly, when the proportional controller is placed after the PCI, it still applies the same amplification or attenuation factor to the entire signal of $e_r(t)$, including both the DF and HOSIDF. Therefore, the scaling of the components remains unchanged, and the same scaled output signal is fed into the subsequent LTI elements of the control loop. The mathematical formulations about H_n and S_n, as expressed in Theorem 2.1 and Theorem 2.2, confirm this equal scaling property. As a result, regardless of whether the controller is positioned before or after the PCI element, the RCS exhibits the same performance, as the amplification or attenuation of the DF and HOSIDF components is consistent in both cases.

2) Sequence between a PCI and a lead (PD) filter: The work in [27] shows that locating the lead filter before the PCI (PD-PCI-PI structure) results in a more damped RCS with a mass plant, leading to the advantage of reduced settling time. To validate that the PD-PCI-PI structure shows the improved performance compared to the PCI-PID structure for a more complex plant, the LTI Simscape model of a wire bonder is utilized as the plant of the RCS. Theorem 2.1 and Theorem 2.2 are applied to calculate the pseudo-sensitivities of the wire bonder's model controlled by the PD-PCI-PI and PCI-PID, as shown in Fig. 4. The results demonstrate that the wire bonder controlled by PD-PCI-PI exhibits lower pseudo-sensitivity at low frequencies, indicating superior low-frequency disturbance suppression capability.

However, it is important to note that the Theorem 2.1 and Theorem 2.2 are based on the assumption that the entire RCS is SISO. However, in practical situations, the system is often subject to multiple inputs, such as noise signals introduced by encoder measurements. Placing the lead filter before the PCI could amplify the high-frequency noise signal which will be part of the $e_r(t)$ in the practical closed-loop system. If the system is subject to a relatively high noise level, the amplification of noise could change $e_r(t)$, and alter the reset instants and cause undesired excessive resets

[15], leading to a deterioration in the performance of the PD-PCI-PI system compared to the PCI-PID configuration. However, the work in [28] experimentally concluded that placing lead filter before the reset element could show better performance if the noise level is relatively low. Under this condition, the PD-PCI-PI system limited amplifies the noise signal, but exhibits less control input signal compared to the PCI-PID system. It is because that the resetting action leading to the output of the reset element jumping is fed into the lead filter, whose amplification of jump results in large control input signal within the RCS [28]. Less control input is preferred and could avoid the practical issues such as actuator saturation.

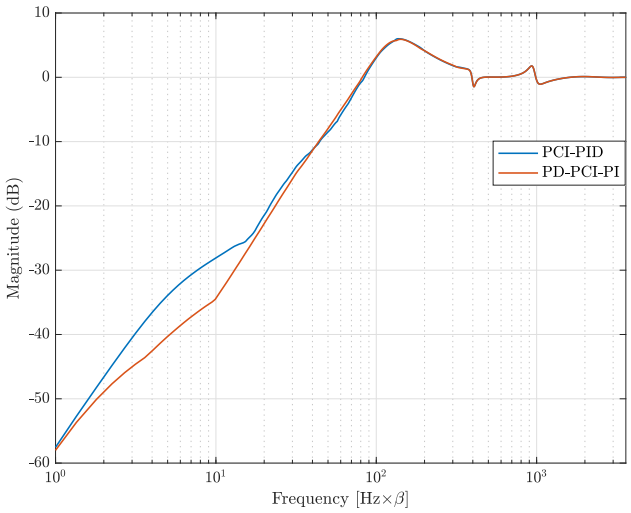

Fig. 4. S_∞ for the ASMPT's wire bonder model with PCI-PID and PD-PCI-PI controllers respectively, and for both controllers the PCI, PI, and lead filter have the same parameters (Due to confidentiality, the X-axis has been scaled by an arbitrary constant β.).

3) Sequence between a PCI and a PI: In the context of the relative position between PI and PCI, the primary role of PI is to ensure zero steady-state error in the control system. However, when dealing with plants which cannot attain zero steady-state error, placing PI before PCI cannot assist the whole system achieve such zero steady-state error because, when the error is integrated by both PI and PCI and reaches zero, PCI simultaneously resets the system's state according to the definition of R in Section II-B, and the achieved steady-state error is disrupted. Conversely, when the PI is placed after PCI, the reset action occurs first, allowing PI to continue integrating the error resulting from the reset action of the PCI. This allows the system to ultimately achieve the zero steady-state error, as the integration is maintained without interruption.

Taking into account the above discussion and recognizing the sensitivity of precision machines used in this study (ASMPT's wire bonders) to considerable noise, as well as the necessity of a PI integrator to attain zero steady-state error, the choice of placing reset element before PID controller i.e. PCI-PID is established. The selected PCI-PID control structure could be depicted through Fig. 2 as R is PCI controller, $C_1 = 0$, and C_2 is the LTI PID controller.

B. Tuning procedures of PCI-PID controller

After discussing the optimal sequence of PCI-PID controller, it could be then applied to replace the PID controller for breaking the traditional LTI limitations and therefore improving the system's performance. This part concentrates on the tuning algorithms of the PCI-PID structure. Since the BLS determines the most performance of its corresponding RCS [29], a well-designed RCS should have its BLS with the decent performance. Therefore, the preliminary step for designing a well-performed PCI-PID controller is to tune a decent PID controller as the origin of the PCI-PID design, which is called the original PID controller. A decent original PID controller could be tuned utilizing the rules of thumb outlined in (2). Building upon this well-tuned original PID controller, a PCI-PID controller could be subsequently tuned with two steps. Firstly, the original PID controller is modified by replacing the PI part with a tuned PCI element, resulting in the formation of a PCID controller. In the second step, an optimized PI filter is added to the PCID structure obtained in the first step, and the PCI-PID controller is finally formed.

Before discussing details of these two tuning steps, a relevant variable is supposed to be discussed at first. For a RCS with a single harmonic reference input at the frequency ω, the number of reset instants per period is denoted as $N_{ri}(\omega)$ when the RCS reaches its steady-state, and $N_{ri}(\omega) \in \mathbb{N}$. Additionally, since the reset instants occur with a period of $\frac{\pi}{\omega}$ and the period of RCS is $\frac{2\pi}{\omega}$ [13], there are even number of reset instants in each steady-state period of RCS. The minimum of $N_{ri}(\omega)$ is 2, as only the DF of the RCS results in resets. Therefore, $N_{ri}(\omega)$ is an even and positive integer.

Regarding the first step of tuning a PCI-PID controller, a PCID controller is tuned with the lead filter directly from the original PID controller, and therefore only parameters of the PCI element γ and $\omega_{i-\mathrm{PCI}}$ are adjusted during the first tuning procedure. However, it is difficult to determine the best PCI-PID controller between different γ values. It is because that although the PCI with lower γ benefits the advantage of less phase lag and larger open-loop gain, lower γ results in larger undesired higher-order harmonics, as explained in Section II-E.1. These increased higher-order harmonics could possibly activate the high-frequent modes of the machine. Besides, increased higher-order harmonics may affect the reset instants, and further lead to the undesired multiple resets. Therefore, determining the optimal PCI system between multiple γ values also relies on several practical aspects as the power of noise, distribution of machine's modes in the frequency domain. Thus, considering the complexity of determining the optimal PCI system with different γ, we list multiple γ values, and the parameter $\omega_{i-\mathrm{PCI}}$ is optimized for each single γ. This approach provides designers with sufficient freedom to tune a PCI-PID system based on the specific properties of each motion system and ensures the generality of the tuning procedure.

Based on the above reasoning, the tuning guidelines for PCI-PID controllers involve listing all the interested γ values.

In this work, γ values are listed as a range from -0.9 to 0.9, with increments of 0.1 (i.e. $[-0.9, -0.8, -0.7, ..., 0.9]$). For each γ value, the variable $\omega_{i-\text{PCI}}$ is tuned to form an optimized PCID during the first tuning step, denoted as $\bar{P}_1$, which is defined as:

$$\bar{P}_1 := \begin{cases} \max \ \ \omega_{bw}(\omega_{i-\text{PCI}}), \\ \text{s.t.} \ \ \max(S_\infty(\omega_{i-\text{PCI}}, \omega)) < \alpha \text{ dB}, \\ \qquad N_{ri}(\omega_{i-\text{PCI}}, \omega) = 2 \ \ \forall \omega \in [\omega_{bfv}, \frac{\omega_s}{2}], \\ \qquad 0 < \omega_{i-\text{PCI}} < \frac{\omega_s}{100}, \end{cases} \tag{13}$$

in which $\omega_{bw} \in \mathbb{R}_{>0}$ is the bandwidth of the PCID system defined as the open-loop cut-off frequency of the DF, i.e. $|H_1(\omega_{bw})| = 0$, and $\alpha \in \mathbb{R}_{>0}$. $\omega_s \in \mathbb{R}_{>0}$ is the sampling frequency of the system, and $\omega_{bfv} \in \mathbb{R}_{>0}$ is the frequency where the base frame vibration occurs.

The cost function ω_{bw} is defined with $\omega_{i-\text{PCI}}$ as the variable, where an increase in $\omega_{i-\text{PCI}}$ leads to improvements in both the system's bandwidth and the suppression level of base frame vibrations. During the first tuning step $\bar{P}_1$, the lead filter and proportional controller remain fixed from the original PID controller, and the increased bandwidth solely results from the increase in $\omega_{i-\text{PCI}}$ of the PCI element. Simultaneously, the increased $\omega_{i-\text{PCI}}$ offers an additional advantage by enhancing the suppression of low-frequency disturbance vibrations. Therefore, although the cost function is specifically defined as bandwidth in $\bar{P}_1$, it effectively optimizes both the system's bandwidth and the suppression of low-frequency disturbance vibrations simultaneously.

Regarding the constraints in $\bar{P}_1$, the first constraint associated with the pseudo-sensitivity can be interpreted that the "modulus margin" based on the S_∞ of the PCID system should be less than α to limit the magnification of the error by r. Typically, if adopting the rules of thumb of LTI systems for PCID systems, α should be 6 [18]. However, since a PI filter will be added to the optimized PCID controllers in the subsequent step, some margin needs to be reserved for the PI filter. Therefore α should be set lower than 6. In this work, α is customized to 5.8, in order to ensure the sufficient reset action for exceptional improvements in bandwidth and disturbance suppression.

The second constraint concerning $N_{ri}(\omega)$ is established because the performance prediction method applied in this work assumes that the RCS has two reset instants per period as discussed in Section II-D. It is anticipated that this assumption holds within our interested frequency range, which encompasses the frequency where base frame vibration mainly occurs. Additionally, regarding the first assumption concerning the input-to-state convergence of the applied performance prediction method (Theorem 2.2), this work does not take it into consideration within the optimization algorithm. This is due to the author's experimental observations that the PCI controllers designed based on $\bar{P}_1$ are consistently stable. Furthermore, in this study, it is assumed that the RCS is stable if its corresponding BLS is stable. The stability of the BLS is verified after the optimization phase but before the experimental stage.

The third constraint related to the sampling is to guarantee the precise capture of the PCI's behavior within the frequency range $[0, \omega_{i-\text{PCI}}]$ by the encoder. Following the rules of thumb in [18], the sampling system could capture both magnitude and frequency distribution information when the input frequency within the set $\{\omega | \omega < \frac{\omega_s}{10}, \omega \in \mathbb{R}_{>0}\}$. To ensure an enhanced measurement precision for capturing the nonlinear behavior of the PCI element, the condition $\omega_{i-\text{PCI}} < \frac{\omega_s}{100}$ is determined.

In the second step of the PCI-PID tuning, in order to achieve zero steady-state error, a PI filter is introduced after the PCID tuning to form a PCI-PID controller. This step optimizes the $\omega_{i-\text{PI}}$ of the added PI, while keeping the PCID controller fixed from the previous step. The added PI is tuned based on the optimization problem as follows:

$$\bar{P}_2 := \begin{cases} \max \ \ \omega_{bw}(\omega_{i-\text{PI}}), \\ \text{s.t.} \ \ max(S_\infty(\omega_{i-\text{PI}}, \omega)) < 6 \text{ dB}, \\ \qquad N_{ri}(\omega_{i-\text{PI}}, \omega) = 2 \ \ \forall \omega \in [\omega_{bfv}, \frac{\omega_s}{2}]. \end{cases} \tag{14}$$

In the tuning procedure $\bar{P}_2$, PI is designed for the PCI-PID controller, leading the maximum of S_∞ increasing from α to 6 dB. When α is set to 5.8, $\bar{P}_2$ provides a relatively weak PI action to guarantee the sufficient reset action in the system for improving the performance.

After the tuning procedures $\bar{P}_1$ and $\bar{P}_2$, a group of optimized PCI-PID systems are formed, each with a different γ value. The advantages of the $\bar{P}_1$ and $\bar{P}_2$ tuning guidelines for PCI-PID lie in their comprehensive nature. These procedures take into account both the open-loop and closed-loop information of the RCS, ensuring a well-rounded optimization process. Additionally, they could consider higher-order harmonics information when calculating the pseudo-sensitivity, resulting in a more accurate evaluation of the system's performance. Another advantage of these tuning procedures is their applicability in industry. $\bar{P}_1$ and $\bar{P}_2$ do not require a parametric model of the system; instead, FRF data of the machine can be utilized. This makes the tuning process practical and accessible for industrial usage, where obtaining an accurate parametric model of the machine may be challenging. Furthermore, these guidelines provide designers with ample freedom and alternatives in selecting the optimal PCI-PID controller. They can leverage their knowledge of the motion system's specific properties and draw from their testing experience to make informed decisions. Overall, the tuning procedures $\bar{P}_1$ and $\bar{P}_2$ offer a comprehensive, practical, and flexible approach to optimizing a PCI-PID controller based on the unique requirements and characteristics of the motion system.

C. Simulation model and simulation results analysis

To firstly verify the proposed tuning algorithms $\bar{P}_1$ and $\bar{P}_2$ for PCI-PID controllers, simulations based on ASMPT's AB383 wire bonder are performed.

1) Simulation model: Wire bonder is the machine to make interconnections between an integrated circuit or other semiconductor device and its packaging for semiconductor manufacturing, and one of them is ASMPT's AB383 wire bonder shown in Fig. 5(a). As a part of AB383 wire bonder, the isolated motion stage depicted in Fig. 5(b) allows for 3 Degree-of-Freedom (DoF) motion along X-, Y- and Z-axis. To model this motion stage, a lumped mass model is developed based on Simscape including a base frame, and individual X, Y and Z stages, as shown in Fig. 5(c). The base frame with substantial mass provides support and vibration isolation from external influences. The X,Y and Z motion stages are respectively responsible for the motion along X, Y and Z directions. Since each DOF of the motion stages is controlled by a separate actuator, the dynamics along the X-, Y- and Z-axis could be approximately treated as independent SISO systems. For this simulation verification study, the focus is on the X-stage, which is regarded as the P in Fig. 1 and Fig. 2.

Moreover, since the lumped mass model is derived through the linearization of its nonlinear motion equations at different positions, this model cannot fully capture the nonlinearity of the practical AB383 wire bonder's motion stage. Additionally, the lumped mass model considers the transport delay experienced by the practical AB383 wire bonder, and this delay could limit the system's bandwidth by introducing the increased phase lag. The FRF of the linear lumped mass model for the AB383 wire bonder is displayed in Fig. 6. Due to confidentiality, the frequency axis has been scaled by an constant β.

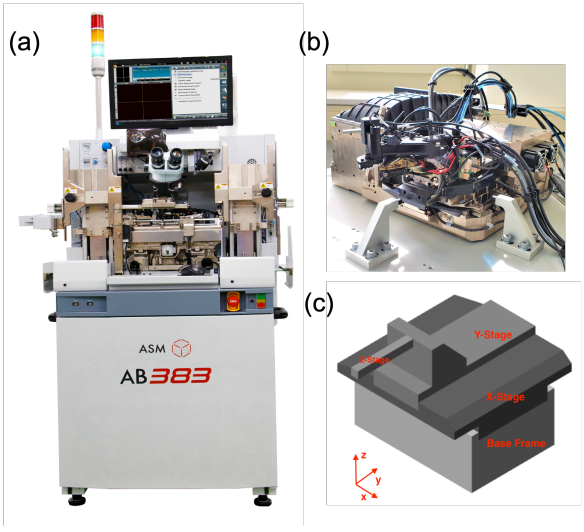

Fig. 5. (a) ASMPT AB383 wire bonder. (b) Isolated XYZ-motion platform of the AB383 wire bonder. (c) Model of the AB383 wire bonder's motion stage.

2) Simulation results analysis: Regarding the feedback controller designs for the lumped mass model of the AB383 wire bonder, an LTI PID controller was tuned at first by applying the rules of thumb in (2). This tuning process involved selecting a bandwidth ω_{bw} based on the plant's resonances and phase lag, as observed from its FRF in Fig. 6. The bandwidth were adjusted to achieve a high bandwidth and ensure a sensitivity peak of 6 dB. The tuned PID parameters are listed in Table I corresponding to $\gamma = 1$. After obtaining a satisfactory PID controller, PCI-PID controller can be further fine-tuned via the optimization procedures outlined in $\bar{P}_1$ and $\bar{P}_2$.

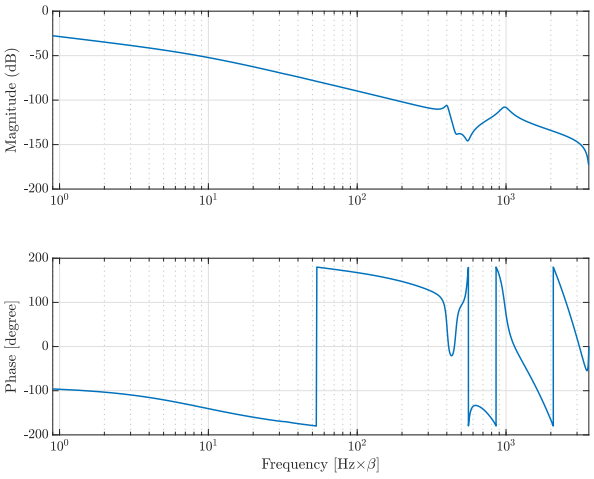

Fig. 6. FRF about the X-stage of AB383 wire bonder's Simscape model, with the transport delay.

For each γ from $[-0.9, -0.8, -0.7, ..., 0.9]$, the optimization algorithms $\bar{P}_1$ and $\bar{P}_2$ are performed. The parameters of the optimized PCI-PID controllers and their corresponding systems' performance parameters are shown in Table I. The performance parameters ω_{bw} and $S_\infty(\omega_{bfv})$ of the optimized PCI-PID systems with different γ are visualized in Fig. 7. It could be observed that as the decrease of γ, the optimized PCI-PID system exhibits an increased bandwidth and decreased S_∞ at the frequency ω_{bfv} representing the improved suppression ability of base frame disturbances.

In the interest of brevity, we have chosen to present results and analysis for only a few representative optimized PCI-PID systems from Table I. These selected systems include the RCS with the traditional reset as $\gamma = 0$, and the system with the theoretically largest optimized bandwidth and disturbance suppression level as $\gamma = -0.9$. The analysis of these representative systems will highlight the effectiveness of the proposed tuning algorithms ($\bar{P}_1$ and $\bar{P}_2$) and the advantages of utilizing the PCI-PID controller over traditional LTI controllers.

When ensuring the same maximum value between each S_∞ and the sensitivity function of the PID system denoted as S (within permissible tolerance in practice) as shown in Table I, Fig. 8 demonstrates that the optimized PCI-PID system offers the advantage of larger bandwidth and more disturbance suppression simultaneously. Besides, when comparing the DF between different PCI-PID systems, it becomes evident that the optimized PCI-PID system with a lower γ offers more improvements. However, when considering the higher-order harmonics of RCS in Fig 8, the optimized PCI-PID system with lower γ exhibits larger

TABLE I

OPTIMIZED PCI-PID SYSTEMS, THE ORIGINAL PID ($\gamma = 1$) SYSTEM AND THEIR FREQUENCY PERFORMANCE PARAMETERS, WITH THE PLANT AS THE LUMPED MASS MODEL OF THE AB383 WIRE BONDER.

PCI controller		PI controller	System performance parameters		
γ	$\omega_{i-\mathrm{PCI}}$ [Hz]	$\omega_{i-\mathrm{PI}}$ [Hz]	max(S_∞) (dB)	ω_{bw} [Hz]	$S_\infty(\omega_{bfv})$ (dB)
-0.9	1.503	2.700	5.995	107.100	-13.606
-0.8	2.939	2.475	5.991	105.750	-13.343
-0.7	4.242	2.700	6.000	103.950	-13.029
-0.6	5.477	2.700	5.995	102.600	-12.746
-0.5	6.679	2.700	5.997	101.250	-12.485
-0.4	7.815	2.700	5.995	99.900	-12.226
-0.3	8.884	2.813	5.997	99.000	-11.966
-0.2	9.885	2.925	5.998	97.650	-11.710
-0.1	10.955	2.813	5.996	96.750	-11.489
0	11.890	2.475	5.995	95.400	-11.265
0.1	12.691	2.138	5.994	94.500	-11.036
0.2	13.092	2.25	6.000	93.150	-10.754
0.3	13.560	2.138	5.999	91.180	-10.505
0.4	13.894	2.138	5.999	90.450	-10.251
0.5	14.228	2.025	5.995	89.550	-10.014
0.6	14.495	2.025	5.999	88.650	-9.776
0.7	14.695	2.025	5.999	87.750	-9.537
0.8	14.895	1.913	5.991	86.850	-9.299
0.9	15.096	1.913	5.998	85.950	-9.057
1	0	17.100	5.997	85.500	-9.074

Note: Gain controllers and lead filters are consistent across controller groups, where $k_P = 7344.1$, $\omega_d = 28.5$ Hz and $\omega_t = 256.5$ Hz. All frequencies in this table are scaled by β to maintain confidentiality.

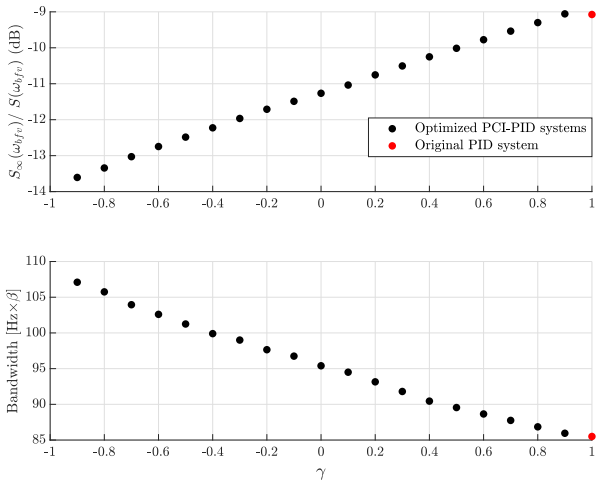

Fig. 7. Bandwidth and $S_\infty(\omega_{bfv})$ of optimized PCI-PID systems with different γ and $S(\omega_{bfv})$ of the original PID system ($\gamma = 1$), with the plant as the lumped mass model of the AB383 wire bonder's X-motion stage.

undesired HOSIDFs, potentially leading to more excessive resets and a deterioration in performance for the systems whose high-frequency modes have large magnitude.

In terms of the closed-loop performance of the PCI-PID systems, based on the analytical equations in Theorem 2.2 and (10), Fig. 10 illustrates the S_∞ and S_1 of the PCI-PID systems, as well as the S of the PID system. Besides, the simulation-based S_∞ is also provided in Fig. 10, to validate the accuracy of theory-based prediction (based on Theorem 2.2 and (10)), and to provide the information where Theorem 2.2 is not valid due to that $N_{ri}(\omega) = 2$ is not satisfied. As the reliable reference of S_∞, the simulation-based prediction is derived by only activating the reference input as a single harmonic wave within the control scheme in Fig. 2, then conducting the time-domain simulations, and finally applying

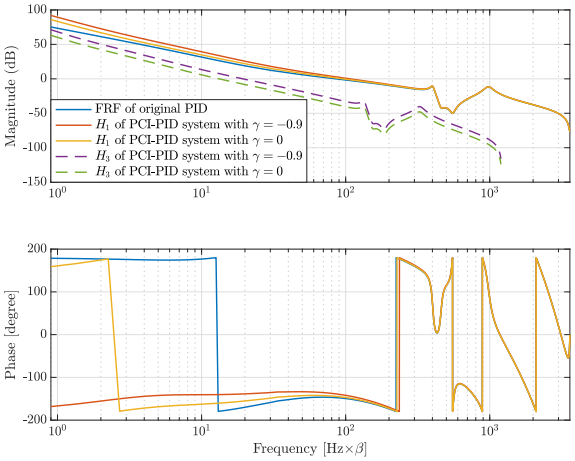

Fig. 8. Magnitude and phase characteristics of the DF and 3rd HOSIDF of the open-loop optimized PCI-PID system with $\gamma = 0$ and $\gamma = -0.9$, and the open-loop FRF of the original PID system, with the plant as the lumped mass model of the AB383 wire bonder's X-motion stage.

simulation data to calculate the S_∞ according to its definition in (9). The comparison between the simulation-based S_∞ and theory-based S_∞, indicates that the theory-based prediction is accurate at the frequency range where the assumption $N_{ri}(\omega) = 2$ holds. However, in the frequency range with multiple resets ($N_{ri} > 2$), the theory-based prediction shows the evident deviation compared to the trustworthy simulation-based prediction. Hence, it is crucial to ensure that the assumption $N_{ri} = 2$ is met for the theory-based prediction to be reliable and accurate.

Regarding the comparison between the optimized PCI-PID systems and the original PID system, the frequency domain could be divided into four regions based on the intersection points at the frequencies (ω_{cro1}, ω_{cro2}, ω_{cro3}) between the S_∞ of the RCS and the S of the original PID system. These four frequency ranges indicate the improved or deteriorated performance of the PCI-PID systems compared to the original PID system. Fig. 10 could show these deterioration and improvements, but in order to clearly show the division of four frequency ranges, Fig. 9 displays the legible comparison between the optimized PCI-PID system with $\gamma = -0.9$ and the original PID system.

The first frequency region $[0, \omega_{cro1}]$ in Fig. 9 shows that the performance of the optimized PCI-PID system is worse than the original PID system. This is essentially due to the occurrence of the undesired multiple resets, indicating the relatively large HOSIDFs compared to the desired DF. Furthermore, large HOSIDFs cause the large deviation of S_∞ to its corresponding S_1 as depicted in Fig. 10, finally resulting in the worse performance of the optimized PCI-PID systems. Additionally, due to the multiple resets at the first frequency region, the theory-based performance prediction is less accurate as the assumption $N_{ri} = 2$ does not hold. However, through the simulation-based S_∞, the deterioration performance of the PCI-PID system with multiple resets can be verified. In the second frequency region $[\omega_{cro1}, \omega_{cro2}]$, the

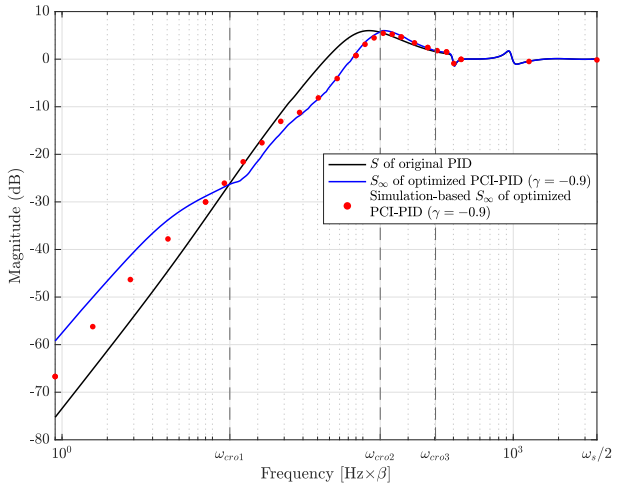

Fig. 9. Comparison between S_∞ of the optimized PCI-PID ($\gamma = -0.9$) and the S of the original PID system, displaying the four divisions of the whole frequency ranges, with the plant as the lumped mass model of the AB383 wire bonder X-motion stage.

performance of the PCI-PID system is better than the PID system, since the S_∞ of the optimized PCI-PID system is lower than the S of the PID system. This is because at this frequency region, multiple resets gradually decreases, and therefore the desired DF with the advantage of larger open-loop gain is dominant. As a result, the benefit of PCI in terms of the low-frequency disturbance suppression is observed. The third frequency region $[\omega_{cro2}, \omega_{cro3}]$ shows deteriorated performance for the PCI-PID system due to the large value of S. However, this deterioration is not caused by the undesired nonlinearity of the PCI but is the determined result of the increase in bandwidth. The increase in bandwidth necessarily causes the right shift of the sensitivity peak, resulting in S_∞ being larger than the S. Since PCI is usually not activated at such high-frequency ranges, this deterioration is inevitable as the bandwidth increases. Regarding the fourth frequency range $[\omega_{cro3}, \frac{\omega_s}{2}]$, both the optimized PCI-PID system and the original PID system show equivalent performance because S and S_∞ overlap each other. This is due to that neither the PI from the original PID system nor the PCI from the optimized PCI-PID system are activated at such high-frequency ranges.

In terms of comparing the closed-loop performance between the different optimized PCI-PID controllers, the PCI-PID system with lower γ exhibits the characteristic of higher open-loop gain for both DF and HOSIDFs. Due to larger open-loop DF, the PCI-PID with lower γ benefits the advantage of lower S_1. Therefore, when $N_{ri}(\omega) = 2$, indicating the DF is dominant compared to HOSIDFs, the PCI-PID system with $\gamma = -0.9$ could show an improvement, as it results in lower S_∞. However, lower γ also indicates higher open-loop HOSIDFs, which bring the disadvantage of more influence on reset instants and lead to multiple resets. Therefore, due to larger HOSIDFs, the optimized PCI-PID system with lower γ such as $\gamma = -0.9$, also suffers from the drawback of a wider frequency range where multiple resets occurs as depicted in Fig. 10.

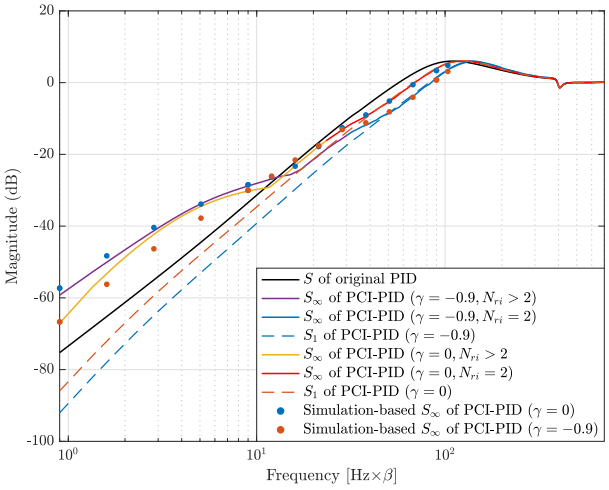

Fig. 10. S_∞ and S_1 of the optimized PCI-PID systems with $\gamma = 0$ and $\gamma = -0.9$, S of the original PID system, and the simulation-based S_∞ expressed as dash points for verification, with the plant as the X-stage of the lumped mass model of AB383 wire bonder.

After the performance analysis in the frequency-domain, the simulations results in time-domain are analyzed to validate the effectiveness of the proposed tuning algorithms $\bar{P}_1$ and $\bar{P}_2$. The resulting error signals and their Power Spectrum Density (PSD) applied in the settling phase, for a typical reference trajectory, are portrayed in Fig. 11. The reference trajectory consists of three distinct phases: initially transitioning from 0 to its maximum value, then maintaining this maximum value, and ultimately transitioning back from the maximum value to 0. As the interested region of the error signal, the settling phase of the error signal is defined as the period between sample $k_{set} \in \mathbb{N}$, the sample at which the reference signal firstly reaches it maximum and the sample at which the reference signal lastly remaining its maximum, as demonstrated in Fig. 11.

From the time-domain error signal in Fig. 11, we could find that the error within the settling phase is reduced with the optimized PCI-PID controllers compared to the one with the original PID controller. Furthermore, the spectrum analysis of the error within the settling phase in Fig. 11 reveals that the base frame vibration is significantly suppressed with the optimized PCI-PID controllers. Notably, the PCI-PID system with lower γ shows more suppression, which is consistent with the predictions made in the closed-loop sensitivity analysis. These results demonstrate the effectiveness of the proposed optimization algorithms $\bar{P}_1$ and $\bar{P}_2$ for PCI-PID controllers in reducing settling errors and suppressing base frame vibrations, leading to the improved tracking and disturbance rejection performance.

D. Experimental setup and experimental results analysis

After successfully applying tuning procedures $\bar{P}_1$ and $\bar{P}_2$ in simulations with the lumped mass model of the AB383

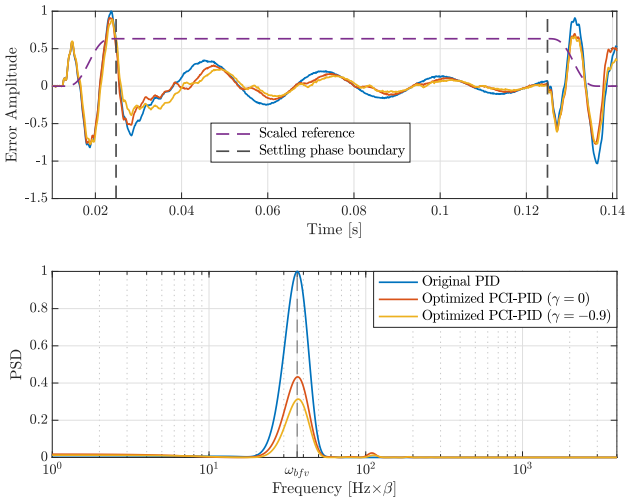

Fig. 11. Error signals of the settling phase and their corresponding PSDs obtained from simulations for a typical reference trajectory (the reference is scaled).

wire bonder, experimental validation is performed with ASMPT's Yθ table machine. This real-world validation will assess the effectiveness of the optimized PCI-PID controller under practical operating conditions, providing valuable insights into its performance enhancements in tracking ability, disturbance rejection, and overall precision in motion control.

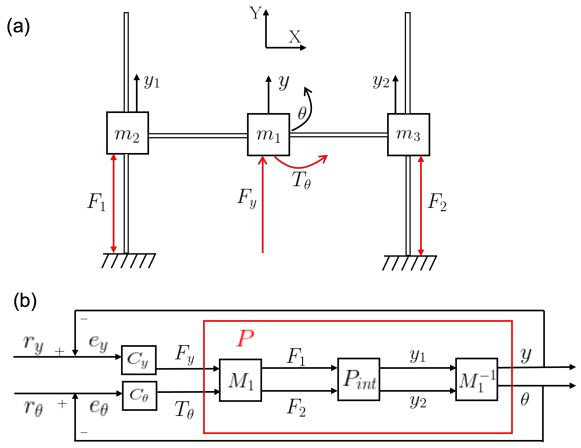

Fig. 12. (a) Schematic diagram for the dynamics of ASMPT's Yθ table. (b) Control scheme of ASMPT's Yθ table.

1) Experimental setup: The Yθ table's motion platform, is composed by a central moving mass m_1 and two actuators denoted as m_2 and m_3, as depicted in Fig. 12(a) respectively. The moving mass m_1 can achieve two DoFs: translation along the Y-axis with the displacement y and rotation in the XY-plane with angle θ. The applied force F_y and torque T_θ are responsible for controlling the translation and rotation respectively. The actuators, which are rigidly connected with the moving mass by a rod, could transitionally move along the Y-axis. The two actuators are utilized to control the motion of m_1 by adjusting their positions on the guideways. In other words, when m_2 and m_3 move with the same displacement along Y-axis, the stage m_1 is under translation motion, while m_2 and m_3 move with the different displacements, m_1 performs the rotation. And the displacement of m_2 and m_3 on the Y-axis are measured by encoders as y_1 and y_2 separately. In industry, the decoupled and collocated equation of the interested moving mass is usually preferred. Therefore, since the controlled object is m_1, the forces exerted on the actuators m_2 and m_3 are supposed to be transformed to the forces subject to the central moving mass m_1 (i.e. the transformation from F_1 and F_2 to F_y and T_θ). Similarly, it is also necessary for the transformation from y_1 and y_2 to y and θ. In order to achieve these transformations, the matrix M_1 is introduced as shown in Fig. 12(b). If the dynamics from F_1 and F_2 to y_1 and y_2 is regarded as the plant P_{int} in Fig. 12(b), the dynamics of the central moving mass m_1 from F_y and T_θ to y and θ is therefore derived as $M_1 P_{int} M_1^{-1}$. The dynamics $M_1 P_{int} M_1^{-1}$ could be successfully decoupled by the M_1 matrix, the y and θ are regarded as being separately controlled by the force F_y and T_θ. Thus, the dynamics from F_y to y could be approximated as a SISO system. In this work, only translation dynamics of the central mass is studied, and the dynamics of F_y to y is regarded as the plant P in Fig. 2. The decoupling matrices are provided by ASMPT and only the plant P is studied, which is assumed to be well-decoupled in this work. The identified FRF of the SISO system from F_y to y suffering the transport delay is shown in Fig. 13. To ensure confidentiality, the frequency axis has been adjusted by an arbitrary constant η, and magnitude and phase information has been excluded. Same as the lumped mass model of AB383 wire bonder, the practical Yθ table is also perplexed by the base frame vibration.

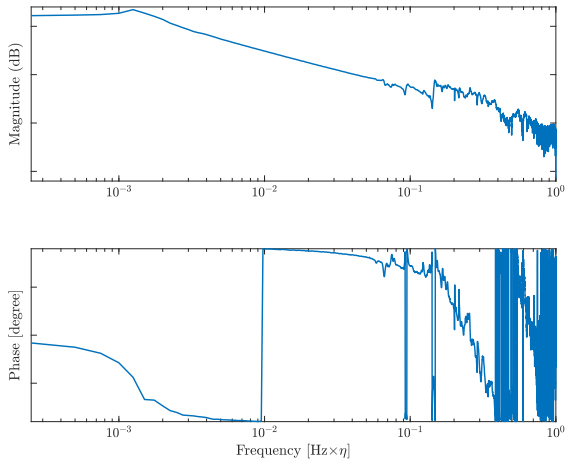

Fig. 13. Identified FRF from the Yθ table in translation motion, from the force on the moving mass F_y to its displacement y.

2) Experimental result analysis: In terms of tuning a decent LTI PID controller, the rules of thumb in (2) are also applied to the PID design for the Yθ table, to achieve the high bandwidth with modulus margin at 6dB, and the parameters

TABLE II

OPTIMIZED PCI-PID SYSTEMS, THE ORIGINAL PID ($\gamma = 1$) SYSTEM AND THEIR FREQUENCY PERFORMANCE PARAMETERS, WITH THE PLANT AS THE TRANSLATION MOTION OF Yθ TABLE.

PCI controller		PI controller	System performance parameters		
γ	$\omega_{i-\text{PCI}}$ [Hz]	$\omega_{i-\text{PI}}$ [Hz]	max(S_∞) (dB)	ω_{bw} [Hz]	$S_\infty(\omega_{bfv})$ (dB)
-0.9	4.824	8.438	5.994	312.500	-12.335
-0.8	9.370	8.438	5.996	307.500	-12.020
-0.7	13.823	6.875	5.999	305.000	-11.761
-0.6	17.441	6.875	5.996	297.500	-11.383
-0.5	20.781	6.875	5.991	290.000	-11.030
-0.4	23.750	7.500	5.993	285.000	-10.675
-0.3	26.904	7.188	5.997	280.000	-10.383
-0.2	29.688	6.875	5.993	277.500	-10.078
-0.1	32.100	5.938	5.994	272.500	-9.764
0	33.770	5.938	5.999	270.000	-9.390
0.1	35.254	5.938	5.997	267.500	-9.026
0.2	36.367	6.250	5.992	262.500	-8.657
0.3	37.852	5.781	5.995	257.500	-8.338
0.4	38.965	5.156	5.995	252.500	-8.015
0.5	39.336	5.313	5.995	250.000	-7.662
0.6	39.707	5.469	5.994	247.500	-7.327
0.7	40.264	5.469	5.995	245.000	-7.018
0.8	40.820	5.469	5.995	242.500	-6.722
0.9	41.191	5.625	5.994	240.000	-6.430
1	0	47.222	6.004	237.500	-5.866

Note: Gain controllers and lead filters are consistent across controller groups, where $k_P = 3518300$, $\omega_d = 79.167$ Hz and $\omega_t = 712.5$ Hz. Frequency parameters are scaled by $\eta{*}10^4$ for confidentiality and readability.

of such PID controller are shown in Table II with $\gamma = 1$. In addition, ASMPT has developed a notch filter to suppress the plant mode at the high-frequency range, with this introduced notch filter being considered as an integral component of the overall plant system. With the decent linear PID controller for translation dynamics of Yθ table, the PI is firstly replaced by PCI and a relatively weak PI is added afterwards based on the optimization algorithm in $\bar{P}_1$ and $\bar{P}_2$, to finally form the optimized PCI-PID systems.

The tuning and analysis of the optimized PCI-PID systems for experimental setup followed a comparable approach in the section of simulation validation, where the controllers were optimized through $\bar{P}_1$ and $\bar{P}_2$ for different values of γ in the range [0.9, 0.8, 0.7, ..., 0.9]. The parameters of these optimized PCI-PID controllers are provided in Table II in the Appendix. The performance parameters, ω_{bw} and $S_\infty(\omega_{bfv})$, for the optimized PCI-PID systems with varying γ values are illustrated in Fig. 22 in the Appendix. Same as the trends observed in the simulation validation from Fig. 7, a decrease in γ results in optimized PCI-PID systems with increased bandwidth and decreased S_∞ at the frequency ω_{bfv}. Conducting a similar comparison strategy in the simulation result analysis, the detailed analysis is performed including the optimized PCI-PID systems with the traditional reset as $\gamma = 0$, and with the theoretically largest tuned bandwidth and disturbance suppression level as $\gamma = -0.9$.

In the frequency-domain analysis, due to the similarity of the results between PCI-PID systems with simulation model and experimental setup, the frequency-domain analysis in this section will be concise, and more details in explanation could be derived from Section III-C.2. Compared to the original PID system in open-loop, the DF of optimized the PCI-PID systems depicted in Fig. 23 exhibits the improvement in bandwidth and low-frequent disturbances suppression. Regarding the comparison between different optimized PCI-PID systems, a trade-off is evident. An increase in bandwidth and enhancement of disturbances suppression is accompanied by larger undesired higher-order harmonics, which could lead to excessive resets and may activate the high-frequency modes of the plant. Regarding the closed-loop comparison between optimized PCI-PID systems and the original PID system in Fig. 24, the entire frequency range could also be divided into four parts, indicating where the PCI-PID systems show the improved or deteriorated system's performance compared to the PID system, as discussed in Section III-C.2. The comparison between different optimized PCI-PID systems in the closed-loop shows the same trade-off as observed in the simulation. Lower γ is associated with the advantage of lower S_∞ within the mid-frequency range where $N_{ri}(\omega) = 2$ holds, but it is also accompanied with the disadvantage of a wider frequency range with multiple resets, as depicted in Fig. 24.

During the discussion of time-domain performance of the optimized PCI-PID systems and the original PID system, the Root-Mean-Square (RMS) of the error signal at the settling phase, is defined as

$$e_{RMS} = \sqrt{\frac{1}{1 + k_n - k_{set}} \left(\sum_{k=k_{set}}^{k_n} e_k^2 \right)}, \tag{15}$$

where $k_n \in \mathbb{N}$ is the last sample in the settling phase. The resulting normalized e_{RMS} is shown in Table V. Notably, the proper tuning algorithms for the PCI-PID controller led to a reduction of approximately 20% in e_{RMS} for both PCI-PID systems compared to the original PID system.

After globally analyzing the experimental error signals from the e_{RMS} perspective, the detailed analysis discussing the local performance of the error in settling phase is supposed to be conducted. In Fig. 14, compared to the original PID system, the PCI-PID systems present a noticeable reduction in undershoot (at the time around $1.6s$). This reduction significantly demonstrates the benefit of the PCI-PID systems tuned by the optimization algorithm $\bar{P}_1$ and $\bar{P}_2$. Nevertheless, it is important to note that the subsequent limit cycles of the PCI-PID systems (starting around $1.62s$ for $\gamma = 0$, and around $1.6s$ for $\gamma = -0.9$) strongly worsen the time-domain performance, since these cycles lead to the increased settling time of the system.

The cause of the limit cycling behavior can be attributed to the reset action of the PCI. A PI filter could gradually integrate the error, and the force provided by PI as its output increases over time to counteract disturbances and the nonlinearity of the plant. This process continues until the error reaches zero, and the plant is subject to a constant force from PI, which could compensate for the disturbances in the system and the plant's nonlinearity. On the other hand, within a reset integrator PCI, being similar to the PI at first, the error is gradually integrated, leading to an increase in the force provided by PCI. However, when the error reaches zero, the force provided by the PCI is reset, resulting in the absence of a constant counteracting force to compensate for the nonlinearity of the plant. As a consequence, the nonlinearity of the machine is not fully eliminated, and the error persists, prompting PCI to continue its integration process and the

subsequent reset action. This repeated iteration leads to the occurrence of limit cycles in the optimized PCI-PID systems, as depicted in Fig. 14. While a PI filter is employed to assist the PCI in counteracting the nonlinearity of the plant and achieving zero steady-state error, the relatively weak PI used in this work necessitates long time to fully eliminate the limit cycles. It is worth mentioning that these limit cycles are not observed in simulations due to the utilization of a linearized model, while the limit cycles in this work is mainly contributed by the nonlinearity of the plant.

Cumulative Power Spectral Density (CPSD) analysis in Fig. 14 revealed that the limit cycles of the PCI-PID systems could also deteriorate the suppression of base frame vibration, leading to increased overall error powers compared to the original PID system. In conclusion, experimental results demonstrate that considering the practical effect of the plant nonlinearity and the caused limit cycling behavior, the time-domain performance (settling time) and the suppression of base frame vibration of the optimized PCI-PID systems are even deteriorated compared to the original PID system.

To address the evident limit cycles, one potential solution involves strengthening the linear integrator relative to the PCI strength to provide a constant counteracting force and quickly eliminate the limit cycles. However, this solution involves a trade-off, as stronger PI action comes at the cost of reduced improvement in bandwidth and suppression of low-frequency disturbances. Another alternative is to apply a different reset integrator, such as the PI+CI structure proposed in [30], where the gain of PI and PCI are separately designed. Nonetheless, this approach also introduces a trade-off, as increased PI action results in greater phase lag of DF, leading to less nonlinearity advantage in phase lag. Given these trade-offs in the current solutions, a novel reset integrator is proposed in the next section to overcome these limitations.

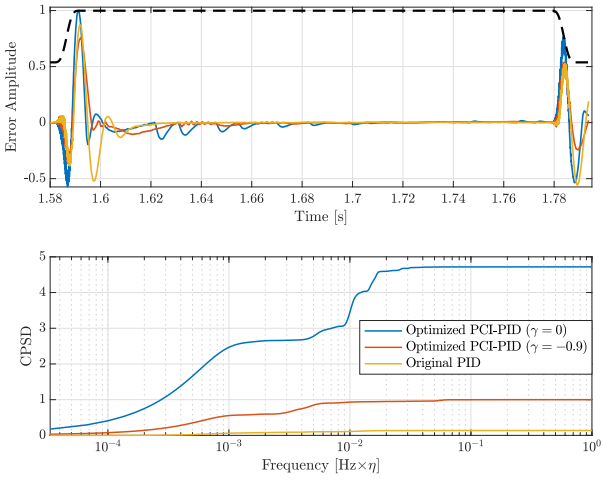

Fig. 14. Normalized error signals of the settling phase and their corresponding CPSDs obtained from experiments conducted on the Yθ table with a typical reference trajectory (the reference is scaled), and CPSD is based on processing the error signal at the settling phase with adding Hanning windows.

IV. Generalized FORE-based Integrator (GFbI)

A. Definition of GFbI

The application of optimized PCI-PID controllers into the Yθ table has led to reductions in undershoot and the e_{RMS} of the settling phase error, as evident from the analysis of experimental measurement data. However, replacing the PI with the PCI could result in the deterioration of the system's zero steady-state error performance, such as the undesired limit cycling behavior.

Theoretically and mathematically speaking, based on the internal model principle [31] for the LTI SISO system, the feedback controller containing the internal model of the reference signal $r(t)$ could result in the achievement of asymptotic tracking (i.e. $\lim_{t\to\infty} e(t) = 0$) for LTI system. To be specific, when assuming C_{ff} depicted in Fig. 1 is zero and representing the transfer function of $P(s)$ and $C_{fb}(s)$ as $P(s) = \frac{N_p(s)}{D_p(s)}$ and $C_{fb}(s) = \frac{N_{fb}(s)}{D_{fb}(s)}$, along with expressing the Laplace transform of $r(t)$ as $\frac{N_r(s)}{D_r(s)}$, asymptotic tracking necessitates that the existence of a polynomial $M(s)$, such that $D_p(s)D_{fb}(s) = M(s)D_r(s)$. However, for the RCS, the asymptotic tracking may not occur if the internal model of $r(t)$ is present only in the BLS of R [23]. This indicates that replacing the PI by the PCI could lead to the loss of the fundamental property of the linear integral [23], such as zero steady-state error. Additionally, in terms of the engineering perspective, a practical plant is subject to multiple inputs such as disturbance and noise and also exhibit its nonlinearity. The PCI cannot provide a constant buffer force to compensate for these undesired disturbances and the machines' nonlinearity, as its state is persistently reset to zero when zero error is achieved.

To achieve zero steady-state error, the PCI-controlled system needs to add an extra linear integrator to compensate for the lost fundamental property of integration and achieve zero steady-state error. One potential approach is to add a PI after the PCI to form a double-proportional-integrator PCI-PI. However, the experimental measurement analysis in Section III-D demonstrates that even though zero steady-state error is achieved, it takes significantly long time to reach this state and the settling time is strictly deteriorated compared to the LTI PID system. More PI action could reduce those time to reach zero steady-state error, but it also reduces the beneficial PCI action, leading to less phase margin around the bandwidth or less suppression of low-frequency disturbances. Another state-of-art solution, called PI+CI structure, shares a similar trade-off. In this approach, an integrator PI is added in parallel with the CI to form a nonlinear proportional integrator with partial reset, and two integral terms are used to separately tune the action between the PI and CI [30]. However, the PI+CI structure exhibits a property wherein a lower integral term of CI leads to a larger phase lag. Thus, the PI+CI solution encounters the same trade-off as the PCI-PI approach when using more PI action to reduce the time taken to reach zero steady-state error, which results in less advantage from the PCI action. In summary, introducing the PI for the PCI integrator to achieve asymptotic tracking results in a trade-off, leading to either a reduction in phase

margin or a decrease in the nonlinear benefits gained from the PCI. To overcome this limitation, a novel reset integrator GFbI is proposed to replace the traditional reset integrator CI.

The novel reset integrator GFbI consists of two elements: a linear element PI and a reset element GFORE with a corner frequency ω_r. The integrator GFbI allows for achieving zero steady-state error while preserving the advantage of applying the reset action, providing a promising solution for enhanced control performance. The structure of GFbI is depicted in Fig. 15(a), with the PI placed after the reset element GFORE to guarantee the achievement of zero steady-state error, and $\omega_{i-\text{PGFbI}} \in \mathbb{R}_{>0}$ is utilized to adjust the gain of GFbI.

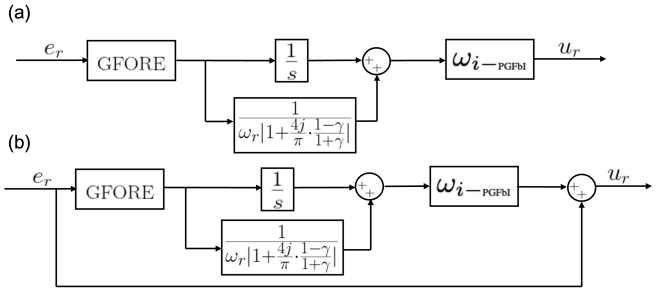

Fig. 15. (a) GFbI block diagram, (b) PGFbI block diagram.

The DF formation of the GFbI in Fig. 16 demonstrates the principle and composition of the GFbI. At the low frequency range $[0, \omega_r]$, the PI is activated, and the GFORE acts as a resetting first-order low pass filter working above ω_r. Therefore, the DF behavior of the GFbI resembles the FRF of a PI with -20dB/dec in magnitude and 90° phase lag in the range $[0, \omega_r]$, and it exhibits the same magnitude slope and phase lag as the DF of CI above ω_r. Compared to the traditional CI, GFbI, as a single reset integrator, could achieve zero steady-state error by internally incorporating a linear integrator PI after the reset element GFORE, while GFbI could retain the advantage of reduced phase lag after ω_r, resulting from the application of the reset action.

Similar to the transition from the CI to PCI, the Proportional Generalized First Order Reset Element-based Integrator (PGFbI) is derived from the GFbI, with the structure shown in Fig. 15(b). For the PGFbI structure, $\omega_{i-\text{PGFbI}}$ is the cut-off frequency of the PGFbI. By ensuring the same phase lag at a specified frequency, the comparative analysis between PI, PCI, and PGFbI in Fig. 17 demonstrates that both PCI and PGFbI achieve superior performance in terms of increased bandwidth and elevated open-loop gain. This enhancement presents the effectiveness of reset controllers in overcoming traditional LTI limitations. Furthermore, PGFbI, in addition to sharing the same advantages in improvement in bandwidth and low-frequency disturbance suppression as PCI, is capable of achieving zero steady-state error due to the presence of a linear integrator PI after the reset element. Another noteworthy advantage of the PGFbI is its ability to exhibit lower HOSIDFs compared to the PCI, as illustrated in Fig. 17. This improvement stems from the replacement of reset action in the low-frequency range $[0, \omega_r]$ with PI

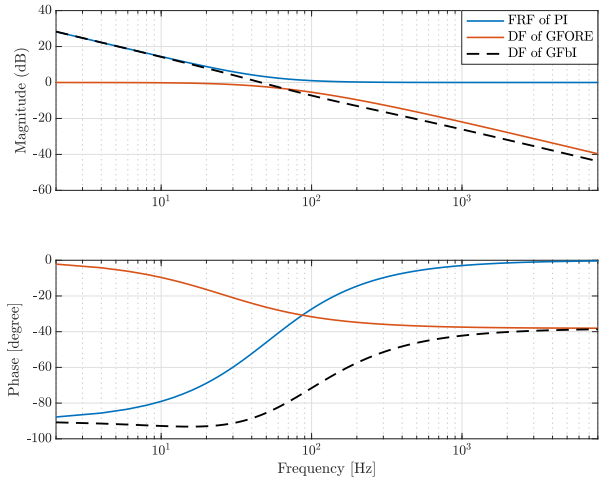

Fig. 16. DF formation of GFbI, along with the parameters $\gamma = 0$, $\omega_r = 51.75$ Hz, and $\omega_{i-\text{PGFbI}} = 52$ Hz.

action in PGFbI. Consequently, for the same $\omega_{i-\text{PGFbI}}$ and $\omega_{i-\text{PCI}}$ values, PGFbI utilizes less reset action compared to PCI, leading to lower magnitudes of the HOSIDFs.

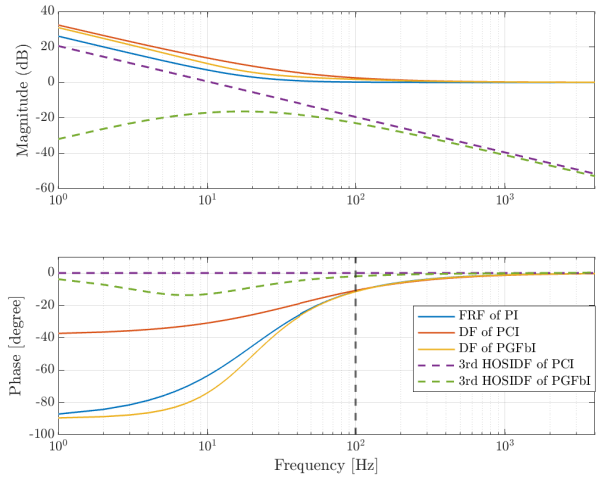

Fig. 17. Comparison of the frequency-domain characteristics between PI, PCI and PGFbI, by ensuring the same phase lag at a selected bandwidth as 100 Hz

Replacing the PI by PCI to break the traditional LTI limitations could lead to the issue of the RCS being unable to achieve zero steady-state error. The existent solutions PCI-PI and PI+CI structures overcome this problem by adding an extra PI into the RCS with the PCI, but this introduces a trade-off of reduced phase margin and increased modulus margin due to the additional PI. Nevertheless, the novel solution PGFbI integrator contains a built-in PI, allowing PGFbI itself to achieve the zero steady-state error without requiring an extra linear integrator PI. PGFbI reduces the reset action by replacing the reset action only in the low-frequency range with linear PI action. This replacement is

advantageous because the low-frequency range, where the PI action is activated, could be far away from the bandwidth frequency and the frequencies where disturbances mainly occur. As a result, the replacement has limited effects on the system's performance in terms of robustness (phase margin) and disturbances suppression. This allows PGFbI to achieve the desired reduction in reset action without compromising the system's stability and disturbance rejection capabilities.

To better understand the advantages of GFbI, it is essential to consider that the strategies of PCI-PI and PI+CI require activating low-frequency reset action within $[0, \omega_r]$ that contributes little to the system's performance. This necessitates extra linear PI action to compensate for the nonlinearity and reduce limit cycles. However, with GFbI, the low-frequency reset action is replaced by PI integration, which can further compensate for the nonlinear reset action at mid- and high-frequency ranges. As a result, PGFbI achieves a reduction in reset action and limit-cycling behavior, while ensuring only a limited loss of the system's benefits from the advantage of reset nonlinearity.

Due to the special advantages of PGFbI over PCI and PI, PGFbI is applied to replace the PI controller within the PID framework or, equivalently, replace the double integrator PCI-PI within the PCI-PID framework to form a PGFbID controller. In terms of implementing a PGFbID controller within a closed-loop system, the GFORE reset element is regarded as R in Fig. 2, and other LTI elements in Fig. 2 can be expressed as follows:

$$\begin{aligned} C_1 &= \frac{s}{(k_{gg} \cdot s + 1)\omega_{i-\text{PGFbI}}}, \\ C_2 &= \omega_{i-\text{PGFbI}} \left(k_{gg} + \frac{1}{s} \right) \left(\frac{\frac{s}{\omega_d} + 1}{\frac{s}{\omega_t} + 1} \right) k_P, \end{aligned} \tag{16}$$

in which $k_{gg} = \frac{1}{\omega_r |1 + \frac{4j}{\pi} \frac{1-\gamma}{1+\gamma}|}$. By applying the implementation method in (16), we could predict the frequency-domain performance of the PGFbI system through Theorem 2.1 and Theorem 2.2.

B. Tuning procedure of PGFbI

In terms of the PGFbI tuning, its ability to achieve comparably reduced HOSIDFs (in comparison to the PCI) and thus to avoid excessive resets is leveraged. Similar to the tuning procedures of PCI-PID controllers, for tuning a PGFbI integrator within the PGFbID framework, the lead filter is fixed from the original PID controller, and different γ values are considered within $[-0.9, -0.8, -0.7, .., 0.9]$. For each γ value ω_r and $\omega_{i-\text{PGFbI}}$ are optimized. Considering the trade-off between sufficient utilization of nonlinear reset action for significant improvements in bandwidth and disturbance suppression, and adequate involvement of linear PI action to expeditiously reach the stage of zero steady-state error and thus effectively suppress limit cycles, the tuning algorithm of a PGFbI integrator is proposed as

$$\bar{Q} := \begin{cases} \max \ \ \omega_{bw}(\omega_r, \omega_{i-\text{PGFbI}}), \\ \text{s.t.} \ \ \max(S_\infty(\omega_r, \omega_{i-\text{PGFbI}}, \omega)) < 6 \text{ dB}, \\ \qquad N_{ri}(\omega_r, \omega_{i-\text{PGFbI}}, \omega) = 2 \ \ \forall \omega \in [\omega_a, \frac{\omega_s}{2}], \\ \qquad 0 < \omega_{i-\text{PGFbI}} < \frac{\omega_s}{100}, \end{cases} \tag{17}$$

where $\omega_a \in [0, \frac{\omega_s}{2}]$ is a changable parameter.

The cost function and the first constraint and third constraint are set for the same reason as in PCI-PID tuning procedures $\bar{P}_1$ and $\bar{P}_2$, ensuring performance optimization and robustness of the system with PGFbI. However, the introduction of the second constraint related to N_{ri} in $\bar{Q}$ serves a different purpose. While N_{ri} is used as a constraint in $\bar{P}_1$ and $\bar{P}_2$ to meet the assumption of performance prediction method Theorem 2.2, in the optimization problem of $\bar{Q}$, the constraint on N_{ri} is introduced to achieve improved performance, specifically lower HOSIDFs and fewer limit cycles, as well as is used to satisfy the assumption of the applied performance prediction method. As shown in Fig. 17, one of the advantages of PGFbI over PCI is the ability to achieve lower HOSIDFs, indicating a more dominant influence of DF in the pseudo-sensitivity. Consequently, the reduced number of resets from HOSIDFs leads to less frequency ranges with multiple resets, enhancing the RCS performance. The requirement of $N_{ri}(t)(\omega) = 2$ within the tunable interval as $[\omega_a, \frac{\omega_s}{2}]$ allows for the tuning of different suppression levels of undesired HOSIDFs by adjusting ω_a. Specifically, a lower value of ω_a indicates a more narrow frequency range with undesired multiple resets, which in turn means lower HOSIDFs within the RCS. As a result, designers have the flexibility to fine-tune ω_a to control the suppression levels of undesired HOSIDFs. Simultaneously, adjusting ω_a could determine the extent of improvements in bandwidth and disturbances suppression with the PGFbID controller. This provides a high level of flexibility in meeting specific system requirements and optimizing the performance of the control system according to different applications.

The tuning algorithm $\bar{Q}$ requires the $N_{ri}(\omega) = 2$ to limit the relative strength of DF compared to HOSIDF. The practical integration of the optimization problem involves using the changeable parameter ω_a to adjust the frequency range of ω satisfying $N_{ri}(\omega) = 2$, and assists in quantifying the relative strength of HOSIDFs and DF. It is noteworthy that the constraint of $N_{ri}(\omega) = 2$ within a changeable frequency range for PGFbID tuning can also be applied to other RCSs to limit the strength of undesired HOSIDFs and achieve superior performance. This approach offers a versatile and effective means to optimize various RCS control strategies while considering their unique characteristics and requirements.

To solve the optimization problem $\bar{Q}$ in a computationally tractable manner, a two-level nested bisection approach is employed. The design of these nested bisection loops is grounded on the assumption that $\max(S_\infty)$ behaves as a convex function with respect to $\omega_{i-\text{PGFbI}}$ while keeping γ

and ω_r fixed. In this approach, the inner bisection loop, corresponding to a specific γ and ω_r, utilizes the bisection method to determine the highest attainable $\omega_{i-\text{PGFbI}}$ that maximizes the ω_{bw} while satisfying the first constraint. The outer bisection loop, revolving around ω_r, aims to pinpoint the minimum value of ω_r which ensures that the corresponding optimized $\omega_{i-\text{PGFbI}}$ from the inner loop adheres to the second constraint. The choice of the minimum ω_r stems from that for PGFbI controller, a lower ω_r corresponds to a diminished utilization of the PI action. Given the objective of maximizing the benefits from the nonlinear reset action for breaking traditional LTI limitations, minimizing the usage of the linear PI component is preferred. For each γ, these two nested bisection loops are functionalized to find its corresponding optimal ω_r and $\omega_{i-\text{PGFbI}}$ (i.e. the allowable minimum ω_r and maximum $\omega_{i-\text{PGFbI}}$).

C. Experimental results analysis

In order to validate the feasibility of PGFbI in reducing undesired HOSIDFs and decreasing limit-cycling behavior with less compromising other performances compared to PCI-PI, the experimental results are preferably analyzed, since the limit cycles caused by the nonlinearity of the plant could be properly observed only from the experimental data. The PGFbID controller is tuned based on the algorithm $\bar{Q}$ with setting $\omega_a = 0$ for each γ from $[-0.9, -0.8, -0.7, ..., 0.9]$, indicating the minimum two reset times per period is rigorously required to significantly suppress undesired HOSIDFs within the RCS. The parameters of the optimized PGFbID systems and their corresponding system performance parameters are shown in Table III. The performance parameters ω_{bw} and $S_\infty(\omega_{bfv})$ of the optimized PGFbID systems with different γ values are depicted in Fig. 18. Similar to the experiments conducted for the PCI-PID systems, two specific cases are selected for comparison: the traditional reset $\gamma = 0$ and the $\gamma = 0.1$ yielding the best performance (the largest bandwidth and lowest $S_\infty(\omega_{bfv})$). These two cases are tested on the Yθ table introduced in Section III-D.1. Subsequently, the experimental results of the optimized PGFbID systems with $\gamma = 0$ and $\gamma = 0.1$ are compared and analyzed in the following.

The open-loop analysis in Fig. 19 compares the optimized PCI-PID system tuned by $\bar{P}_1$ and $\bar{P}_2$ with the optimized PGFbI system tuned by $\bar{Q}$, both with $\gamma = 0$. The performance parameters such as bandwidth and phase margin of each system are listed in Table IV, derived from the data visualized in Fig. 19. Upon analyzing the results in Table IV and Fig. 19, several key observations can be made. Firstly, both PGFbID systems with $\gamma = 0$ and $\gamma = 0.1$ show improvements in bandwidth and low-frequency open-loop gain compared to the original PID system, while maintaining almost the same phase margin. This indicates better suppression of low-frequency disturbances by the PGFbID systems. When comparing with the PCI-PID system with $\gamma = 0$, the PGFbID system with $\gamma = 0$ could achieve the reduction in undesired HOSIDFs. On the other hand, we could also find that the PCI-PID ($\gamma = 0$) system exhibits relatively larger DF

TABLE III

OPTIMIZED PGFBID SYSTEMS WITH DIFFERENT γ, WITH THE PLANT AS THE TRANSLATION MOTION OF Yθ TABLE.

PGFbI controller			System performance parameters		
γ	ω_r [Hz]	$\omega_{i-\text{PGFbI}}$[Hz]	max(S_∞) (dB)	ω_{bw} [Hz]	$S_\infty(\omega_{bfv})$ (dB)
-0.9	64.688	65.000	5.995	242.500	-5.108
-0.8	68.750	70.000	5.996	245.000	-5.311
-0.7	72.500	73.125	5.992	247.500	-5.479
-0.6	73.750	75.313	5.994	250.000	-5.677
-0.5	73.750	76.250	5.997	255.000	-5.877
-0.4	73.750	74.375	5.990	257.500	-6.010
-0.3	73.750	71.875	5.999	257.500	-6.126
-0.2	72.500	68.125	5.991	260.000	-6.223
-0.1	69.375	64.688	5.995	260.000	-6.346
0	67.500	61.250	5.998	260.000	-6.409
0.1	64.375	57.813	5.993	257.500	-6.451
0.2	62.500	55.000	5.995	255.000	-6.436
0.3	57.500	52.188	5.994	255.000	-6.415
0.4	53.750	50.000	5.995	252.500	-6.331
0.5	48.750	48.438	5.996	250.000	-6.221
0.6	43.750	47.344	5.995	247.500	-6.064
0.7	37.500	46.875	5.998	247.500	-5.878
0.8	29.961	46.563	5.993	245.000	-5.644
0.9	22.500	46.875	5.998	242.500	-5.376

Note: Gain controllers and lead filters are consistent across controller groups, where $k_P = 3518300$, $\omega_d = 79.167$ Hz and $\omega_t = 356.25$ Hz. Frequency parameters are scaled by $\eta{*}10^4$ for confidentiality and readability.

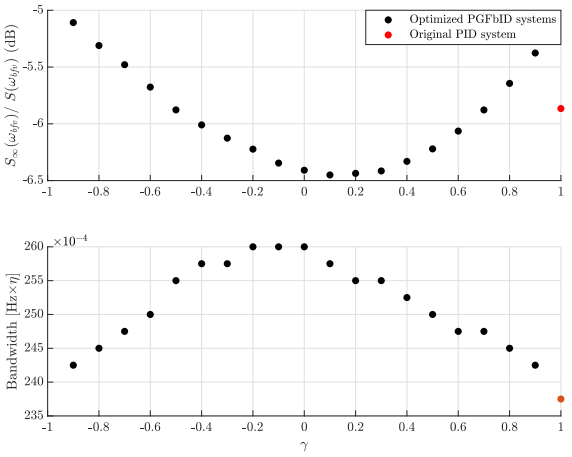

Fig. 18. Bandwidth, $S_\infty(\omega_{bfv})$ of optimized PGFbID systems with different γ and $S(\omega_{bfv})$ of the original PID system ($\gamma = 1$), with the plant as translation motion of the moving mass of Yθ table.

compared to the ones of PGFbID system ($\gamma = 0$). In fact, this larger open-loop gain can be interpreted as the disadvantage of the PCI-PID system. This is because that such larger open-loop gain of the PCI-PID results from the two integrators PCI and PI being simultaneously applied at the low frequency range. In contrast, the PGFbID system activates only the PI at the low-frequency range, which avoids the negative impact of the undesired low-frequency reset action and allows for a faster elimination of limit cycles. Furthermore, the higher open-loop of PCI-PID system is shown below around 10Hz, which is far away from the base frame vibration frequency. This indicates that the influence of the low-frequency open-loop gain on the system's performance is limited. Overall, the comparison shows that the PGFbID system outperforms the PCI-PID system in terms of reduced higher-order harmonics and avoiding less helpful reset action at the low-frequency

range, while achieving improved bandwidth and better suppression of low-frequency disturbances.

TABLE IV

PERFORMANCE COMPARISON WITH THE OPTIMIZED PCI-PID ($\gamma = 0$), OPTIMIZED PGFBID SYSTEM ($\gamma = 0$), AND ORIGINAL PID SYSTEM.

	Original PID	PCI-PID ($\gamma = 0$)	PGFbID $\gamma = 0$	PGFbID $\gamma = 0.1$
Bandwidth [Hz×η]	$237.5{*}10^{-4}$	$270{*}10^{-4}$	$260{*}10^{-4}$	$260{*}10^{-4}$
Phase margin [°]	32.049	33.842	33.093	33.058

The closed-loop performance analysis, as visualized in Fig. 20, provides further insights into the behavior of the PGFbID systems. In the case of PGFbID systems, the less useful low-frequency reset action is replaced by the linear PI action, allowing for the achievement of two reset instants at the entire frequency range $[0, \frac{\omega_s}{2}]$. Moreover, $N_{ri} = 2$ at the whole frequency domain leads to that DF mainly results in the reset and thus DF is dominant in pseudo-sensitivity S_∞, indicating that therefore S_∞ could be closed to the DF S_1 of PGFbID system. This stands in notable contrast to the PCI-PID systems, where S_∞ cannot always be smaller than S of the original PID system throughout the entire frequency range, as mentioned in Section III-C.2. The PGFbID system can consistently achieve S_∞ smaller than S, due to its lower HOSIDFs. In summary, the closed-loop performance analysis of the PGFbID systems demonstrates their ability to reduce HOSIDFs, avoid less useful reset action and therefore reduce limit cycles, and achieve improved performance across the entire frequency range. This characteristic distinguishes them from the PCI-PID systems, making PGFbID a more effective and promising control solution for systems with the plant's nonlinearity and disturbances.

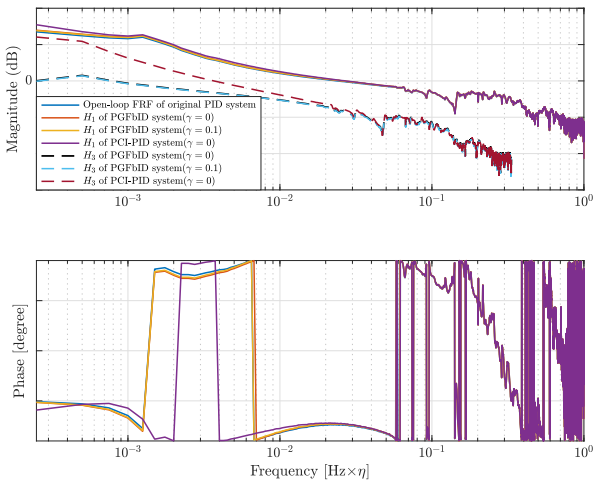

Fig. 19. Magnitude and phase characteristics of the DF and 3rd HOSIDF of the open-loop optimized PCI-PID system with $\gamma = 0$ and the optimized PGFbID system with $\gamma = 0$ and $\gamma = 0.1$, and the open-loop FRF of the original PID system, with the experimental setup as Yθ table.

Following the frequency-domain analysis in the open-loop and closed-loop, a time-domain analysis is performed using the error signal during the settling phase. Fig. 21 presents the results for all nonlinear systems: the PCI-PID system with

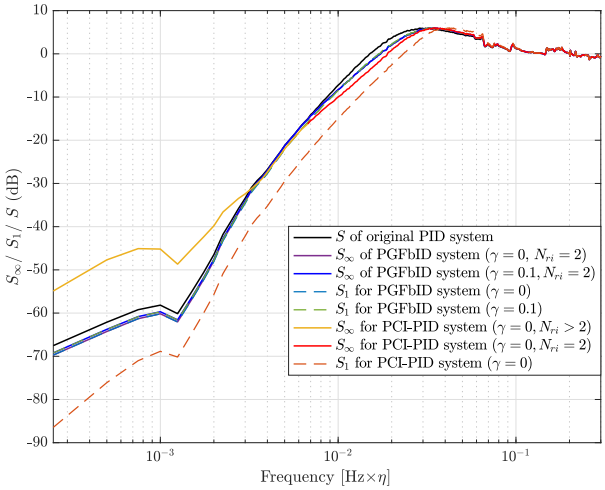

Fig. 20. S_∞ and S_1 of the optimized PGFbID systems with $\gamma = 0$ and $\gamma = 0.1$, S_∞ and S_1 of the optimized PCI-PID systems with $\gamma = 0$, and S of the original PID system, with the plant as the translation dynamics of Yθ table.

$\gamma = 0$, the PGFbID system with $\gamma = 0$, and the PGFbID system with $\gamma = 0.1$. All three systems achieve reduced undershoot compared to the original PID system. However, in contrast to the optimized PCI-PID system ($\gamma = 0$) suffering from limit cycles, the PGFbID systems optimized by the algorithm effectively suppresses these undesired limit cycles. Regarding the spectrum analysis of the error signal during the settling phase, Fig. 21 reveals that the optimized PCI-PID system ($\gamma = 0$) exhibits the largest CPSD due to the presence of undesired limit cycles, which introduce significant power in the signal. In contrast, both optimized PGFbID systems with $\gamma = 0$ and $\gamma = 0.1$ effectively reduce the CPSD compared to the original PID system and the optimized PCI-PID system, due to their ability to reduce the HOSIDFs and suppress the limit-cycling behavior. Moreover, the PGFbID system with $\gamma = 0.1$ achieves a smaller CPSD compared to the PGFbID system with $\gamma = 0$, indicating better suppression of base frame vibrations, as predicted by the S_∞ analysis. Finally, based on the tuning algorithm of $\bar{Q}$ with $\omega_a = 0$, the optimal PGFbID system with $\gamma = 0.1$ achieves a 30.88% reduction in steady-state RMS error compared to the original LTI PID system. This performance improvement in precision further highlights the effectiveness of the PGFbID controller with the existence of the plant's nonlinearity and disturbances, making it a promising control strategy for real-world motion systems.

TABLE V

NORMALIZED e_{RMS} DERIVED FROM EXPERIMENTS WITH DIFFERENT CONTROLLER STRUCTURES.

	Original PID	PCI-PID($\gamma = 0$)	PCI-PID($\gamma = -0.9$)	PGFbID($\gamma = 0$)	PGFbID($\gamma = 0.1$)
e_{RMS}	1	0.7844	0.8503	0.8704	0.6912

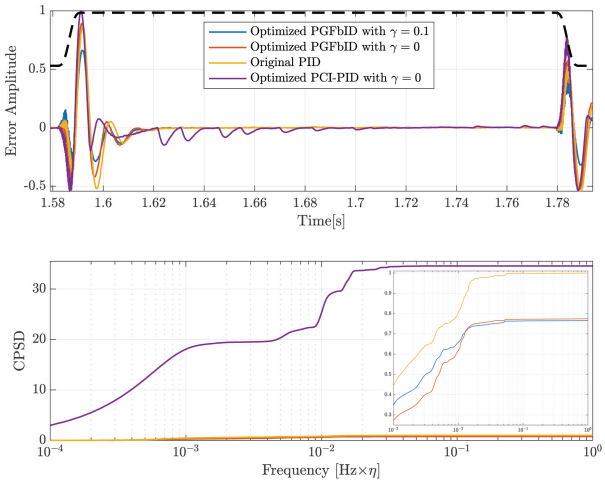

Fig. 21. Normalized error signals at the settling phase obtained from experiments conducted on the Yθ table with a typical reference trajectory (the reference is scaled), and its corresponding frequency-domain spectrum analysis as CPSD, which is based on processing the error signal at the settling phase with adding Hanning windows.

V. Conclusion

In this work, a reset element PCI is employed to replace the linear PI controller for breaking the traditional LTI limitations, such as the water-bed effect and Bode's gain-phase relationship. To achieve optimal performance, the sequence of the PCI-PID controller is determined while considering practical aspect as input noises. The tuning algorithms of PCI-PID controller, considering both open-loop and closed-loop requirements, are proposed to maximize the system performance in terms of the bandwidth and suppression of low-frequency disturbances, such as the base frame vibration. Simulation validation confirms that the PCI-PID controller, along with its tuning algorithms, bring the improvement in bandwidth and disturbance suppression compared to the traditional PID system. During the experiments on an industrial motion platform, the tuning procedures enable the PCI-PID system to achieve a lower RMS error within the settling phase compared to the original LTI PID system. However, due to the nature of the PCI integrator, which cannot provide a constant buffer force to compensate for plant nonlinearity and input disturbances, undesired limit-cycling behavior is observed in the experimental results of PCI-PID systems. These limit cycles adversely affect system performance and extend settling times. To address these limit cycles, existent solutions necessities the involvement of an extra linear integrator PI to the PCI element, forming structures such as PCI-PI and PI+CI. Nevertheless, the introduction of the PI creates a trade-off, resulting in a reduction in phase margin or a decrease in the nonlinear benefits gained from the PCI.

To overcome the limitations associated with introducing an extra PI, a novel reset integrator called GFbI is proposed, along with its corresponding PGFbI structure. The GFbI internally incorporates a PI, allowing it to provide a constant buffer force to compensate for the unexpected machine nonlinearity and undesired disturbances, without requiring the addition of an external linear integrator. This unique characteristic allows the system with GFbI to attain zero steady-state error and avoid the undesired limit cycles, without being confined by the limitations associated with introducing an additional PI. Besides, the PGFbI also exhibits the characteristic of less HOSIDFs compared to the PCI integrator, while maintaining other similar system performance parameters. The reduced HOSIDFs assists the PGFbI system avoid excessive resets. In terms of the PGFbI tuning, we leverage its ability to achieve multiple resets in a fewer frequency range. By applying a changeable frequency range and requiring a minimum of two reset times per period, we can define different suppression levels of the system's HOSIDFs and limit cycles based on design requirements. In this work, two rest instants is required to achieve at the whole measured frequency range. By utilizing this constraint, the experimental results demonstrate that the PGFbI system could achieve the lowest CPSD compared to both the original PID system and optimized PCI-PID systems, and could effectively suppress undesired limit cycles and base frame vibrations. This experimental proof indicates that PGFbI structure could improve the machine's performance from the original PID controller without being inherently limited like PCI-PID systems. Finally, the system with the PGFbI controller achieves the best performance, with a 30.88% reduction in the RMS error within the settling phase when compared to the original PID controller.

The experimental results demonstrate that the PGFbI system, with its property of lower HOSIDFs compared to the PCI, achieves fewer limit cycles compared to the PCI-PID system. This suggests that the PCI-PID controller, when combined with reset elements capable of reducing the magnitude of HOSIDFs in RCS, such as the continuous reset element [15], could possibly also achieve improved performance with proper tuning. Furthermore, the requirement of suppressing HOSIDFs, along with its practical implementation by requiring two reset instants within a tunable frequency range, as utilized in the PGFbID tuning algorithm $\bar{Q}$, can be applied to other RCSs to limit the strength of undesired HOSIDFs and achieve superior performance.

For future work recommendations, it would be beneficial to enhance the tuning algorithms for both PCI-PID controllers and PGFbID controllers by considering the tuning of the lead filter. By optimizing the lead filter in conjunction with the reset elements PCI and PGFbI, better performance for RCSs can be achieved. Another meaningful aspect of future work would be to focus on the stability guarantee of the novel PGFbI integrator, and stability considerations should be incorporated into the tuning algorithms of PCI-PID and PGFbID controllers. Furthermore, it would be valuable to develop more accurate performance prediction methods in the frequency domain. This could involve the development of methods that do not rely on some assumptions, such as the one assuming only the first-order harmonic of the input to the reset controller results in reset actions and the requirement for two reset instants per period. The pursuit of more accurate performance predictions would contribute to enhanced reset

controller design and overall system performance.

REFERENCES

[1] K. J. Åström and T. Hägglund, "The future of pid control," *Control engineering practice*, vol. 9, no. 11, pp. 1163–1175, 2001.

[2] H. W. Bode, "Network analysis and feedback amplifier design," Van Nostrand, 1945.

[3] S. Skogestad and I. Postlethwaite, *Multivariable feedback control: analysis and design*. john Wiley & sons, 2005.

[4] W. C. Foster, D. L. Gieseking, and W. K. Waymeyer, "A Nonlinear Filter for Independent Gain and Phase (With Applications)," *Journal of Basic Engineering*, vol. 88, no. 2, pp. 457–462, 06 1966.

[5] D. Deenen, M. Heertjes, W. Heemels, and H. Nijmeijer, "Hybrid integrator design for enhanced tracking in motion control," in *2017 American Control Conference (ACC)*, 2017, pp. 2863–2868.

[6] J. C. Clegg, "A nonlinear integrator for servomechanisms," *Transactions of the American Institute of Electrical Engineers, Part II: Applications and Industry*, vol. 77, no. 1, pp. 41–42, 1958.

[7] S. van Loon, B. Hunnekens, W. Heemels, N. van de Wouw, and H. Nijmeijer, "Split-path nonlinear integral control for transient performance improvement," *Automatica*, vol. 66, pp. 262–270, 2016.

[8] B. Sharif, A. van der Maas, N. van de Wouw, and W. P. M. H. Heemels, "Filtered split-path nonlinear integrator: A hybrid controller for transient performance improvement," *IEEE Transactions on Control Systems Technology*, vol. 30, no. 2, pp. 451–463, 2022.

[9] P. Nuij, O. Bosgra, and M. Steinbuch, "Higher-order sinusoidal input describing functions for the analysis of non-linear systems with harmonic responses," *Mechanical Systems and Signal Processing*, vol. 20, no. 8, pp. 1883–1904, 2006.

[10] L. F. van Eijk, S. Beer, R. M. J. van Es, D. Kostić, and H. Nijmeijer, "Frequency-domain properties of the hybrid integrator-gain system and its application as a nonlinear lag filter," *IEEE Transactions on Control Systems Technology*, vol. 31, no. 2, pp. 905–912, 2023.

[11] N. Saikumar, K. Heinen, and S. H. HosseinNia, "Loop-shaping for reset control systems: A higher-order sinusoidal-input describing functions approach," *Control Engineering Practice*, vol. 111, p. 104808, 2021.

[12] N. Saikumar, K. Henen, and S. H. HosseinNia, "Corrigendum to "loop-shaping for reset control systems: A higher-order sinusoidal-input describing functions approach" [control engineering practice 111 (2021) 104808]," *Control Engineering Practice*, vol. 137, p. 105565, 2023.

[13] A. A. Dastjerdi, A. Astolfi, N. Saikumar, N. Karbasizadeh, D. Valério, and S. H. HosseinNia, "Closed-loop frequency analysis of reset control systems," *IEEE Transactions on Automatic Control*, vol. 68, no. 2, pp. 1146–1153, 2023.

[14] A. A. Dastjerdi, A. Astolfi, and S. H. HosseinNia, "A frequency-domain stability method for reset systems," in *2020 59th IEEE Conference on Decision and Control (CDC)*. IEEE, 2020, pp. 5785–5791.

[15] N. Karbasizadeh and S. H. HosseinNia, "Continuous reset element: Transient and steady-state analysis for precision motion systems," *Control Engineering Practice*, vol. 126, p. 105232, 2022.

[16] N. Saikumar, R. K. Sinha, and S. H. HosseinNia, ""constant in gain lead in phase" element–application in precision motion control," *IEEE/ASME Transactions on Mechatronics*, vol. 24, no. 3, pp. 1176–1185, 2019.

[17] E. Akyüz, N. Saikumar, and S. H. HosseinNia, "Reset control for vibration disturbance rejection," *IFAC-PapersOnLine*, vol. 52, no. 15, pp. 525–530, 2019.

[18] R. M. Schmidt, G. Schitter, and A. Rankers, *The Design of High Performance Mechatronics: High-Tech Functionality by Multidisciplinary System Integration*. Ios Press, 2020.

[19] A. A. Dastjerdi, N. Saikumar, and S. H. HosseinNia, "Tuning guidelines for fractional order pid controllers: Rules of thumb," *Mechatronics*, vol. 56, pp. 26–36, 2018.

[20] Y. Guo, Y. Wang, L. Xie, H. Li, and W. Gui, "Optimal reset law design of reset control systems with application to hdd systems," in *Proceedings of the 48h IEEE Conference on Decision and Control (CDC) held jointly with 2009 28th Chinese Control Conference*. IEEE, 2009, pp. 5287–5292.

[21] M. Vidyasagar, *Nonlinear systems analysis*. SIAM, 2002.

[22] A. Gelb and W. E. Vander Velde, *Multiple-input describing functions and nonlinear system design*. McGraw-Hill, 1968.

[23] O. Beker, C. Hollot, Y. Chait, and H. Han, "Fundamental properties of reset control systems," *Automatica*, vol. 40, no. 6, pp. 905–915, 2004.

[24] K. Krishnan and I. Horowitz, "Synthesis of a non-linear feedback system with significant plant-ignorance for prescribed system tolerances," *International Journal of Control*, vol. 19, no. 4, pp. 689–706, 1974.

[25] Y. Guo, Y. Wang, and L. Xie, "Frequency-domain properties of reset systems with application in hard-disk-drive systems," *IEEE Transactions on Control Systems Technology*, vol. 17, no. 6, pp. 1446–1453, 2009.

[26] A. Barreiro, A. Baños, S. Dormido, and J. A. González-Prieto, "Reset control systems with reset band: Well-posedness, limit cycles and stability analysis," *Systems & Control Letters*, vol. 63, pp. 1–11, 2014.

[27] M. Vanderbroeck, "Damping analysis of reset control systems: an analytical approach," Master's Thesis, Delft University of Technology, 2022.

[28] C. Cai, A. A. Dastjerdi, N. Saikumar, and S. HosseinNia, "The optimal sequence for reset controllers," in *2020 European Control Conference (ECC)*, 2020, pp. 1826–1833.

[29] A. Banos and A. Vidal, "Design of reset control systems: the pi+ ci compensator," *Journal of Dynamic Systems, Measurement, and Control*, vol. 134, no. 5, 2012.

[30] A. Baños and A. Vidal, "Definition and tuning of a pi+ci reset controller," in *2007 European Control Conference (ECC)*, 2007, pp. 4792–4798.

[31] G. Bengtsson, "Output regulation and internal models—a frequency domain approach," *Automatica*, vol. 13, no. 4, pp. 333–345, 1977.

APPENDIX

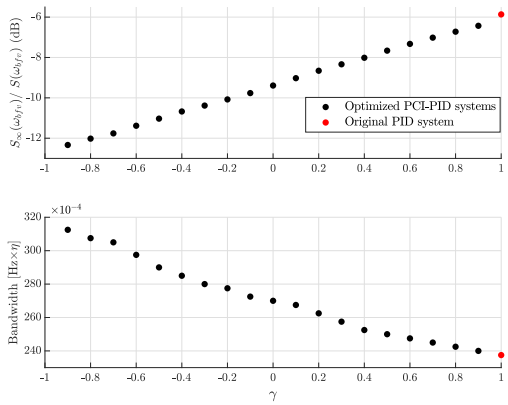

Fig. 22. Bandwidth, $S_\infty(\omega_{bfv})$ of optimized PCI-PID systems with different γ and $S(\omega_{bfv})$ of the original PID system ($\gamma = 1$), with the plant as the translation dynamics of the Yθ table.

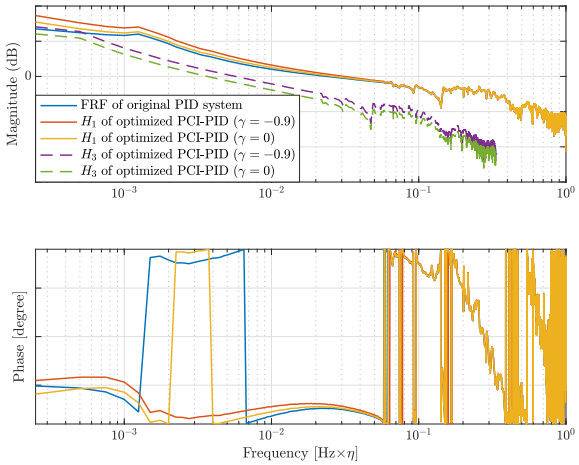

Fig. 23. Magnitude and phase characteristics of the DF and 3rd HOSIDF of the open-loop optimized PCI-PID system with $\gamma = 0$ and $\gamma = -0.9$ and the original PID system, for the experimental setup Yθ table.

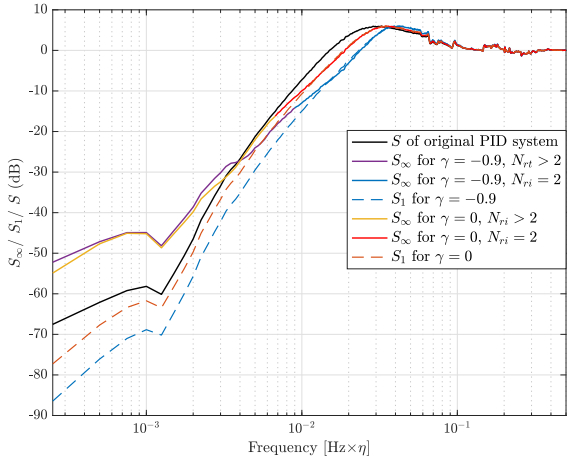

Fig. 24. S_∞ and S_1 of the optimized PCI-PID systems with $\gamma = 0$ and $\gamma = -0.9$, and S of the original PID system, with the plant as the translation dynamics of Yθ table.

Chapter 4

CONCLUSIONS AND FUTURE WORK RECOMMENDATIONS

4.1 Conclusions

In this study, the utilization of a reset element PCI aims to replace the traditional linear PI controller, addressing inherent LTI limitations such as the water-bed effect and Bode's gain-phase relationship. The optimal sequence for the PCI-PID controller is discussed, taking into account of practical aspects such as input noise, to achieve superior performance. Tuning algorithms for the PCI-PID controller, catering to both open-loop and closed-loop requirements, are proposed to optimize system performance through maximizing bandwidth and suppression of low-frequency disturbances, including base frame vibrations. Simulation validation confirms the efficacy of the PCI-PID controller and its tuning algorithms in enhancing bandwidth and disturbance attenuation in comparison to the conventional PID system. Experimental validation using a wire bonder demonstrates that the proposed tuning procedures result in the PCI-PID system achieving reduced Root Mean Square (RMS) error during the settling phase, as opposed to the original LTI PID system. However, inherent to the PCI integrator's characteristics, it falls short in providing a consistent buffer force to counteract plant nonlinearity and input disturbances, leading to undesired limit-cycling behavior observed in the experimental results of PCI-PID systems. These limit cycles have a detrimental impact on system performance, leading to the extended settling time. Addressing this concern, established solutions require the inclusion of an additional linear integrator PI to the PCI element, resulting in configurations such as PCI-PI and PI+CI. However, the requirement of an additional PI introduces a trade-off, either diminishing phase margin or reducing the nonlinear benefits accrued from the PCI.

In light of these limitations related to introducing an additional PI, this work introduces a novel reset integrator named GFbI, accompanied by its corresponding PGFbI structure. The GFbI internally incorporates a PI, allowing it to provide a constant buffer force to compensate for the unexpected machine nonlinearity and undesired disturbances, without requiring the addition of an external PI. This unique feature empowers the GFbI system to attain zero steady-state error and circumvent undesired limit cycles, avoiding the constraints posed by introducing an additional PI. Furthermore, the PGFbI outperforms the PCI integrator by exhibiting fewer HOSIDFs while maintaining other performance parameters. Leveraging the PGFbI's ability to exhibit less HOSIDFs, a changeable frequency range approach coupled with a requirement for a minimum of two reset times per period is applied for PGFbI tuning to define distinct suppression levels for the system's HOSIDFs. Experimental outcomes demonstrate that applying this constraint enables the PGFbI system to yield the lowest CPSD compared to both the original PID system and optimized PCI-PID systems. Besides, experimental results also prove that the ability of PGFbI along with

its tuning algorithm to achieve reduced limit cycles compared to the optimized PCI-PID systems. These experimental findings underscore the capacity of the PGFbI structure to enhance machine performance beyond the limitations inherent in the original PID controller and in the PCI-PID system. Ultimately, the system controlled by the PGFbI controller achieves the best performance, showcasing a remarkable 30.88% reduction in the RMS error during the settling phase compared to the original PID controller, which currently employed to regulate the motion of the wire bonder.

4.2 Future work recommendations

While this study has underscored the potential of reset control, it is evident that additional research and development efforts are essential to fully utilize the advantages it offers. As a result, the following recommendations for future research are provided:

1. Regarding the tuning algorithms for PCI-PID controllers $\bar{P}_1$ and $\bar{P}_2$, the lead filters are kept consistent with the one of the original PID controllers and remain unchanged throughout the tuning process. However, it is important to note that the lead filter design from the original PID controller was based on a relatively low bandwidth (the bandwidth of the original PID controller) and does not account for improvements of bandwidth achieved through the application of reset controllers. For example, as shown in TABLE II, the lead filter designed for a bandwidth of 171 Hz may no longer be suitable for PCI-PID systems with significantly increased bandwidth s (for $\gamma = 0$ and 225 Hz for $\gamma = -0.9$) resulting from applying reset action. It is meaningful that adjusting the lead filter based on the improved bandwidth resulting from applying the optimized PCI controller, since the primary role of the lead filter is to provide substantial phase lead around the bandwidth of the system. Some preliminary efforts have been made in this direction. The lead filter is initially fine-tuned according to the improved bandwidth. This adjustment often leads to a reduction in $\max(S_\infty)$, which in turn provides more leeway for further increases in $\omega_{i-\mathrm{PCI}}$ of the PCI filter, thereby benefits derived from reset actions could be further increase.

This idea has been explored in terms of design and simulations. However, upon analyzing the results, it is apparent that the anticipated further bandwidth increase resulting from lead filter tuning and expanding $\omega_{i-\mathrm{PCI}}$ after $\bar{P}_1$ does not exhibit consistency across all γ values. As depicted in Figure 4.1, for relatively small γ values (from -0.8 to -0.4), a bandwidth increase is observed, while for larger γ values (from 0 to 0.7), a decrease in bandwidth is noted. As a result, it becomes imperative to develop a tuning method for the lead filter and the expansion $\omega_{i-\mathrm{PCI}}$ of that can consistently lead to bandwidth enhancement across all γ values. Furthermore, the tuning of the lead filter can result in an increased of $\omega_{i-\mathrm{PCI}}$, which in turn has the potential to introduce more undesired HOSIDFs into the system. This possible deterioration stemming from increased HOSIDFs needs to be taken into consideration while fine-tuning the lead filter within the PCI-PID framework.

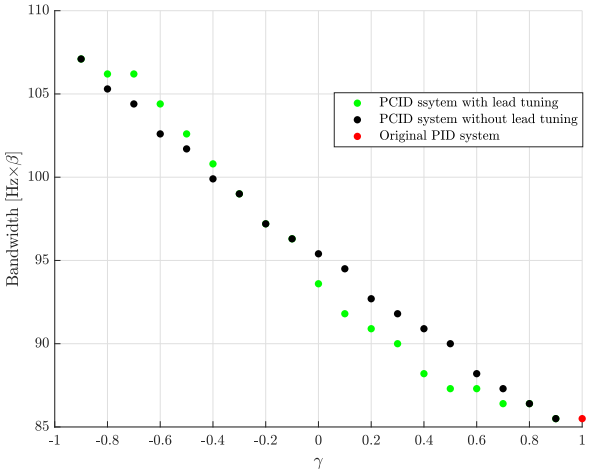

Figure 4.1: Bandwidth of optimized PCID systems with and without tuning lead filters for different γ, with the plant as the Simscape model of AB383 wire bonder.

2. In terms of tuning PGFbI, several comments and future work recommendations are listed.

   - The second constraint about number of reset instants of optimization problem $\bar{Q}$, as mentioned in Chapter 3, could similarly be extended to the tuning of other reset elements to mitigate their undesired HOSIDFs. For example, the author would recommend apply this constraint into the tuning of CR element [20], primarily aimed at HOSIDF suppression within a RCS, while ensuring minimal impact on DF.

   - Drawing inspiration from the PGFbID system's ability to reduce HOSIDFs compared to the PCI-PID system and finally achieve fewer limit cycles based on experimental results, it is conceivable to apply a CR element to the PCI-PID system in order to mitigate the HOSIDFs within the system. By conducting experiments to observe whether the addition of a CR element to the PCI-PID controller results in reduced limit cycles when subjected to a step (or quasi-step) reference input, we could establish a strong link between the magnitude of HOSIDFs and the occurrence of limit cycles.

3. In reference to performance prediction of reset controllers, several suggestions are provided.

   - Developing closed-loop performance prediction methods in frequency-domain allowing less assumptions is a promising research direction. A consideration of the higher-order harmonics within the RCS resulted from the higher-order harmonics at the input of reset controller would facilitate a more precise performance prediction, especially for the frequency range where $N_{ri}(\omega) = 2$. With the aid of this refined performance prediction methodology and the optimized PGFbID systems being capable of achieving $N_{ri}(\omega) = 2$ across the entire frequency range, we could firstly establish a theoretical proof indicating that reset control has the potential to break the conventional limitations associated with LTI feedback control. This involves demonstrating that the S_∞ of the PGFbID system remains below the S of the original PID system across the entire frequency range.

   - Enhancements are needed in frequency-domain closed-loop performance prediction of RCS, aiming to eliminate the necessity of relying on the both second and third assumptions stated in Theorem 2.2 from Chapter 3. By achieving this advancement, a more precise prediction of scenarios involving multiple resets ($N_{ri}(\omega) > 2$) could be accomplished.

   - At present, performance prediction methods for reset controllers operate in the continuous-time domain. However, for improved practical applicability, it is recommended to explore

performance prediction in the discrete-time domain, aiming for greater accuracy.

4. The process of determining whether $N_{ri}(\omega) = 2$ is achieved for a certain frequency ω , relies on time-domain calculations in this study, which can be time-consuming. Consequently, the exploration of a frequency-domain approach, which allows the utilization of the machine's FRF to identify whether $N_{ri}(\omega) = 2$ is achieved, is recommended for further development.

5. The stability of PGFbI cannot currently be ensured. Therefore, the development of stability guarantee method for PGFbI structure is supposed to be proposed, and integrate this method into the current tuning algorithm of PGFbI structure to achieve a more comprehensive tuning. Additionally, incorporating stability guarantees into the tuning process of the PCI-PID structure should also be considered.

Bibliography

[1] ASM Pacific Technology Ltd., "Asm pacific technology." `https://www.asmpt.com` (accessed 16/07/2023).

[2] M. Schuettler and T. Stieglitz, "Microassembly and micropackaging of implantable systems," in *Implantable Sensor Systems for Medical Applications*, pp. 108–149, Elsevier, 2013.

[3] D. Caporale, "Overcoming inherent performance limitations in industrial motion stages with reset control: A general approach to the design and implementation of reset controllers validated on an asmpt ab383 wire bonder," Master Thesis,Technology University of Delft, 2022.

[4] K. J. Åström and R. M. Murray, *Feedback systems: an introduction for scientists and engineers*. Princeton university press, 2021.

[5] A. A. Dastjerdi, N. Saikumar, and S. H. HosseinNia, "Tuning guidelines for fractional order pid controllers: Rules of thumb," *Mechatronics*, vol. 56, pp. 26–36, 2018.

[6] R. M. Schmidt, G. Schitter, and A. Rankers, *The Design of High Performance Mechatronics: High-Tech Functionality by Multidisciplinary System Integration*. Ios Press, 2020.

[7] H. W. Bode, "Network analysis and feedback amplifier design," Van Nostrand, 1945.

[8] K. Krishnan and I. Horowitz, "Synthesis of a non-linear feedback system with significant plant-ignorance for prescribed system tolerances," *International Journal of Control*, vol. 19, no. 4, pp. 689–706, 1974.

[9] W. Foster, D. Gieseking, and W. Waymeyer, "A nonlinear filter for independent gain and phase (with applications)," 1966.

[10] D. A. Deenen, M. F. Heertjes, W. P. M. H. Heemels, and H. Nijmeijer, "Hybrid integrator design for enhanced tracking in motion control," in *2017 American Control Conference (ACC)*, pp. 2863–2868, IEEE, 2017.

[11] J. C. Clegg, "A nonlinear integrator for servomechanisms," *Transactions of the American Institute of Electrical Engineers, Part II: Applications and Industry*, vol. 77, no. 1, pp. 41–42, 1958.

[12] A. van der Maas, N. van de Wouw, and W. P. M. H. Heemels, "Filtered split-path nonlinear integrator (f-spani) for improved transient performance," in *2017 American Control Conference (ACC)*, pp. 3500–3505, IEEE, 2017.

[13] B. Sharif, A. van der Maas, N. van de Wouw, and W. P. M. H. Heemels, "Filtered split-path nonlinear integrator: A hybrid controller for transient performance improvement," *IEEE Transactions on Control Systems Technology*, vol. 30, no. 2, pp. 451–463, 2021.

[14] B. Sharif, A. van der Maas, N. van de Wouw, and W. P. M. H. Heemels, "Filtered split-path nonlinear integrator: A hybrid controller for transient performance improvement," *IEEE Transactions on Control Systems Technology*, vol. 30, no. 2, pp. 451–463, 2022.

[15] A. A. Dastjerdi, A. Astolfi, and S. H. HosseinNia, "A frequency-domain stability method for reset systems," in *2020 59th IEEE Conference on Decision and Control (CDC)*, pp. 5785–5791, IEEE, 2020.

[16] A. Baños and A. Barreiro, *Reset control systems*. Springer, 2012.

[17] N. Saikumar, K. Heinen, and S. H. HosseinNia, "Loop-shaping for reset control systems: A higher-order sinusoidal-input describing functions approach," *Control Engineering Practice*, vol. 111, p. 104808, 2021.

[18] A. A. Dastjerdi, A. Astolfi, N. Saikumar, N. Karbasizadeh, D. Valério, and S. H. HosseinNia, "Closed-loop frequency analysis of reset control systems," *IEEE Transactions on Automatic Control*, vol. 68, no. 2, pp. 1146–1153, 2023.

[19] X. Zhang, M. B. Kaczmarek, and S. H. HosseinNia, "Frequency-domain analysis for reset systems using pulse-based model," *arXiv preprint arXiv:2206.00523*, 2022. Availiable: https://arxiv.org/abs/2206.00523 (visited on 15/08/2023).

[20] N. Karbasizadeh and S. H. HosseinNia, "Continuous reset element: Transient and steady-state analysis for precision motion systems," *Control Engineering Practice*, vol. 126, p. 105232, 2022.

[21] N. Saikumar, R. K. Sinha, and S. H. HosseinNia, ""constant in gain lead in phase" element–application in precision motion control," *IEEE/ASME Transactions on Mechatronics*, vol. 24, no. 3, pp. 1176–1185, 2019.

[22] S. van den Eijnden, *Hybrid Integrator-Gain Systems: Analysis, Design, and Applications*. PhD thesis, Mechanical Engineering, Eindhoven University of Technology, June 2022.

[23] A. Banos and A. Vidal, "Design of reset control systems: the pi+ ci compensator," *Journal of Dynamic Systems, Measurement, and Control*, vol. 134, no. 5, 2012.

[24] O. Beker, *Analysis of reset control systems*. PhD thesis, University of Massachusetts Amherst, 2001.

[25] D. Paesa, J. Carrasco, O. Lucia, and C. Sagues, "On the design of reset systems with unstable base: A fixed reset-time approach," in *IECON 2011-37th Annual Conference of the IEEE Industrial Electronics Society*, pp. 646–651, IEEE, 2011.

[26] Y. Guo, Y. Wang, L. Xie, H. Li, and W. Gui, "Optimal reset law design of reset control systems with application to hdd systems," in *Proceedings of the 48th IEEE Conference on Decision and Control (CDC) held jointly with 2009 28th Chinese Control Conference*, pp. 5287–5292, IEEE, 2009.

[27] X. Zhang and S. H. HosseinNia, "Frequency-domain analysis for infinite resets systems," in *2023 IEEE International Conference on Mechatronics (ICM)*, pp. 1–6, 2023.

[28] Y. Guo, Y. Wang, and L. Xie, "Frequency-domain properties of reset systems with application in hard-disk-drive systems," *IEEE Transactions on Control Systems Technology*, vol. 17, no. 6, pp. 1446–1453, 2009.

[29] N. Saikumar, K. Heinen, and S. H. HosseinNia, "Corrigendum to "loop-shaping for reset control systems: A higher-order sinusoidal-input describing functions approach" [control engineering practice 111 (2021) 104808]," *Control Engineering Practice*, vol. 137, p. 105565, 2023.

[30] Y. Guo, L. Xie, and Y. Wang, *Analysis and design of reset control systems*. Institution of Engineering and Technology, 2015.

[31] L. Hazeleger, M. Heertjes, and H. Nijmeijer, "Second-order reset elements for stage control design," in *2016 American Control Conference (ACC)*, pp. 2643–2648, IEEE, 2016.

[32] Y. Liu and L. F. van Eijk, "Pgfbid and pci-pid tuning algorithms." `https://www.mathworks.com/matlabcentral/fileexchange/134127-pgfbid-and-pci-pid-tuning-algorithms`, Matlab Central File Exchange, Retrieved 21/08/2023.